

General Disclaimer

One or more of the Following Statements may affect this Document

- This document has been reproduced from the best copy furnished by the organizational source. It is being released in the interest of making available as much information as possible.
- This document may contain data, which exceeds the sheet parameters. It was furnished in this condition by the organizational source and is the best copy available.
- This document may contain tone-on-tone or color graphs, charts and/or pictures, which have been reproduced in black and white.
- This document is paginated as submitted by the original source.
- Portions of this document are not fully legible due to the historical nature of some of the material. However, it is the best reproduction available from the original submission.

NASA CR-143799

(NASA-CR-143799) SOLAR GAMMA RAY MONITOR
FOR OSO-H (0.3-10 MeV) Final Report (New
Hampshire Univ.) 278 p HC \$8.75 CSCL 18D

N75-23922

Unclas
G3/35 21435

SOLAR GAMMA RAY MONITOR FOR OSO-H (0.3-10 MeV)

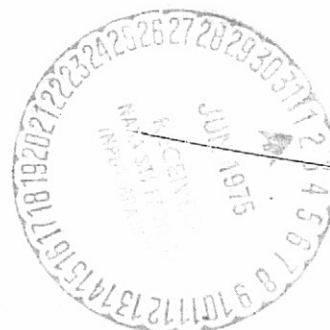
E. L. CHUPP
PRINCIPAL INVESTIGATOR

Department of Physics
University of New Hampshire
Durham, New Hampshire 03824

DECEMBER 1974

FINAL REPORT FOR CONTRACT NAS5-11054

PREPARED FOR
GODDARD SPACE FLIGHT CENTER
Greenbelt, Maryland 20771



SOLAR GAMMA RAY MONITOR FOR OSO-H (0.3-10 MeV)

E. L. CHUPP
PRINCIPAL INVESTIGATOR

Department of Physics
University of New Hampshire
Durham, New Hampshire 03824

DECEMBER 1974

FINAL REPORT FOR CONTRACT NAS5-11054

PREPARED FOR
GODDARD SPACE FLIGHT CENTER
Greenbelt, Maryland 20771

PREPARED BY:

I. U. Gleske 12/1/74
I. U. Gleske Date

D. J. Forrest 12/11/74
D. J. Forrest Date

APPROVAL:

E. L. Chupp 12/31/74
E. L. Chupp Date
Principal Investigator

CONTRIBUTIONS FROM:

R. Adams	J. Kantauskis
A. Buck	R. Kwor
E. Chupp	F. Littlefield
M. Chupp	A. Mammay
S. Croteau	D. Patel
P. Dunphy	K. Patel
P. Ferguson	C. Peabody
D. Forrest	F. Quivey
S. Foss	C. Reppin
C. Fowler	A. Sarkady
I. Gleske	L. Sherman
J. Googins	M. Simmons
P. Higbie	A. Suri
I. Horne	C. Tsai

Acknowledgment

From the very beginning of the University of New Hampshire OSO-7 project in 1965 to the present, many people have contributed to all phases of design, construction, testing, and data analysis of the experiment. It is thanks to their dedication and effort that the project was successful, and we wish to express our gratitude and appreciation to all of them.

Preface

This document is the final project report submitted in partial fulfillment of NASA Contract Nas 5-11054, whose goal was to design and fabricate a gamma ray experiment to be flown aboard the OSO-7 spacecraft. This report contains a history of the development of the experiment, a description of the gamma ray detector and its operation, and a short preliminary review of the scientific information obtained during the instrument's lifetime. A list of all reports and scientific publications (to August 1974) resulting from this project are listed at the end of this report.

Assembly of the gamma ray detector components and the design and fabrication of the electronics was subcontracted to Time-Zero Corporation of Torrance, California. The objectives of the subcontract were to design, fabricate, and test a breadboard version of the experiment for balloon flight, 1 flight unit, 1 flight backup unit, and 1 ground support equipment (GSE) which included a Varian 620/i. The breadboard was flown successfully on a balloon flight in December 1969. Data from this flight verified overall operation of the experiment and indicated modifications that were necessary and which were incorporated into the flight units.

Field support was provided where necessary for instrument calibration at Ball Brothers Research Corporation (BBRC) of Boulder, Colorado; launch activities, at Cape Kennedy (ETR) and Goddard Space Flight Center (GSFC); and programming support, at the University of New Hampshire (UNH). The OSO-7 spacecraft and its complement of instruments was successfully launched from Cape Kennedy on September 29, 1971.

The primary scientific objective of the project was to detect gamma ray lines from the sun. This goal was achieved during the solar events of August 4-7, 1972. For the first time in history, the University of New Hampshire OSO-7 observations gave direct proof that gamma rays are produced on the sun by nuclear reactions yielding neutrons, positrons, and excited carbon and oxygen nuclei.

The main features of the experiment and detector may be summarized as follows:

1. Monitor solar gamma ray flux from 0.3-9.1 MeV with a high resolution gamma ray spectrometer to search for nuclear gamma ray lines (see Section 3.3).

2. Monitor the continuum solar gamma ray spectrum over the same energy range, and simultaneously monitor the 7.5-120 keV x-ray energy range (see Section 3.3.2.5).

3. Provide for internal calibration of detector automatically or on external command (see Section 3.14).

4. Change data-handling mode on command to emphasize high resolution or a broad spectral survey (see Section 3.9).

The UNH gamma ray detector operated an average of 18 hours a day for approximately 15 months. The majority of the data was collected in the solar and antisolar direction, but data at right angles to the spacecraft-sun line was also accumulated. In all, at least two full scans of the celestial sphere were completed.

On December 25, 1972 the UNH instrument failed, apparently because of a problem in the low voltage power supply. Analysis of the data for other solar, cosmic, and atmospheric gamma rays is continuing.

Table of Contents

	<u>Page</u>
List of Figures	vi
List of Tables	viii
1. Philosophy of Instrument Design	1-1
2. History of the Instrument Development	2-1
*3. Description of the Instrument	3-1
3.1 Mechanical Description	3-1
3.1.1 Sensor	3-1
3.1.2 Electronics	3-6
3.1.3 Low Voltage Power Supply	3-9
3.1.4 High Voltage Power Supply	3-9
3.1.5 Memory and Logic Assembly	3-12
3.1.6 PHA and Front End Electronics	3-14
3.2 Mechanical Analysis and Testing	3-16
3.2.1 Vibration	3-16
3.2.2 Thermal Design	3-18
3.3 Detector Assembly	3-20
3.3.1 Selection of Detector Components	3-20
3.3.2 Signal Conditioning	3-24
3.3.2.1 Central Detector Signal	3-24
3.3.2.2 Cup Detector Signal	3-25
3.3.2.3 Slab Detector Signal	3-29
3.3.2.4 Co ⁶⁰ Detector Signal	3-30
3.3.2.5 X-ray Detector Signal	3-32

3.4	Low Voltage Power Supply	3-34
3.5	High Voltage Power Supplies	3-39
3.5.1	Shield High Voltage Supply	3-46
3.5.2	Central Detector High Voltage Supply	3-46
3.5.3	HVPS Programmer	3-56
3.6	Aspect Timing	3-59
3.7	Live Time Logic	3-67
3.8	Dead Time Measurement	3-70
3.8.1	Dead Time Logic	3-70
3.8.2	Dead Time Circuit	3-73
3.9	Command Mode Logic	3-79
3.9.1	Scan Mode	3-79
3.9.2	Quadrant Mode	3-81
3.9.3	Gain Mode	3-82
3.9.4	Calibrate Mode Logic	3-82
3.9.5	Aspect Mode	3-84
3.9.6	Charged-particle HVPS Mode	3-84
3.9.7	Central HVPS Mode	3-84
3.9.8	Central HVPS Step Mode	3-85
3.10	Main Frame Sequence	3-86
3.11	DEM Data Processor	3-90
3.12	Analog Subcom Data Sequence (ASC data)	3-97
3.13	Quadratic Pulse Height Analyzer	3-101
3.13.1	Design Considerations	3-102
3.13.2	Design Implementation	3-104
3.13.3	Results	3-108

3.14	In-flight Calibration (IFC)	3-113
3.14.1	Central Detector Radioactive Source	3-115
3.14.2	X-ray Detector Radioactive Source	3-116
3.14.3	Electronic Calibration	3-117
3.15	Ground Support Equipment (GSE)	3-121
*4.	Instrument Performance	4-1
4.1	Energy Resolution	4-1
4.2	Electronics Duty Cycle	4-3
4.3	Pulse Height Dynamic Range	4-3
4.4	Overall Stability	4-4
4.5	PHA Differential Nonlinearity	4-5
4.6	Maximum PHA Dead Time	4-10
4.7	Live Time Accuracy	4-11
4.8	Quadrant Placement	4-12
4.9	Performance Summary	4-12
5.	Gamma Ray Response Function	5-1
6.	Postlaunch Operation	6-1
6.1	Quick Look System	6-3
6.2	Failure	6-4
7.	Data Processing	7-1
7.1	Quick Look Data Processing	7-1
7.2	Final Data Processing	7-3
7.2.1	PASS1	7-5
7.2.2	CAL1	7-7
7.2.3	CAL2	7-9
7.2.4	PASS3	7-11
7.2.5	VAPREDICT Program	7-13

8.	Initial Scientific Results	8-1
8.1	Assessment of Detector Operation	8-1
8.2	Review of Solar Gamma Ray and Neutron Measurement	8-3
8.3	August 1972 Flare Measurements	8-14
8.4	Preliminary Interpretation	8-23
8.5	Justification as an Extraterrestrial Event .	8-26
8.6	Solar Flux Values	8-29
8.7	Summary of Flare Results	8-33
8.8	Continuing Program - Solar Analysis	8-35
8.9	Continuing Program - Cosmic Analysis	8-39
9.	New Technology	9-1
	References	10-1
	List of Reports and Publications	10-4
	List of Abbreviations	10-8
	Appendix	
	"An Electronically Gated Gamma and X-ray Calibration Scheme"	A-1
	"A Gamma Ray Monitor for the OSO-7 Spacecraft" . . .	A-7
	"Experimental Gamma Ray Response Function for the OSO-7 Spacecraft"	A-13

*Based on "Final Report for OSO-H Gamma Ray Monitor," prepared
by Time-Zero Corporation.

List of Figures

<u>Figure</u>	<u>Page</u>
3.1.1-1 Sensor Schematic	3-2
3.1.1-2 OSO-H Gamma Ray Monitor Detector Assembly	3-3
3.1.2-1 Typical Welded Module	3-8
3.1.3-1 Low Voltage Assembly	3-10
3.1.4-1 High Voltage Assembly	3-11
3.1.5-1 Memory and Logic Assemblies	3-13
3.1.6-1 PHA and Front End Electronics	3-15
3.5-1 Simplified Block Diagram Gamma Ray Detector	3-45
3.5.1-1 UNH Small PMT Schematic	3-47
3.5.2-1 UNH Central Detector PMT Schematic	3-48
3.5.2-2 High Voltage (HV-1) Volts	3-49
3.5.2-3 Backup High Voltage Power Supply Test	3-51
3.6-1 Simplified Block Diagram of Aspect Timing	3-60
3.6-2 Aspect Timing (Normal Quadrant Mode)	3-66
3.7-1 Block Diagram and Timing Sequence of Live Time Logic	3-68
3.8.1-1 Block Diagram Dead Time Logic	3-72
3.8.2-1 Functional Block Diagram of Dead Time Analog Circuit	3-75
3.10-1 Block Diagram Main Frame Data Control	3-88
3.11-1 DSM Data Sequence	3-91

3.11-2	Main Frame SYNC Timing Generator	3-92
3.11-3	Data Processor Block Diagram	3-94
3.13.2-1	Block Diagram of ADC Portion of the Quadratic PHA	3-105
3.13.3-1	Plot of DNL of Quadratic PHA	3-109
3.13.3-2	Analysis of Co ⁶⁰ by the Quadratic PHA	3-112
4.1-1	Resolution Ratio versus Detector Resolution	4-2
4.5-1	Differential Nonlinearity Analysis Printout	4-6
4.5-2	Differential Nonlinearity Analysis Plot	4-7
4.5-3	PHA DNL Test	4-8
4.9-1	Instrument Specifications	4-13
4.9-2	UNH OSO-7 Detector Parameters	4-14
6.2-1	Plot Readout Values versus -12 Volts	6-5
8.1-1	Solar Neutron Measurement	8-8
8.3-1	Time-Integrated Spectrum	8-16
8.3-2	August 4, 1972	8-18
8.3-3	X-ray Plot August 4, 1972	8-20
8.3-4	August 7, 1972	8-21
8.5-1	Housekeeping Data	8-27
8.9-1	Comparison of Energy Loss Spectra	8-44

List of Tables

<u>Table</u>		<u>Page</u>
I	Test History of Flight Unit 1	2-4
II	Test History of Flight Unit 2	2-8
III	Known Differences between Flight Unit 1 and Flight Unit 2	2-10
IV	Comparison of the Performance of Flight Unit 1 and Flight Unit 2.	2-11
V	PHA Channel Assignments	3-87
VI	Adaptive Prescaler	3-95
VII	Analog Housekeeping Sequence	3-98
VIII	Quadratic PHA Specifications	3-111
IX	Electronic Pulse Calibration Format	3-118
X	Summary of Recent Solar Neutron and Gamma Ray Observations to August 1972.	8-5
XI	Solar Gamma Ray Flux at 1 AU.	8-31
XII	Categories of Events	8-40

1. Philosophy of Instrument Design

The main objective of the instrument was to monitor the sun for the emission of certain gamma ray lines that were expected to be associated with large solar flares. Because of the low intensity and line nature of these radiations, the instrument was designed to have as high a sensitivity and energy resolution as possible. At the time this instrument was designed, these requirements were best met by an inorganic scintillator-photomultiplier detector. This combination also had the advantage of a high dynamic range in both energy interval and intensity. The first choice for a scintillator was NaI(Tl) because of its energy resolution. However, since it was not known if the mechanical properties of NaI(Tl) were sufficient for space application, a parallel design effort was carried out using the more rugged CsI(Na) scintillator. Fortunately, a packaging technique was found so that NaI(Tl) could be used. Similarly some effort was made to find a stable, high resolution, rugged 3-inch diameter photomultiplier.

The final central gamma ray detector, as described in this report, exceeded the performance of most similar laboratory detectors and operated satisfactorily over the full life of the experiment. The only problem encountered was the

detector's high sensitivity to overload conditions caused by the spacecraft's passage through the trapped radiation regions. This problem is discussed in more detail later (see Section 4).

Originally the detector was enclosed in a plastic shield in order to reject charged particles. However, during the initial satellite development the experiment's weight allotment was increased thereby allowing the shield to be updated to a more massive CsI(Na) scintillator. The new shield not only rejected charged particles but also inhibited local gamma ray production from the spacecraft material and enhanced the gamma ray line sensitivity by suppressing the Compton continuum.

An x-ray detector was also added at this time to allow us to select time intervals when the solar x-ray flux was higher and gamma ray emissions more probable.

Several unique instrumental improvements were incorporated into the experiment. One of these improvements was the direct measurement of the central detector live time, and although the analog techniques used in our case may not have been ideal, data analysis results strongly justified the need for this information. Another improvement was the use of the gated Co^{60} energy calibration unit (see Section 3.14), which allowed us to determine the energy calibration very accurately twice each

orbit. Because of the unexpected gain variations experienced by our central detector, data analysis would have been difficult or perhaps impossible a good fraction of the time without these energy calibrations. The final noteworthy improvement was the use of the quadratic pulse height analyzer (PHA) (see Section 3.13). The quadratic PHA utilized the entire resolution of our detector over the full energy range (0.3-9 MeV) with one-third the number of channels that would be required with a normal linear PHA. Hence our time resolution was a factor of 3 better.

To help determine the source of any observed increase in the detector counting rate, data was accumulated simultaneously in two directions. One was the solar direction (pointing toward the sun) and the second was the background direction (pointing away from the sun). These two directions were heavily shielded from each other by the mass of the spacecraft; and hence any increase in the gamma ray flux from the solar direction could be determined by comparison of the two data blocks.

2. History of the Instrument Development

The instrument was conceived and the detector designed at UNH in 1967. The mechanical and electrical design and the fabrication were done by Time-Zero Corporation (formerly Marshall Laboratories).

Major detector components were purchased and tested by UNH and then placed in bonded storage at Time-Zero. UNH personnel traveled to T-Z to support the work there and to help interface the detector and electronics.

A balloon-borne flight of the instrument, in the form of the breadboard electronics and a prototype detector, was performed in December 1969 in order to test the instrument and to gather actual counting rate information at altitude.

The engineering model, with plastic shield, was used in the early vibration tests (see Section 3.2.1) to verify overall mechanical design. The detector was changed between the breadboard engineering model and the prototype to include the CsI shield. The prototype instrument was flown with the breadboard detector in the balloon experiment, and the electronics were slightly changed for the flight unit.

Integration of the instrument into the BBRC spacecraft was accomplished with no major problems. Several malfunctions were discovered and repaired in the process of integration but were not caused by integration.

There was a possibility that other calibration sources on the spacecraft would interfere with our instrument. A test was conducted to look for such interference; compatibility tests showed no interference with or from other instruments. However, a temporary gain loss and a problem with the high energy channels was encountered. The high energy problem was corrected, but the gain loss could not be explained. It happened once again during thermal-vac testing (see Section 3.2.2) but could not be repeated thereafter.

The test history of flight units 1 and 2 is summarized in Tables I and II.

The known differences between units 1 and 2 are summarized in Table III; Table IV is a comparison of the two units.

Final tests on the instrument were carried out at Time-Zero by both UNH and T-Z personnel. Several procedures had to be developed for testing and adjusting the detector signals, since up to this stage the emphasis at T-Z had been on processing the signals and actually fabricating the instrument.

UNH testing of the detector components was conducted with lab instrumentation. During final testing some malfunctions occurred but were all explained and corrected. The history of final tests on prototype and flight units is summarized in Section 3.2.

The OSO-7 satellite was launched on September 29, 1971 from Cape Kennedy. The instrument operated successfully until December 25, 1972.

ORIGINAL PAGE IS
POOR QUALITY

Table I
Test History of Flight Unit 1

DATES	TEST	MALFUNCTION	CORRECTIVE ACTION	MALFUNCTION REPORT NO.
<u>1971</u>				
1/27	Rm temperature Functional	None	None	---
1/29	-10°C Functional	Logic failure: unit does not change from background to sun	Replaced Z2022 and Z2036 Z2056 logic board No. 2 804437-101	C00908
			Repaired abraded wire con- tacting terminal on logic board	C00908
2/1	Rm temperature Check	None	None	---
2/2	-10°C Functional	Logic failure: all functions related to quad signal quit when CPHV on	Repaired abraded wire Reconformal coated logic board	----- C00909
2/4	Rm temperature Check	None	None	---
2/5	-10°C Functional	Logic failure: same failure as noted 2/2/71 Integrated circuit temperature sensitive	Replaced Z5003 logic board No. 5 804443-101	C00912
2/7 to 2/8	Special Rm Temperature test to Check Dead Time	Excessive error in dead time measurement during high count rate	Cut ribbon Z35-17 to eliminate extra MC INH line	--- 2-4

DATES	TEST	MALFUNCTION	CORRECTIVE ACTION	MALFUNCTION REPORT NO.
<u>1971</u>				
3/6 to 4/1	Repair above malfunctions	---	---	---
4/1 to 4/2	Rm temperature Functional	None	None	---
4/3	Vibration X-X Random	None	None	---
4/4 to 4/6	-10°C Thermal vacuum	Main channel gain decreased to zero	Replaced failed resistor	C00918
			Module input opened and bypassed with external resistor	C00917
4/7	-10°C Thermal vacuum	None	None	---
4/8	+35°C Thermal vacuum	None	---	---
4/12	Interface at BBRC	Erractic data, experiment current fluctuations	Repaired cold solder joint on terminal	---
		Thermal paint cracking	Remove thermal paint	
		Ground noise out of spec.	Waiver	
		Experiment weight out of spec.	Waiver	

DATES	TEST	MALFUNCTION	CORRECTIVE ACTION	MALFUNCTION REPORT NO.
<u>1971</u>				
2/9	Rm temperature Check	None	None	---
2/9	-10°C Functional	IFC malfunction in the x-ray channel	Reconnected module shield to ground (Z59 W7367-1)	C00911
2/14	Rm temperature Check	None	None	---
2/15 to 2/16	-10°C Functional	None	None	---
2/16 to 2/18	+35°C Functional	None	None	---
2/18 to 2/19	Vibration	None detected during vibration	None	---
2/21 to 3/5	Thermal vacuum	Central detector confirmed degraded by vibration test	Central detector assembly replaced	C00915
		Central HVPS monitor circuit (diode failed)	Replaced failed diode	---
		Central HVPS divider network failed	Replaced resistor pack 804341-101	C00916
		LVPS turnon problem at -10°C	Redesigned converter drive circuit	C00914

DATES	TEST	MALFUNCTION	CORRECTIVE ACTION	MALFUNCTION REPORT No.
<u>1971</u>				
4/14 to 4/19	Repair above malfunction			
4/20	Integration	Main channel locked out during IFC	Make connector assembly to load cup signal during flight at test connector	---
5/21	Compatibility Test	Gain loss in main channel for several hours	None; condition could not be repeated	
		High channels not recording data	Take high energy signal from dynode 9 instead of dynode 10, to reduce crosstalk from H. E. circuits to cup	---
		No interference		
8/9	Thermal vacuum -10°C	Gain dropped in main channel; comprehensive test	Pending; proceed to end of test; instrument returned to normal after several hours	
8/14 to 8/16	Bench test (special)	None	(This was a monitoring test, to try to catch the low gain malfunction)	

Table II

Test History of Flight Unit 2

DATES	TEST	MALFUNCTION	CORRECTIVE ACTION	MALFUNCTION REPORT NO.
<u>1971</u>				
7/17	Corona test	Arc from HV terminal to feedback amplifier	Replace FU 2 power supply (s/n 3) with prototype power supply (s/n 1)	---
8/4	Thermal vacuum	HVPS corona; main channel	Additional potting on HVPS	C00920
		Increased gain in main channel (open attenuator resistor)	Replace surge limiter module Z1; replace R1, C1	C00920
		HV short in one cup PMT	Reposition cable in PMT; repair potting	C00997
		Damaged cup input amplifier	Replace input amp. module W7367-1	C00992
8/4 to 8/9	Repair above malfunctions			
8/10	Thermal vacuum -10°C	Main channel gain erratic	None; appears to be input resistors again; proceed at +35°C	
8/20	Thermal vacuum +35°C	instrument input current increased, HV off 145-165 watts; HV off	None; proceed to end of test	

ORIGINAL PAGE IS
OF POOR QUALITY

DATES	TEST	MALFUNCTION	CORRECTIVE ACTION	MALFUNCTION REPORT NO.
<u>1971</u> 8/22 8/23	Finish TV Repair above Start tempera- ture cycle	None	Replace main channel input resistors with Corning glass brand Monitor to determine cause of power increase of 8/20	

Table III

Known Differences between Flight Unit 1 and Flight Unit 2

ITEM	FLIGHT UNIT 1	FLIGHT UNIT 2
High voltage power supply	New Unit	Reworked Prototype
- HV Range, MC (HV 1)	880-1220 volts	950-1619 volt
- HV Q-point (gain 1)	Step 0	Step 14
- Shield HV	1359 volts	1374 volt
- X-Ray HV	1114 volts	1174 volt
Experiment current draw		
16 volts	215 mA	230 mA
19 volts	179 mA	197 mA
22 volts	155 mA	170 mA
Surge current		
22 volts	150 mA	170 mA
Power line noise	30 mV	12 mV
Power ground noise	68 mV	20 mV
Chassis ground noise	64 mV	20 mV
Weight	74.0 lbs	73.8 lbs
Power	125-135 mA at 197 volt	140-150 mA HV both off
	185	200 HV both on

Table IV

Comparison of the Performance of Flight Unit 1 and Flight Unit 2

PARAMETER			FLIGHT UNIT 1	FLIGHT UNIT 2
<u>Main Channel</u>	Energy Resolution	FWHM Cs ¹³⁷	7.5-8%	8.5-9%
		P/V Co ⁶⁰	9	6
	Energy Range, approx.,	at Q-point	0.3-10 MeV	0.3-10 MeV
	Compton Rejection at 400 keV, High Energy Channels (Q-point)	Cs ¹³⁷	2.6	1.6
		1	---	---
		2	23-46 MeV	7.2-14.4 MeV
		3	46-92 MeV	14.4-28.8 MeV
	Energy linearity, (deviation from straight line 0-0.662 MeV)	at 0.662 MeV	+1.0%	
		at 1.33 MeV	0 (reference)	
		at 2.62 MeV	-1.5%	
		at 6.1 MeV	+0.6%	
	Co ⁶⁰ calibration source,	peak ch. counts	3(10 ²)	3(10 ²)
		Rate from Co ⁶⁰ PMT	1.2 kc	1.4 kc
		Leakage	≈5%	≈5%
<u>Shield</u>	Energy threshold	in Cup	80-100 keV	120-160 keV
		in Slab	30-60 keV	60-100 keV
<u>X-ray</u>	Calibration source leakage		≈0	≈0

3. Description of the Instrument

3.1 Mechanical Description

The OSO-7 gamma ray detector's mechanical design and packaging requirements were governed by the University of New Hampshire. This instrument consists basically of the sensor and its electronics mounted within the wheel compartment of the OSO-7 spacecraft. The mechanical aspects of the instrument design, fabrication, and analysis are discussed in the following paragraphs.

3.1.1 Sensor

This experiment detector assembly is depicted in Figure 3.1.1-1 with a complete unit assembly pictorially illustrated by Figure 3.1.1-2.

The detector assembly consists of CsI(Na) crystals for the shield and front slab, NaI(Tl) crystal for the central detector, Am^{241} and Co^{60} calibration sources, and eight photomultiplier tubes (PMT's). This detector weighs approximately 55 lbs when assembled.

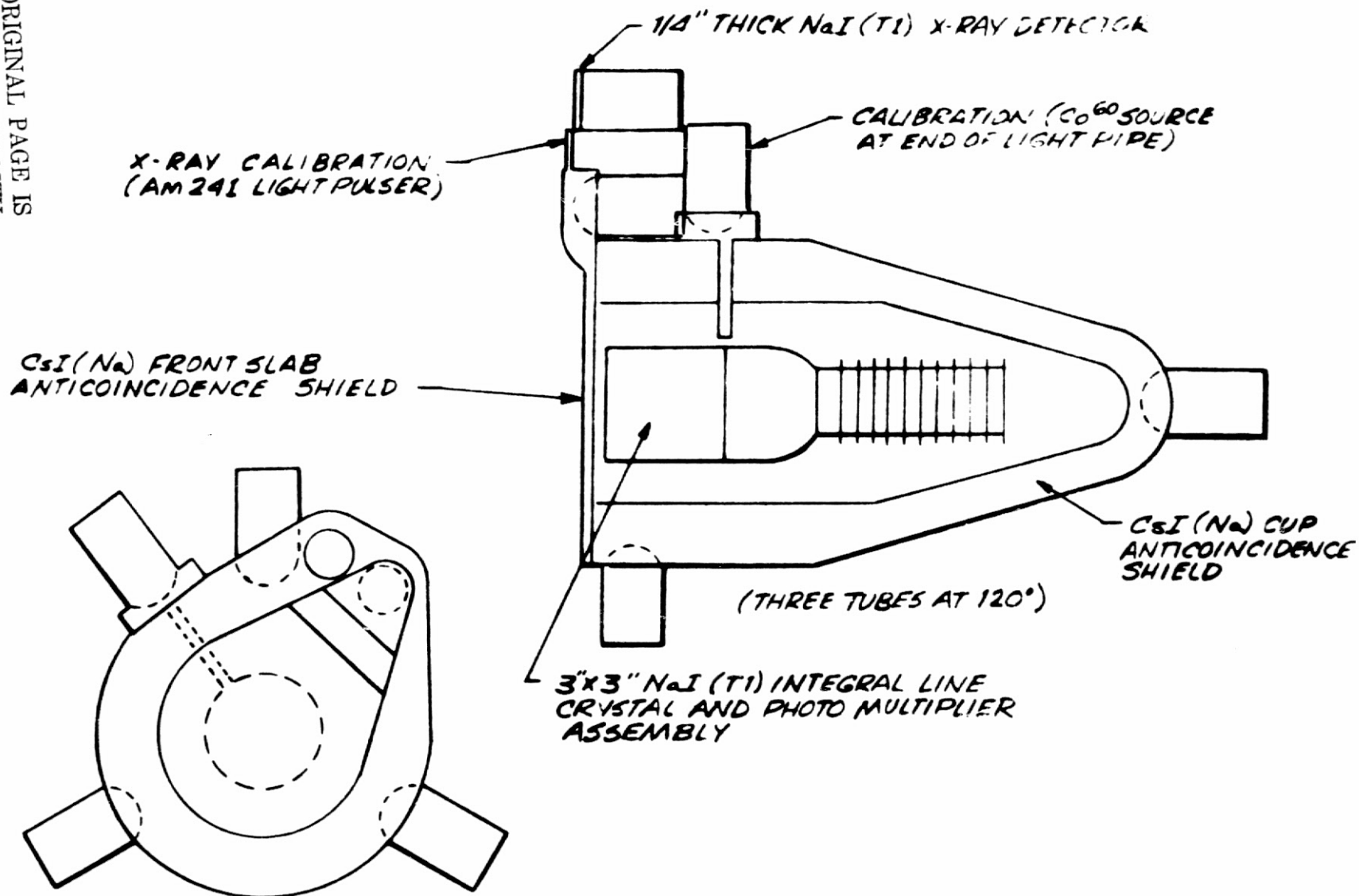
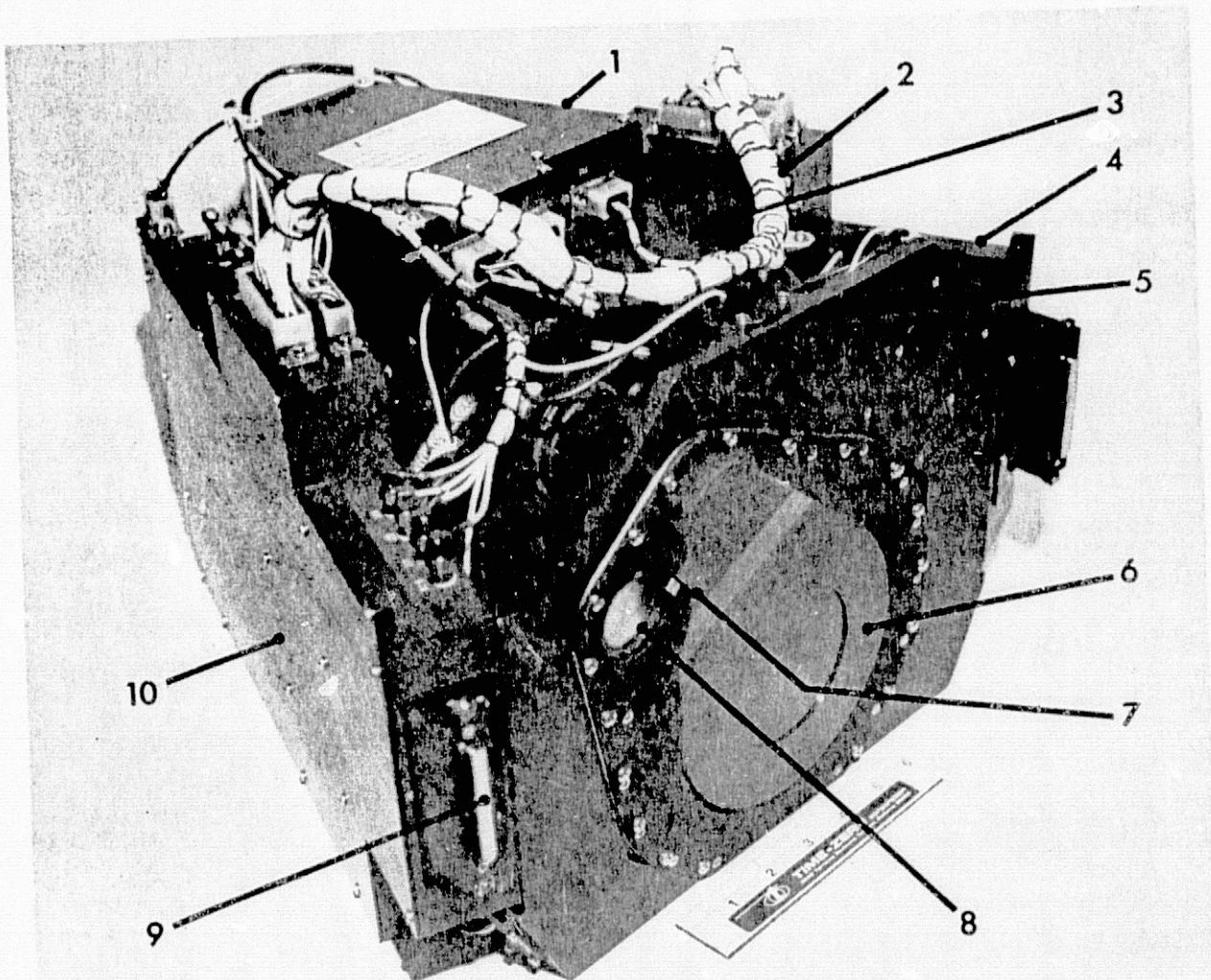


Figure 3.1.1-1 Sensor Schematic



2029

- 1 LOW VOLTAGE POWER SUPPLY
- 2 HARNESS
- 3 HIGH VOLTAGE POWER SUPPLY
- 4 BLIVET #1 MEMORY LOGIC
- 5 P.M. TUBE (6 required)
- 6 CsI (Na) FRONT SLAB & COVER
- 7 AM 241 CALIBRATION SOURCE
- 8 X-RAY TUBE NO.1 (T1)
- 9 TEST CONNECTOR 2 PLACES
- 10 BLIVET #2 FRONT END ELECTRONICS & PHA

ORIGINAL PAGE IS
OF POOR QUALITY

Figure 3.1.1-2 OSO-H Gamma Ray Detector Assembly

The crystals and photomultiplier tube assemblies were packaged within an aluminum housing. The housing was rough machined in small sections, brazed together to eliminate light leaks, and welded to ensure structural strength. The assembly was then fine machined to specification. Using this technique it was economical to fabricate and, furthermore, structurally very sound.

The central detector assembly utilizes a 3-inch photomultiplier (RCA-C31009) that has a 3- by 3-inch cylindrical NaI(Tl) crystal coupled to the photomultiplier tube face and is hermetically sealed. The electronic components that connect the anode, dynodes, and cathode together are coated with RTV-11 to provide structural support and corona protection. A stainless steel housing is fitted over the neck of the tube containing the dynode structure. The remaining volume between the stainless steel housing and the RTV-11 coating is filled with a polyurethane high density foam to insure structural integrity of the assembly. Mounted on the end, opposite the crystal, is a 3-inch hemispherical-shaped lexan plastic assembly that is used to position the central detector assembly into the large cesium iodide shield (cup).

Prior to installation of the cesium iodide shield into the housing, it is wrapped with aluminum foil to prevent light leakage and

to improve light collection at the photomultipliers. The detector housing is lined with several strips of 1-inch silicon tape to allow the cesium shield to be properly loaded.

After the cesium iodide shield is installed into the housing and centered using an O-ring, the central detector is placed in the center of the shield and foamed using a high density polyurethane. The cesium iodide shield and central detector are then properly loaded into the housing using a stainless steel plate and wave spring. The 1-inch photomultiplier tubes that view the shield are installed using RTV-615 as an optical coupler and held in place by a metal cap and wave spring assembly that loads a tube to ~ 12 lbs.

The cesium iodide front slab assembly is mounted over the area of the central detector that is not covered by the cesium iodide cup. The front slab crystal is wrapped with aluminum foil for light tightness and both sides of the crystal have a 1-inch strip of silicon tape attached to buffer the crystal against the aluminum housing.

For attachment to the spacecraft wheel compartment, the instrument provides fourteen 10-32 inserts in the mounting surface. The same structural members are used for mounting the electronic assemblies to the detector assembly.

3.1.2 Electronics

The electronics associated with the gamma ray experiment consist of five electronic assemblies. These assemblies are the high voltage power supply, low voltage power supply, memory-associated electronics and logic assembly, pulse height analyzer, and electronics associated with the sensors.

The experiment electronic circuits are quite complex and consist of approximately 265 discrete component modules (average of five transistors, etc., per module) and an additional 450 integrated circuits. The electronic circuits were packaged so that the instrument would meet the expected environmental requirements of the spacecraft while maintaining the requirements of ease of fabrication, test, and maintenance. The weight of these electronic assemblies and their housing is approximately 19 lbs.

The techniques used in the packaging were welded modules, welded wire matrix, printed circuit boards, and micropoint welding. Welded modules and interconnect matrices were selected for use where the capability of making modification with relative ease was desired thereby allowing for circuit design improvements while still maintaining a highly reliable unit. This technique also results in high density packaging with a minimum of weight. Printed circuit techniques were

utilized in the power supplies and memory electronics where it was desirable to keep impedance paths to a minimum. The micropoint welding technique was utilized to interconnect the integrated circuit logic boards. The electronic circuits were packaged to minimize noise and interconnect requirements.

A typical welded module was designed like Figure 3.1.2-1. When a module required shielding by engineering it was conformally coated, foamed using a closed cell polyurethane, covered using copper foil tape connected to a module pin for grounding to signal ground, and then the copper foil was conformally coated. Welded modules are installed into a welded matrix and interconnected using weld ribbon. The electronic assembly has a ground plane incorporated into the welded matrix to minimize noise in the low power analog sensor circuits.

Circuit components that require selection during test are located on the interconnect board side of the matrix and installed on terminals. During final electrical testing the assemblies are spot bonded, conformally coated, and encapsulated using closed cell polyurethane foam to ensure meeting the expected environmental conditions. The electronic housings were machined aluminum and black anodized. The electronic housings are mounted to the sensor housing by using through-bolt hardware.

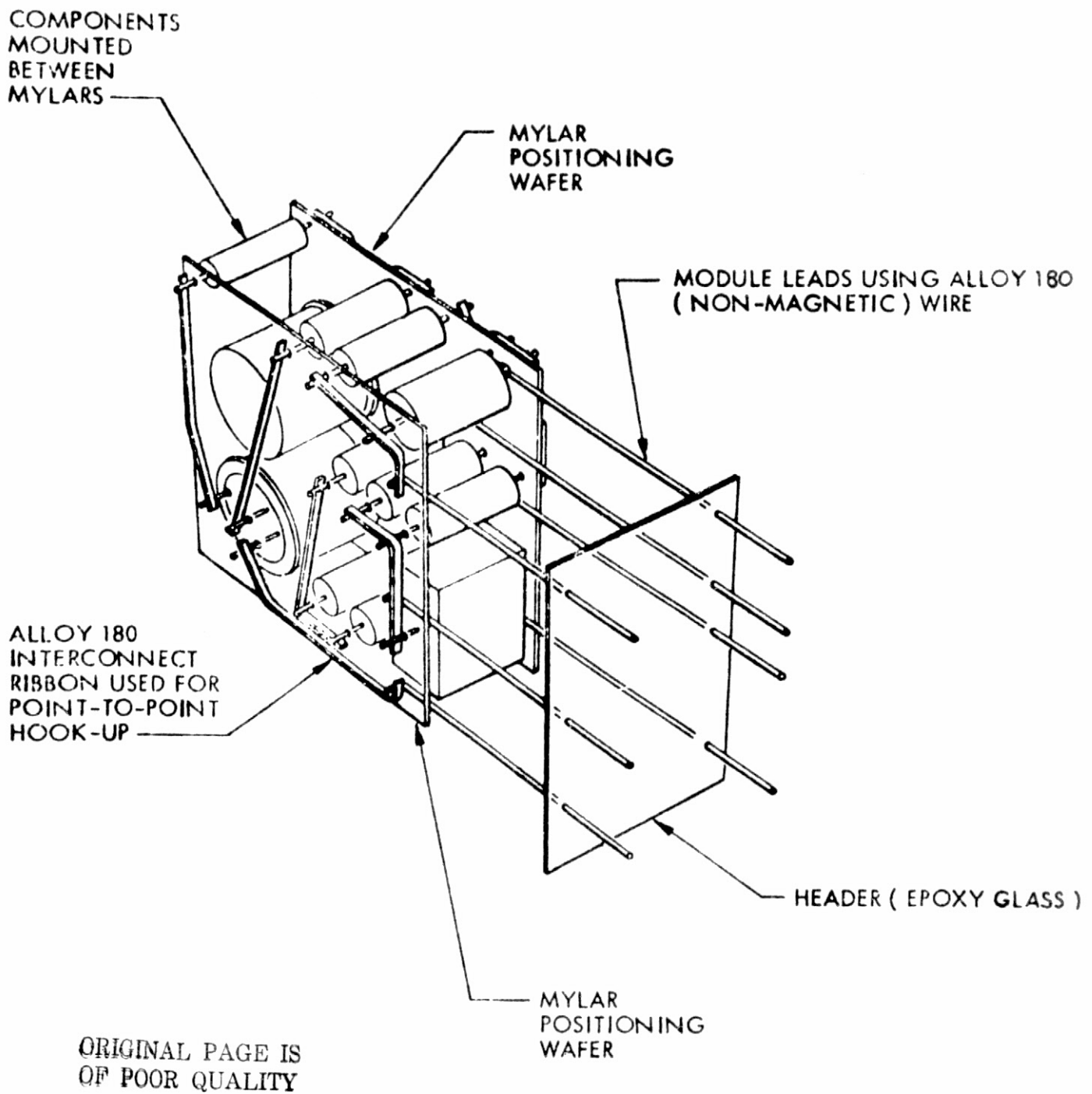


Figure 3.1.2-1 Typical Welded Module

3.1.3 Low Voltage Power Supply

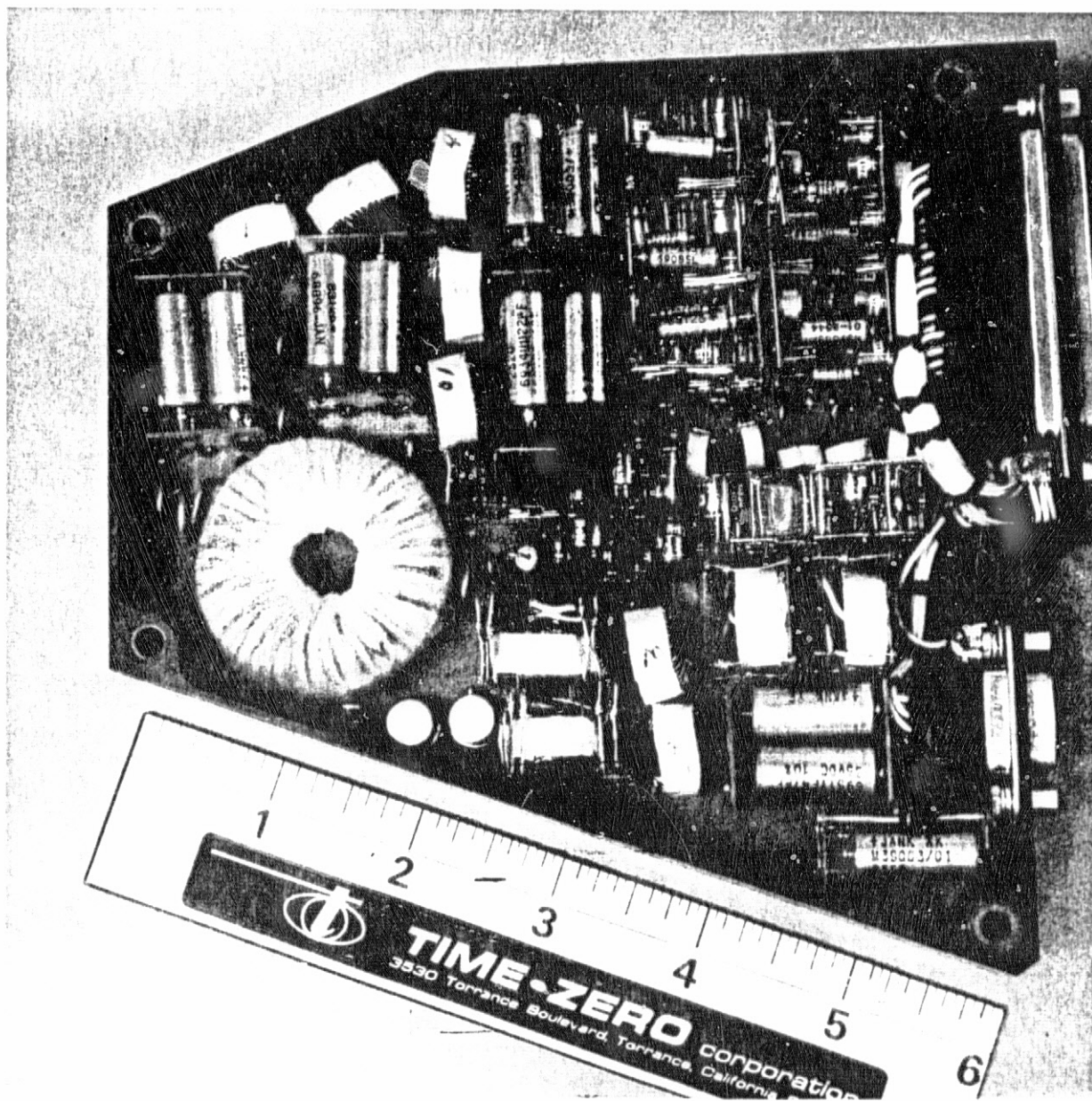
The low voltage power supply shown in Figure 3.1.3-1 is packaged as a point-to-point welded interconnect of welded modules. The assembly is conformally coated and encapsulated using closed cell polyurethane foam.

3.1.4 High Voltage Power Supply

The high voltage power supply assembly illustrated by Figure 3.1.4-1 uses welded modules interconnected by printed circuit board and soft interconnect wiring.

The high voltage supply actually consists of two separate power supplies: One supply is fixed at ~ 1100 volts and the other is programmable from approximately 1000-1300 volts.

The techniques used in the high voltage assembly included rounding off all solder joints to reduce high potential gradients which cause corona, encapsulating modules with Stycast-1090SI, and encapsulating the interconnect side of the printed circuit boards with Solithane-113.

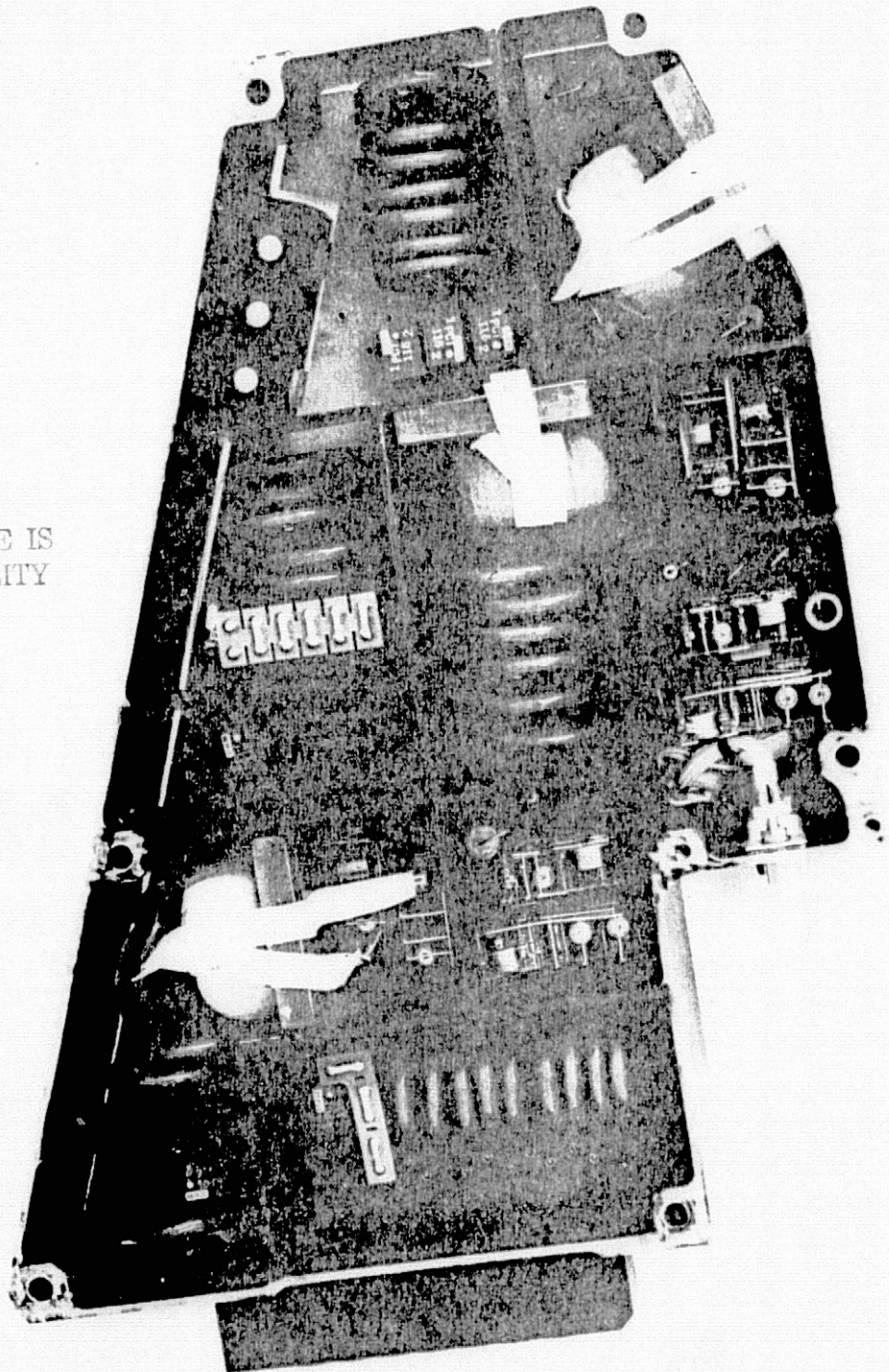


1878-71

Figure 3.1.3-1 Low Voltage Assembly

ORIGINAL PAGE IS
OF POOR QUALITY

ORIGINAL PAGE IS
OF POOR QUALITY



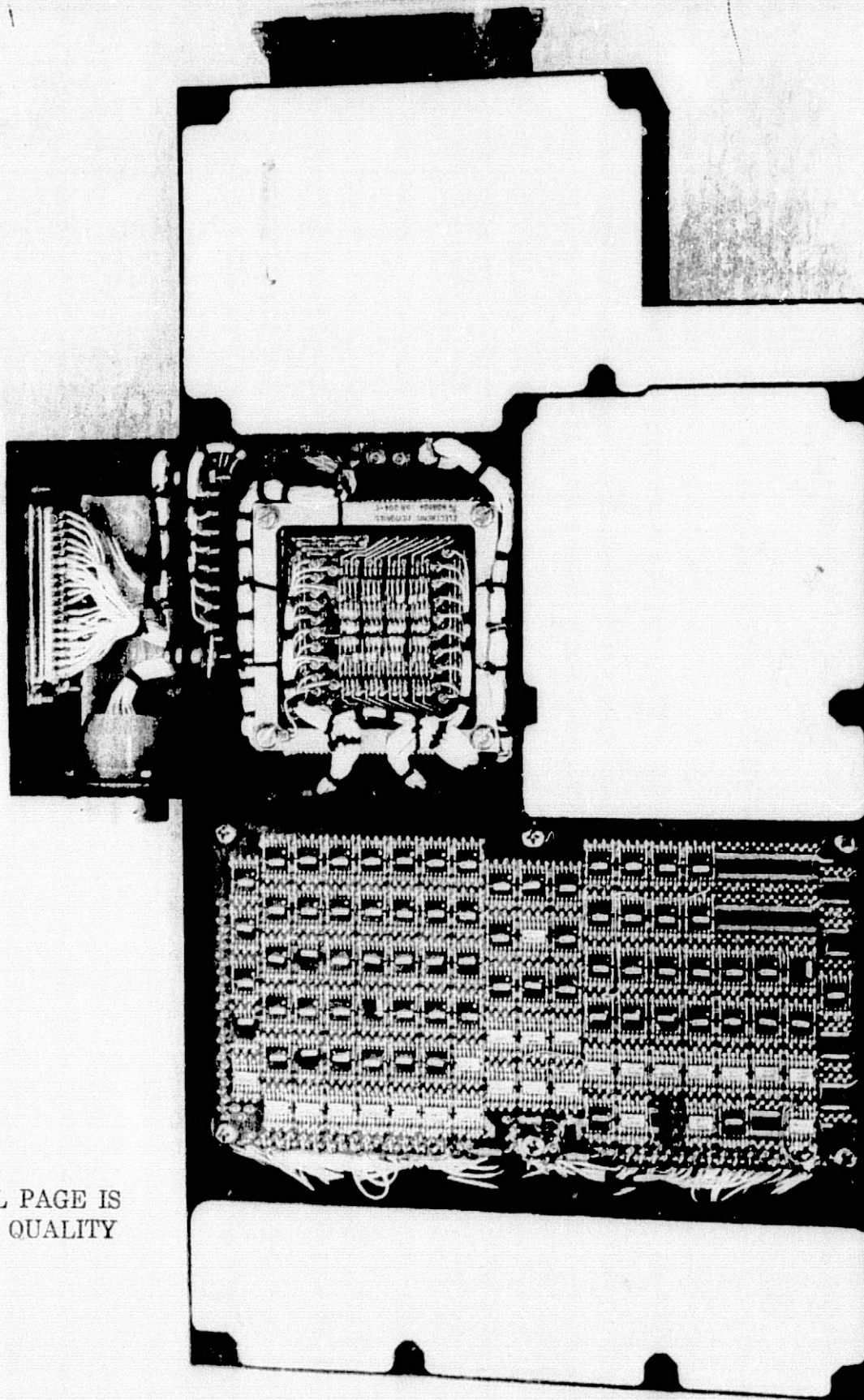
1875-71

Figure 3.1.4-1 High Voltage Assembly

3.1.5 Memory and Logic Assembly

The memory and logic assembly is pictorially shown in Figure 3.1.5-1. The memory core stack was purchased from Electronic Memories Incorporated. The overall dimensions of the core stack are 3.25- by 3.25- by 1.0-inch high. The core stack utilizes cannon Micro-D connectors for system interconnect. The memory drive and sense electronics are all welded modules installed on printed circuit boards.

The logic assembly, comprised of approximately 400 IC's, utilizes micropoint welding technique of packaging. This packaging method uses insulated wire that is cold electrode welded to goldplated stainless steel pins. The integrated circuits are installed on the opposite side of the board and parallel gap welded to the through-goldplated stainless steel pins. The individual logic boards are interconnected by means of soft wire from board to board.

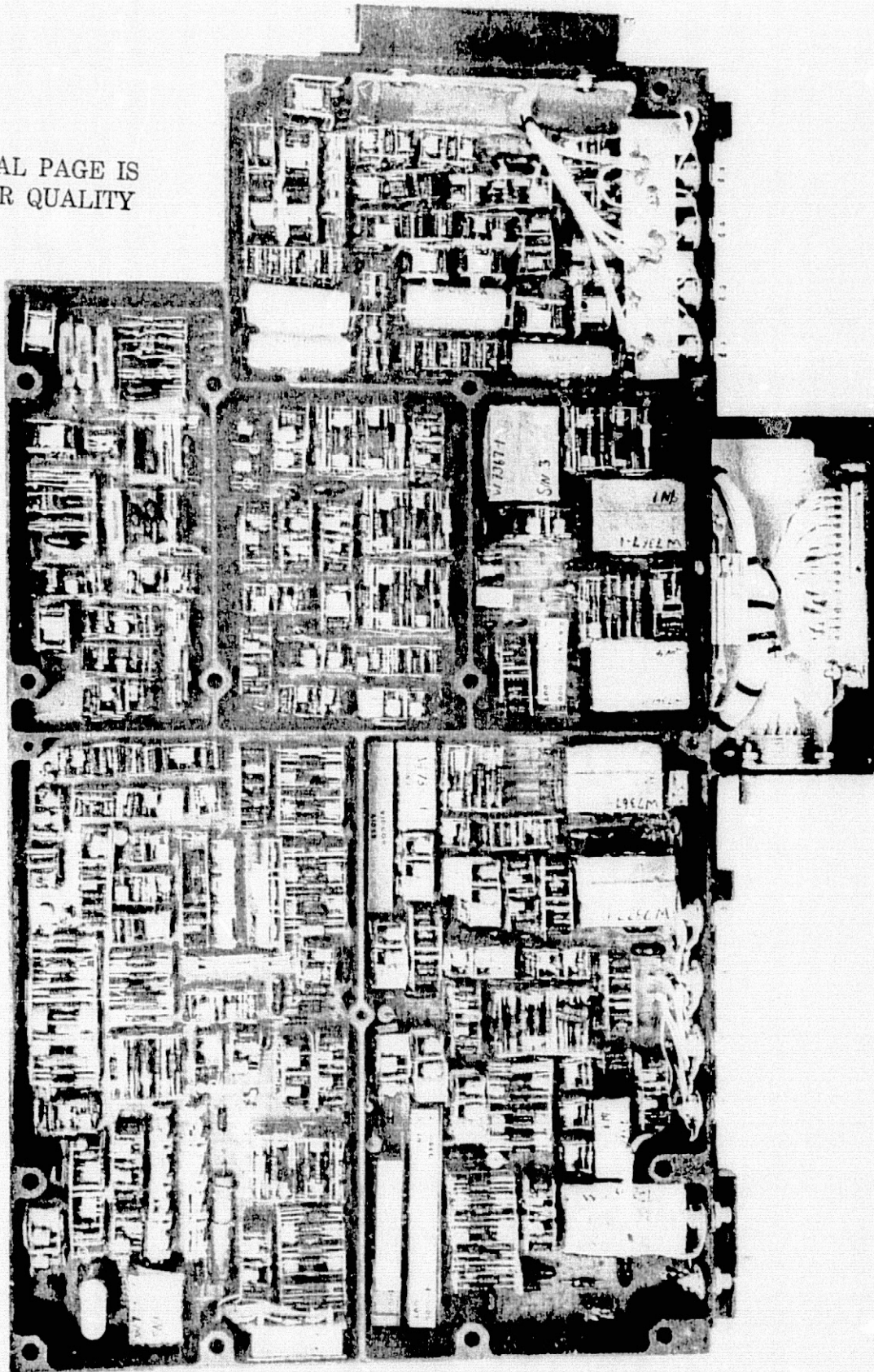


ORIGINAL PAGE IS
POOR QUALITY

3.1.6 PHA and Front End Electronics

The pulse height analyzer (PHA) and front end electronics assembly is pictorially shown in Figure 3.1.6-1. The packaging technique is welded modules interconnected by means of a welded matrix. Sensitive circuits are shielded using copper foil tape, and a ground plane is built into the matrix to allow grounding at any point to reduce system noise to a minimum.

ORIGINAL PAGE IS
OF POOR QUALITY



3.2 Mechanical Analysis and Testing

3.2.1 Vibration

The environmental requirements of the experiment were established and qualification testing was performed that verified that the experiment was capable of meeting these requirements.

During the design of the unit preliminary vibration tests were conducted using the prototype detector and dummy electronic housings to duplicate the actual weight. These tests were conducted to ensure that the three major potential problem areas of mechanical design would surpass the environmental requirements. The investigated problem areas were loss of optical coupling, cracked crystals, and photomultiplier tube (PMT) degradation. Inspection after these preliminary tests indicated no degradation.

However, during the flight unit tests (protoflight qualification tests) the following problems were observed when the detector was disassembled (see Section 3.3.1): The central detector NaI(Tl) crystal was fractured in several places and appeared to be separated from the tube face; several shield tubes had separated at the optical coupling; the Co⁶⁰ plastic light pipe was cracked. It was determined that the above-mentioned

problems were caused by an epoxy washer used to electrically isolate the central detector from the wave spring which was connected to chassis ground. The washer had worn through, reducing the preload on the central detector assembly sufficiently to cause movement which resulted in the damage mentioned. The problem was corrected by adding two stainless steel washers, one on each side of the epoxy washer, to prevent wear-through.

The central detector preload requirements were reverified and the detector reassembled. The system was retested to verify that the modifications were satisfactory. The modification was incorporated into subsequent units.

3.2.2 Thermal Design

Thermal design required that the front slab crystal housing and x-ray detector be protected thermally since these parts were directly exposed to the sun through the spacecraft rim panel. To protect the front slab assembly, a thermal paint, supplied by BBRC, was applied to the housing. The x-ray assembly was protected by an assembly made from 0.002-inch thick aluminized teflon, which acted as a second surface mirror.

Subsequent to protoflight qualification testing, it was noted the thermal control paint was cracking, which was resolved by adding an aluminum plate over the cutout in the rim panel attached to standoffs allowing the compartment to decompress. The thermal paint was removed from the housing leaving the black anodize finish.

The gamma ray monitor has the following physical properties:

Magnetic dipole moment (gauss - cm ³):	X axis	+30
	Y axis	+10
	Z axis	+50
Magnetic field adjacent(gauss):	3 inches above instru-	
	ment (+Z)	0.018
	2 inches from either	
	side	0.005
Magnetic field (milligauss):	0.5	
Moments of inertia:	X axis	4.44 inch-lb sec ²
	Y axis	4.86 inch-lb sec ²
	Z axis	5.02 inch-lb sec ²
Weight:	74.0 lbs	

3.3 Detector Assembly

The detector assembly consists of three major detector elements and two minor ones. The major elements are the central detector, the slab detector, and the cup detector. The latter two form the anticoincidence shield around the central detector and are used to identify charged-particle events among all events recorded by the central (or main) detector as well as acting as an active collimator. The minor elements are the x-ray and Co^{60} detectors, which are used to provide calibration data from an internal Co^{60} source and to aid in ground-based correlation of data.

3.3.1 Selection of Detector Components

As mentioned in Section 2, our aim was to build a rugged, high resolution detector. Additional considerations were weight, size, and gain stability. For the shield we needed a high signal-to-noise ratio in the photomultipliers in order to obtain good Compton rejection.

The central detector photomultipliers tested were the EMR-544 and the RCA-C31012. Shield photomultipliers were RCA-2067, later changed to the C70132B type. The x-ray detector PMT was an RCA-4461.

ORIGINAL PAGE IS
OF POOR QUALITY

From early in the project the EMR-544's were considered only as a backup unit because of the better resolution, stability, and mechanical properties of the RCA-C31012. However, we did encounter some manufacturing delays with the RCA PMT, which were corrected by changing the tube material specification from copper-beryllium to Kovar.

The shield photomultipliers were preselected by RCA for ruggedness, high output, and low noise (dc tests). Visual check of the PMT's was conducted at UNH, and tubes with weld or dimension defects were rejected. All PMT's were aged for a minimum of 100 hours at 5- μ A average anode current, using neon lamps as light sources. Pulse output was measured before and after aging using a scintillator crystal and radioactive source in a standard test fixture. Tubes were sorted according to gain and noise with the best lot going to the flight unit.

Various tests were conducted on the central detector PMT's to measure resolution, long term stability, operation at high light levels, and change in gain with counting rate (see Section 3.2).

The operation at high light levels was intended to simulate passage through the South American anomaly (high charged-particle fluxes) and indicated that the power supply would

limit current in the PMT and that the gain would drop sharply. This was our protection against overloads. Apparently we did not simulate the actual operating conditions accurately because we experienced severe long term gain changes in orbit (described in Section 4).

Our experience with the RCA PMT was good, and the C31012 was used in both the flight and backup units. Both units were operated for extended periods in the setup and calibration of the instrument and behaved as expected. We did, however, experience some nonlinearity due to high currents, which was corrected by the use of a nonlinear divider chain and a reduced high voltage.

During the setup period no permanent gain changes were noticed in either flight or backup unit.

Our prediction for maximum aging assumed aging to be a function of average anode current and was based on initial tests of PMT's as well as the behavior of our central detector photomultipliers during the setting up of the flight and backup units. We allowed for a 50% loss of output due to aging, and the HV supply output could be increased above the nominal operating voltage to effect a factor of 3 gain increase from the central detector (see Section 3.5.2). This was considered sufficient gain reserve.

As it turned out, our flight unit was a last minute replacement with no long term history. This PMT was subjected to accelerated aging at high anode currents as shown below:

Aging of PMT No. P2024 at High Anode Currents

Time on	Average I_A	Relative Output
0 hrs	11.5 μA	100%
20 hrs	7.6 μA	66%
115 hrs	7.0 μA	60%
130 hrs	$\sim 0.5 \mu A^*$	64%

*After 115 hours the rate was dropped to about 6% of the initial rate.

During the accelerated aging the flight unit PMT was seen to drop by about 40%. Because of the high average anode current and the large drop in output, this was considered permanent aging, and the tube was not tested again to see if it had recovered. It is likely, judging from the behavior of the PMT in orbit, that it did recover at least somewhat.

The x-ray PMT's were handled in a manner similar to the shield PMT's.

3.3.2 Signal Conditioning

This section details the analog signal processing circuitry with the exception of the analog housekeeping data, the log count rate meters (LCRM's), and the pulse height analyzer (PHA).

3.3.2.1 Central Detector Signal

The central or main detector is a high resolution NaI(Tl) gamma ray spectrometer consisting of a 3- by 3-inch cylindrical crystal coupled to an RCA-C31009 photomultiplier tube (PMT) (Higbie et al., 1972). The anode and dynode string are supplied by two dependently variable high voltage supplies (see Section 3.1.4). Resistive cross-coupling allows operation of the tube in the event that either of the two supplies malfunction. Signals are obtained from dynodes 9, 10, and the anode and carried to the electronics via individually shielded cables. A temperature monitor, consisting of a precision thermistor and matched resistor network, indicates central detector temperatures over the range -50° to 100°C .

Each signal is capacitively coupled from the appropriate tube element to the output cable. A resistor references the output cable to ground to prevent voltage overloads when the cables are disconnected and connected. The signal polarity is negative for the anode signal and positive for the dynode signals.

3.3.2.2 Cup Detector Signal

The CsI(Na) shield, which consists of a large cup and a front slab, is viewed by five PM tubes (RCA-70132B, hemispherical photocathode), three of which are arranged around the front end and one at the rear end of the cup, and the fifth views the front slab of the shield and an Am^{241} calibration source. All five tubes are supplied from the shield HVPS which is fixed. A single output from each tube's anode (negative signal polarity) is coupled to the electronics package.

The signal from each of the four cup PM tubes is coupled to a single current amplifier through individual surge limiters and gain compensation networks. The surge limiters are identical to the one described above, and the gain compensation consists of a parallel trim resistor which shunts a portion of the signal current to ground, and a standard 200 Ω resistor which provides isolation between trim resistors. Each 200 Ω resistor connects to the summing junction of the current amplifier. The current amplifier output drives two signal paths; one directly into a threshold circuit (through a dc restorer) for veto pulse stretchout and the other through two RC differentiators and two voltage amplifiers into the lower level threshold circuit and retriggerable one-shot. Amplifier gains are adjusted so that the lower level discriminator trips at

200 keV nominal, and the upper level discriminator trips at 2 MeV. The latter discriminator provides a variable pulse width to allow recovery time for all amplifiers during high energy loss events. The lower level discriminator is adjusted to 0.5- μ sec width and each firing during the PHA quadrant is recorded by the cup LCRM's. The remaining logic is discussed in Section 3.3.2.4 after the remaining charged-particle event inputs are developed.

The signal from the main channel PM tube anode is coupled to a charge-sensitive amplifier through a surge limiter network. This network consists of a series resistor and parallel diodes designed to limit voltage transients to +0.7 and -1.4 volts. The charge-sensitive amplifier consists of a charge-sensitive preamp (CSP), two shaping amplifiers, and a postamplifier. The CSP integrates the input signal, providing a time measure of the energy released within the crystal.

The feedback elements are 30 pF and $10^6 \Omega$, yielding a time constant of 30 μ sec and a gain of 33 mV/pC. The dual shaping amplifiers provide double delay line clipping with a time constant of 2 μ sec, resulting in a bipolar pulse of approximately 4 μ sec duration and reasonably flat tops (approximately 6% droop). This waveform minimizes noise effects, and maximizes linearity and stability. A second signal path from the CSP utilizes double RC differentiation with small time

constants (0.3 and 0.8 μ sec) to minimize the pulse pair resolution time. A postamp provides sufficient gain (selected at test) to trip one discriminator at 300-keV equivalent incident energy loss, while a second discriminator is adjusted to trip at 9.1-MeV equivalent incident energy loss. The upper level discriminator duration is 2 μ sec and the lower level is set to 0.5 μ sec and delayed by 0.7 μ sec to act as a strobe pulse for the gamma separator logic.

The gamma separator logic consists of three conditional paths: two for gammas in the 0.3-9.1 MeV range and one for gammas greater than 9.1 MeV. The latter path requires the presence of the 0.3-MeV discriminator, the 9.1-MeV discriminator, the anticoincidence line [high or on except during radioactive source calibration (RS cal)], the PHA quadrant line (high during valid PHA quadrants), and the absence of a charged-particle event. This combination of events defines a greater than 9.1-MeV gamma event for counting by the log count rate meters (LCRM's).

One of the remaining two paths in the gamma separator is used during radioactive source calibration and requires the presence of the coincidence line (the complement of the anticoincidence line), the PHA quadrant line, the 0.3-MeV discriminator, the Co^{60} discriminator, and the absence of the 9.1-MeV discriminator, and a charged particle event. Thus only true gammas

between 0.3 and 9.1 MeV that coincided with an event detected by the Co^{60} tube and occurred during a PHA quadrant produce an output during RS cal. During the remaining time ($\sim 93\%$) the other gamma path is used, which requires the same events as the RS path, except that anticoincidence must be high, and coincidence and Co^{60} inputs are not used. The true gamma output (summation of last two paths described) is used to start the PHA and is tallied by the two 0.3-9.1 MeV LCRM's.

3.3.2.3 Slab Detector Signal

The signal from the slab PM tube is coupled to a current amplifier through a surge limiter of the type previously discussed. The current amplifier output is differentiated ($\tau=0.5 \mu\text{sec}$) and amplified for threshold discrimination at 200 keV. The discriminator one-shot provides a $0.5\text{-}\mu\text{sec}$ pulse to a retriggerable (or updating) one-shot, which generates a pulse that remains high for $2.5 \mu\text{sec}$ after the last received input.

For example, two events spaced $2 \mu\text{sec}$ apart would cause an output pulse lasting $3.5 \mu\text{sec}$ (second pulse arrives prior to timeout from first pulse), while two events spaced $3 \mu\text{sec}$ apart would cause two output pulses lasting $2.5 \mu\text{sec}$ and spaced $0.5 \mu\text{sec}$ apart (second pulse arrives after timeout from the first pulse). This circuit may be contrasted to an ordinary one-shot which would ignore the second pulse in the first example above. The updating one-shot input is also gated with the PHA quadrant signal and presented to the slab LCRM's.

3.3.2.4 Co^{60} Detector Signal

The Co^{60} source consists of a scintillating material viewed by a separate RCA-701232B tube. Since the gamma rays from this source are coincident with the emitted charged particles, the calibration line may be electronically rejected or selected. The electronic construction of this detector is similar to the others. This tube is also powered from the shield HVPS and has a signal output as described above. See Appendix (An Electronically Gated Gamma And X-Ray Calibration Scheme).

This signal is handled exactly the same as the slab signal except the differentiator time constant is 200 nsec instead of 500 nsec, and the discriminator one-shot is set to 1.0 μsec instead of 0.5 μsec . No updating one-shot is used and no LCRM is provided. The Co^{60} discriminator pulses are gated with the anticoincidence line and presented to the cup updating one-shot along with the cup lower level discriminator pulses, providing nominal 2.6- μsec outputs.

The charged-particle dead time indicator is high (dead) when any of the following circuits are activated during a PHA quadrant:

1. Cup upper level discriminator ($> 2 \text{ MeV}$). This pulse remains on (low) until the cup output falls below the 2-MeV level.

2. Slab updating one-shot.
3. Cup and Co^{60} updating one-shot.

This charged-particle dead time indicator is delayed slightly and provided to the gamma separator logic discussed in Section 3.3.2.2.

3.3.2.5 X-ray Detector Signal

A separate thin (1/4 inch) NaI(Tl) crystal is viewed by an RCA-4461 PM tube and acts as a detector for low energy solar x-rays. This tube is also powered from the shield HVPS and has a signal output as described below.

The signal from the x-ray PMT is coupled to a current amplifier through a surge limiter of the type previously discussed. The current amplifier output is differentiated ($\tau=0.3 \mu\text{sec}$) and amplified. The signal is presented to a programmable attenuator which provides four levels of attenuation by means of three switches (the fourth position is all switches off). The least attenuation is given an arbitrary value of 1, and the other three levels are trimmed to provide attenuation of 2, 4, and 8. The signal is amplified and buffered and presented to the lower level discriminator. The buffered signal is then attenuated by a factor of 2, buffered, and presented to the upper level discriminator. The lower level discriminator one-shot is used as a strobe by delaying its 0.5- μsec signal by 0.7 μsec . The upper level discriminator one-shot is set to 1.5 μsec , allowing excellent overlap with the delayed 0.5- μsec strobe.

The net effect is that of a single channel analyzer with a dynamic range of 2 to 1 which may be moved to any of four contiguous energy bands under program control. The nominal energy bands are 7.5-15 keV, 15-30 keV, 30-60 keV, and 60-120 keV.

Two counting modes are provided. During normal data accumulation (non-RS cal periods), charged-particle events cause rejection of otherwise valid x-ray events, while during RS calibrations only those x-ray events occurring coincident with a charged-particle event will be accepted. Both modes of operation reject x-ray events that do not occur during the correct PHA quadrants.

3.4 Low Voltage Power Supply

The low voltage power supply (LVPS) is a pulse width regulated supply for higher efficiency of operation. The LVPS converts the spacecraft +19 volts into the required instrument operating voltages. The 19-volt supply from the spacecraft is passed through a simple LC π filter to the output transformer, the other end of which is switched towards power return. The rate and duration of switching is controlled by the clock and control logic. The clock, in addition to driving the primary driver transformer, furnishes a start pulse to the regulator, which is then delayed and returned to the control logic as the stop pulse. The amount of delay is determined by sensing the 13 volts and stop pulses are coupled by two transformers, which also isolate power ground from experiment ground.

The following output voltages are furnished (postregulation is performed where indicated):

Output	
20 volts	
15 volts	(postregulated)
12 volts	(postregulated)
8 volts	
6 volts	(postregulated)
5 volts	
- 5 volts	
- 6 volts	(postregulated)
-12 volts	(postregulated)

ORIGINAL PAGE IS
OF POOR QUALITY

Each output voltage is filtered with a simple π filter.

In addition, two alternate 19-volt dc power sources (keep-alive voltage and orbit-power sense) are applied to the power supply. The keep-alive voltage keeps the input filter capacitors charged through 10 k Ω to prevent a surge of charging current when power is first applied. The orbit-power sense accomplishes two functions: It supplies auxiliary power through a diode in the event of interruption of the 19-volt power; also the orbit-power sense is regulated to 5 volts to supply power for the clock and control logic, which are referenced to power ground.

The following is a basic description of the main elements of the low voltage power supply.

Clock

The clock furnishes the basic chopping pulse which is eventually pulse width modulated and fed to the output transformer. It also furnishes the start pulse to the regulator. Part of the clock module Zener regulates the +19 to +5 volts, which is used to power the clock and control logic. These two circuits are on the spacecraft side of the

primary chopper transformer; thus they are power referenced to spacecraft power return. The clock operates at a nominal 5-kHz rate, which is adjustable for optimization.

Control Logic

The control logic processes the clock output so that the output transformer is driven by pulse width modulated pulses, depending on the power output demand. The control logic accepts the stop pulse which is delayed from the start pulse by the regulator, again depending on the power output demand. The stop pulse interrupts drive to the transformer.

The control logic circuit drives the primary driver transformer, which in turn feeds the power limiting transformer and the chopper (output) transformer. The power limiting transformer feeds back a ramp voltage to the control logic which limits the maximum amount of drive to the chopper transformer thus current limiting the power supply. Two transformers couple the stop and start pulses and isolate power ground from experiment ground.

Rectifier Filters

The dc output voltages are produced by current passing through the output transformer, half-wave rectifiers, and LC π filters. The use of an x-section filter provides an output voltage that approaches the peak value of the ac potential of the source, the ripple components being very small. Selected filter outputs (mentioned previously) are postregulated to produce the required stable operating.

Postregulator

The -12, -6, 6, 12, and 15 volt outputs are postregulated to maintain voltage stability. These stable operating voltages are necessary for the performance of various circuits in the experiment.

Regulator

The regulator receives the start pulses from the clock and returns them with variable delay as stop pulses to the control logic. The regulator also senses the 13-volt winding of the output transformer (after rectification and filtering). An increase in load, resulting in lowering of the output voltages, causes the regulator to generate a greater delay

in the stop pulse which results in the drive to the transformers being stopped at a later time. Thus the output transformer is driven for a longer period of time, and time integration across the output filter capacitors causes an increase in output voltage to compensate for the higher loading.

3.5 High Voltage Power Supplies

The gamma ray detector contains one fixed and one variable high voltage power supply (HVPS). The fixed supply (shield HVPS) provides approximately 1150 volts (selected at test) to power all PM tubes except the central detector. The variable supply (central HVPS) is matched to the central detector PM tube in terms of center voltage (nominal 1050 volts) and adjustment range (nominal ± 150 volts). The central HVPS additionally contains an incremental supply (nominal 100 volts) that tracks and is referenced to the central high voltage. The adjustment capability of the central HVPS consists of two slightly overlapping ranges of 64 steps each, yielding approximately 100 steps over the nominal 300-volt range.

The following description of the central HVPS identifies twelve major functional areas and lists any existing differences between this supply and the shield HVPS. A system equation is listed under System Considerations (this section, page 3-44).

Switch and Primary Current Limit Circuit

The HVPS is turned on and off via a LPTTL-compatible signal. There is a series switch and a current limiter (which prevents an initial current surge from destroying the series switch). The input current is limited to approximately 60 mA under all conditions.

Oscillator

The oscillator circuit is basically a relaxation oscillator which provides a frequency standard for the HVPS of 7.5 kHz (nominal).

Chopper

The frequency reference drives a flip-flop (F-F) to insure waveform symmetry. The flip-flop outputs are buffered to decouple the output load from the flip-flop feedback path and to increase the drive capability.

Transformer(s)

The central HVPS uses separate transformers for the nominal 1150-volt output and the nominal 100-volt floating supply, while the shield HVPS requires a single transformer. Each

transformer has a center-tapped primary driven by the chopper circuit previously described. The centertap voltage is the regulation mechanism and may vary between 12 and 18 volts during normal operation. Toroidal construction results in higher packing density coupled with wider selection of core materials. The secondary winding, being wound first, is afforded a small amount of shielding by the lower voltage primary winding.

Rectifiers

High voltage fast recovery silicone diodes are arranged in a half-wave sextupler circuit for the 1150-volt secondary and arranged in two half-wave configurations for the 100-volt secondary. One-half of this secondary drives a doubler arranged to be positive with respect to the centertap, while the other half drives a half-wave rectifier arranged negative with respect to the centertap. The nominal 100 volts appears between the positive and negative points. The shield HVPS omits the 100-volt supply.

Filter

The 1150-volt supply uses a compound filter consisting of a parallel capacitor, a series inductor, and a series resistor for each section. Three sections are used, with the inductor omitted in the final section. The 100-volt supply uses a symmetrical filter consisting of a resistor and inductor in each leg and parallel capacitors to ground for each leg. The low side of this supply is connected to the high side of the 1150-volt supply through an inductor. The high side of the 100-volt supply has additional RC filtering. The break frequency is about 600 Hz and the attenuation rate is 400 dB/decade. The ripple frequency is attenuated approximately 40 dB.

High Voltage Divider String

To compare the output voltage to the reference voltage requires dividing the high voltage down to about 6.7 volts. This is accomplished by film-type resistors which have a solid core in order to avoid corona problems. The resistors are purchased in matched sets having an overall temperature stability of division ratio of 10 parts per million/°C or better.

Primary Reference Voltage

A reference voltage is generated by supplying a (nearly) constant current to a Zener diode. The diode, a Fairchild-FCT1122 has a typical temperature coefficient of 0.002%/°C and requires only 100 μ A of current to maintain regulation.

Secondary Reference

The central HVPS utilizes a programmer (see Section 3.5.3) to provide a variable reference input (in addition to the primary reference voltage). The shield HVPS uses 0 volts as its secondary reference.

Error Amplifier

The error amplifier compares the divided-down output voltage (referred to the secondary reference) to the voltage produced by the primary reference. High input impedance is provided by a dual FET transistor, and additional gain is provided by a dual bipolar transistor.

Buffer and Current Limiter

Although the error amplifier provided voltage gain to the error signal, current gain necessary to drive the transformer centertaps is contained in this buffer amplifier. A current limited output stage is adjusted to allow up to three times the nominal current requirement. The 100% voltage feedback provides a maximum reduction in output impedance.

Output Monitor Level Translator

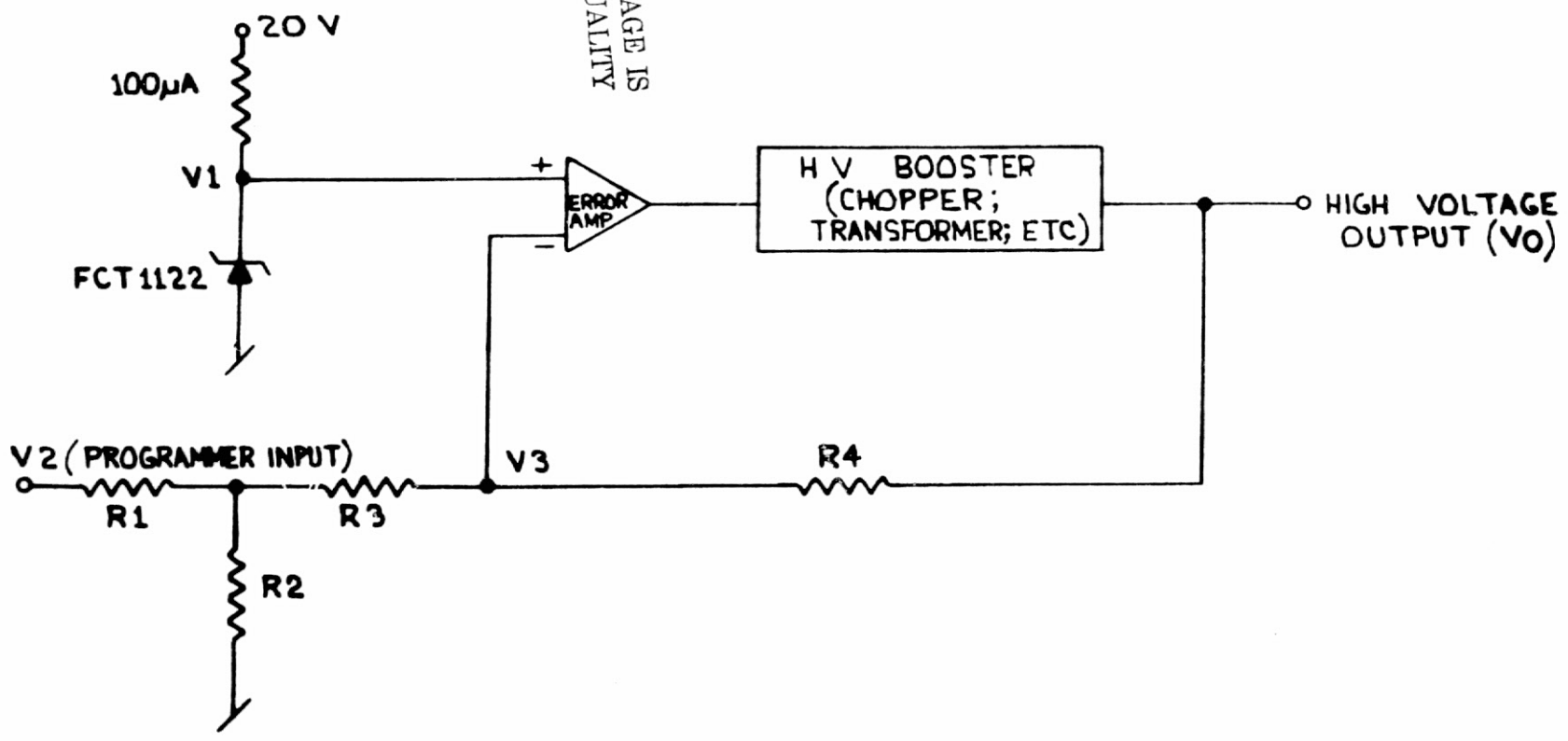
The centertap voltage is approximately proportional to the high voltage output if a slight dependency on load current and temperature is ignored. The nominal range for this voltage is 12-18 volts so that a level translator is required. A resistive divider to -12 volts is used to preserve the voltage swing available at the centertap.

System Considerations

Figure 3.5-1 shows a block diagram of the major elements that affect the output voltage. By using standard operational amplifier notation, the system equation may be expressed as:

$$V_0 = V_3 + \frac{R_4 [V_3 - V_2 (\frac{R_2}{R_1 + R_2})]}{R_3 + (\frac{R_1 R_2}{R_1 + R_2})}$$

ORIGINAL PAGE IS
OF POOR QUALITY



NOTE: V2 = 0 VOLTS FOR SHIELD HVPS

Figure 3.5-1 **Simplified Block Diagram**
Gamma Ray Detector HVPS

3.5.1 Shield High Voltage Supply

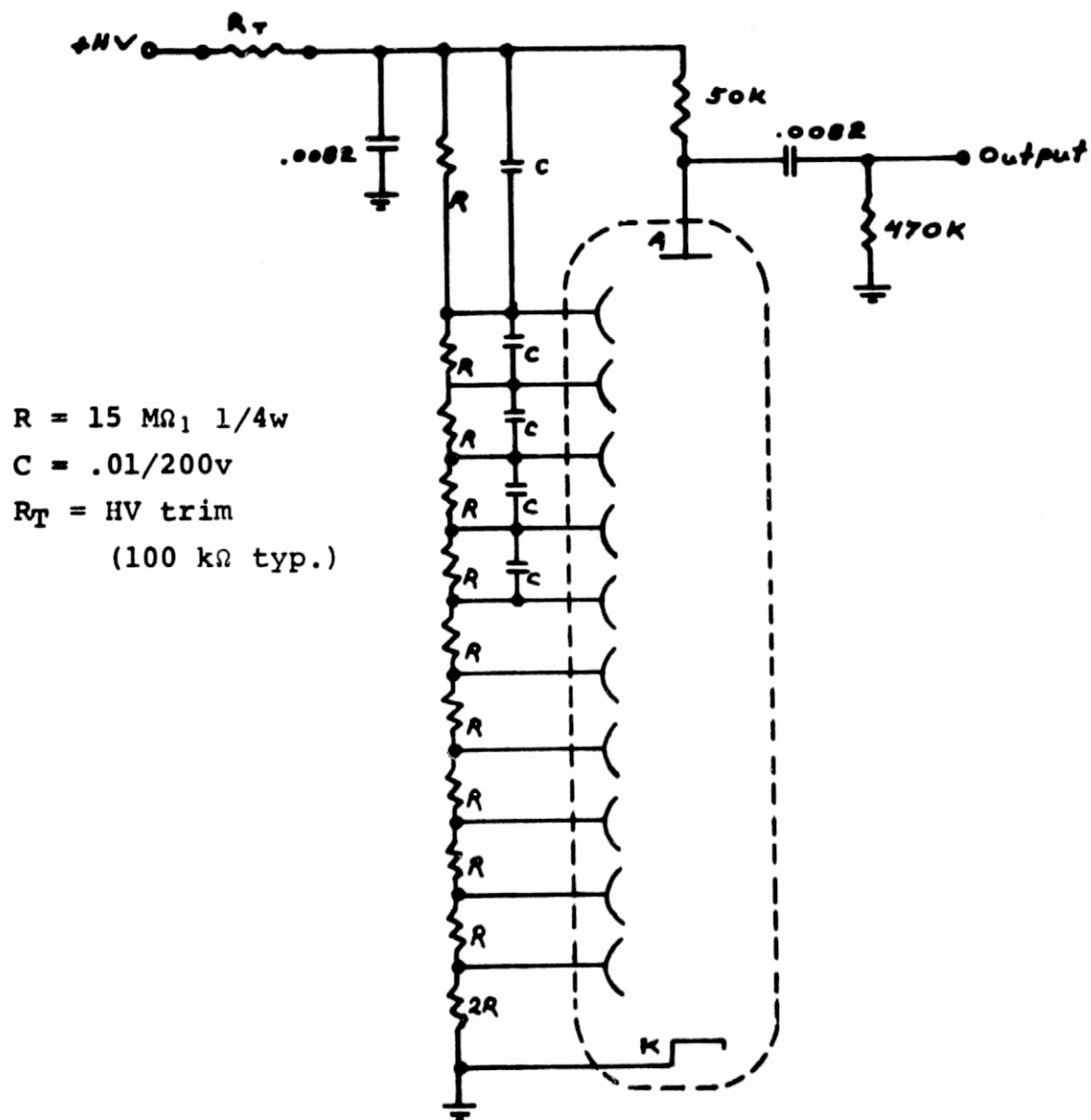
The shield HVPS supplies power to all the shield photomultipliers as well as the Co^{60} calibration source PMT and the x-ray detector PMT. The dynode voltage divider for all the small photomultipliers (shield, etc.) is the same and is shown in Figure 3.5.1-1. The individual photomultiplier voltages can be trimmed by means of a series resistor, as shown in the figure, to compensate for large gain differences between tubes.

The output of the HVPS is fixed (at about 1050 volts) and cannot be adjusted during flight. Likewise all the small PMT's are turned on and off at the same time.

3.5.2 Central Detector High Voltage Supply

The central detector high voltage supply consists of the two-section variable power supply (HV-2 and ΔHV) and a high resistance voltage divider for the dynodes (Figure 3.5.2-1).

The relative output of the flight unit PMT versus total high voltage is shown in Figure 3.5.2-2. The data in this section is based in part on tests (of a backup power supply) conducted after the launch in order to better understand the gain behavior of the detector in orbit.



ORIGINAL PAGE IS
OF POOR QUALITY

Figure 3.5.1-1
Small PMT Schematic

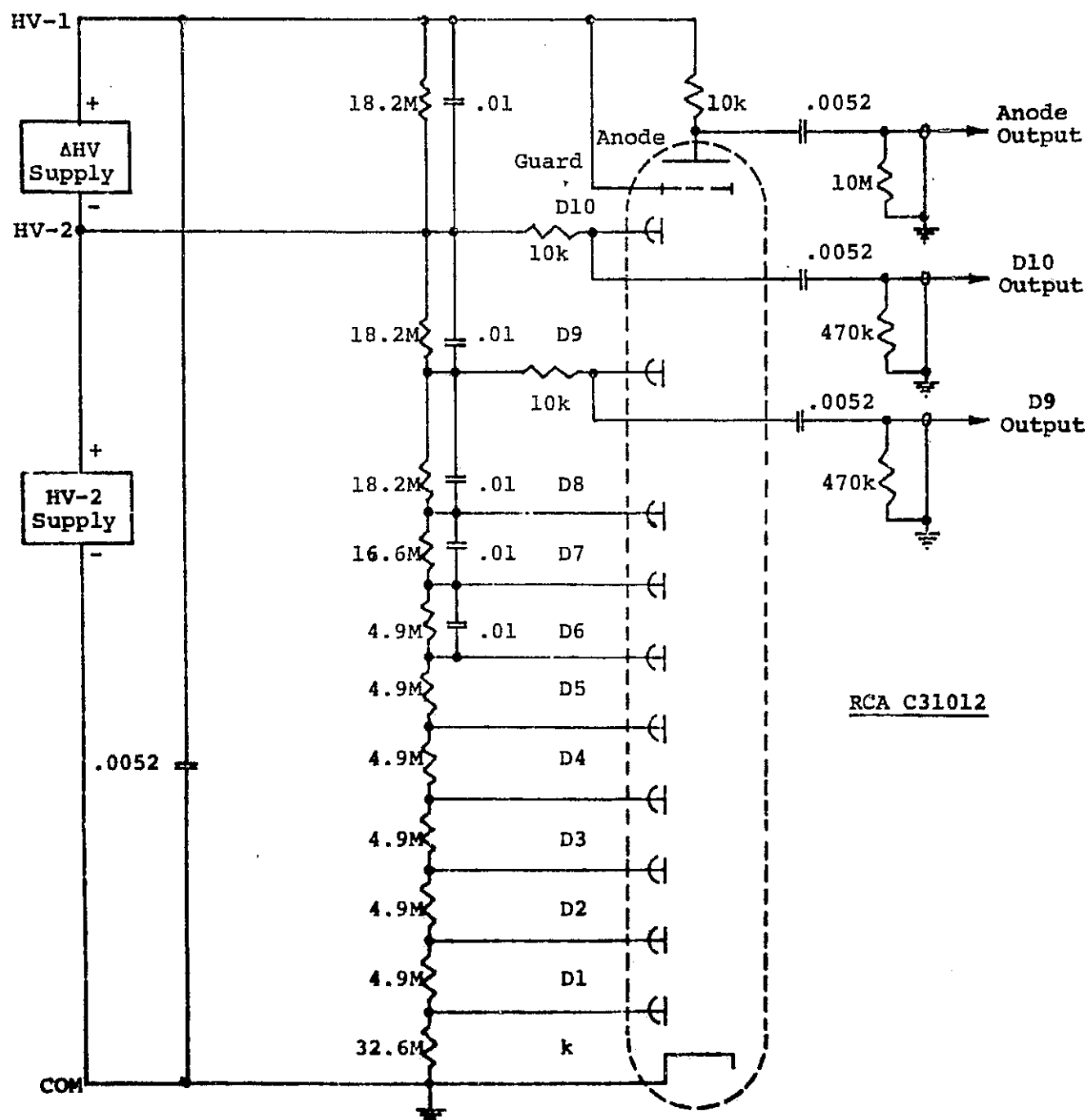


Figure 3.5.2-1

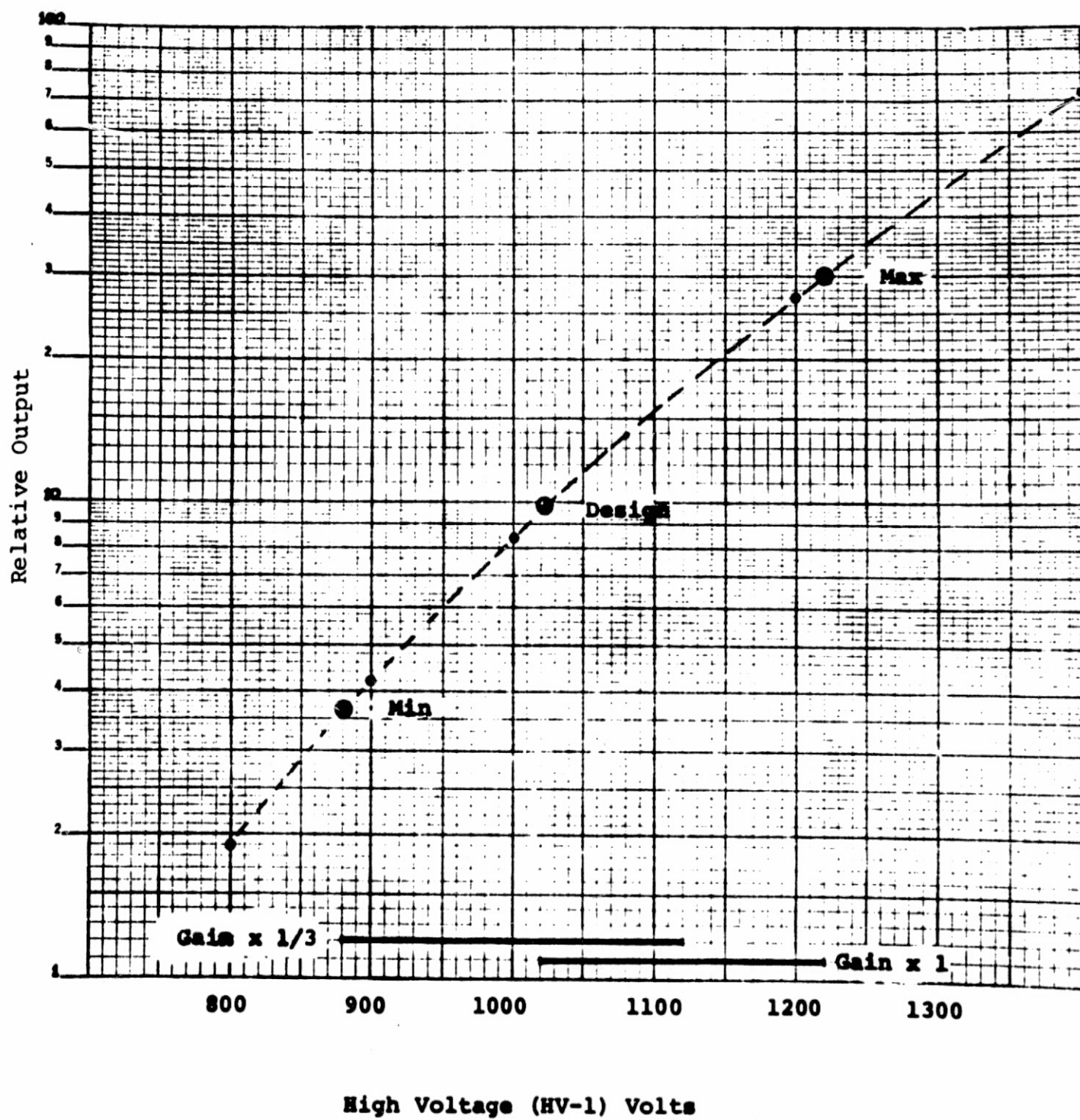


Figure 3.5.2-2

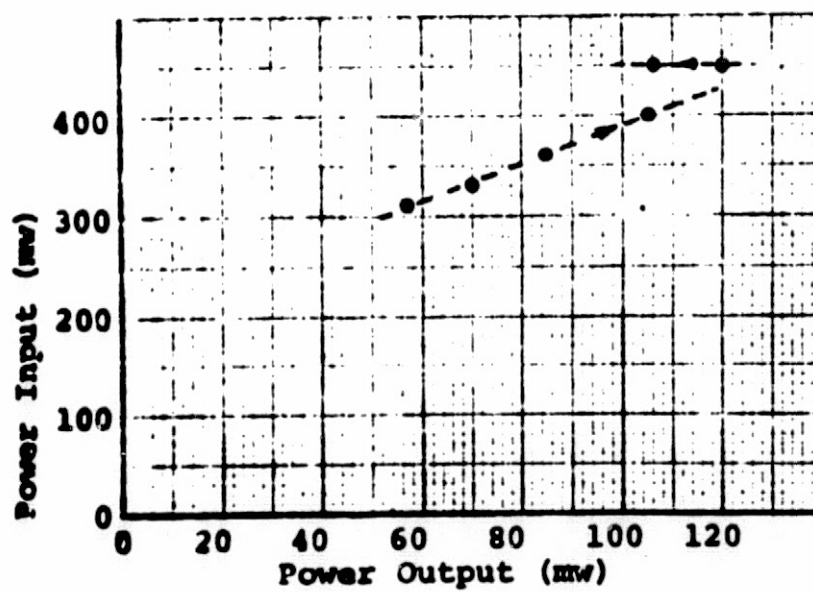
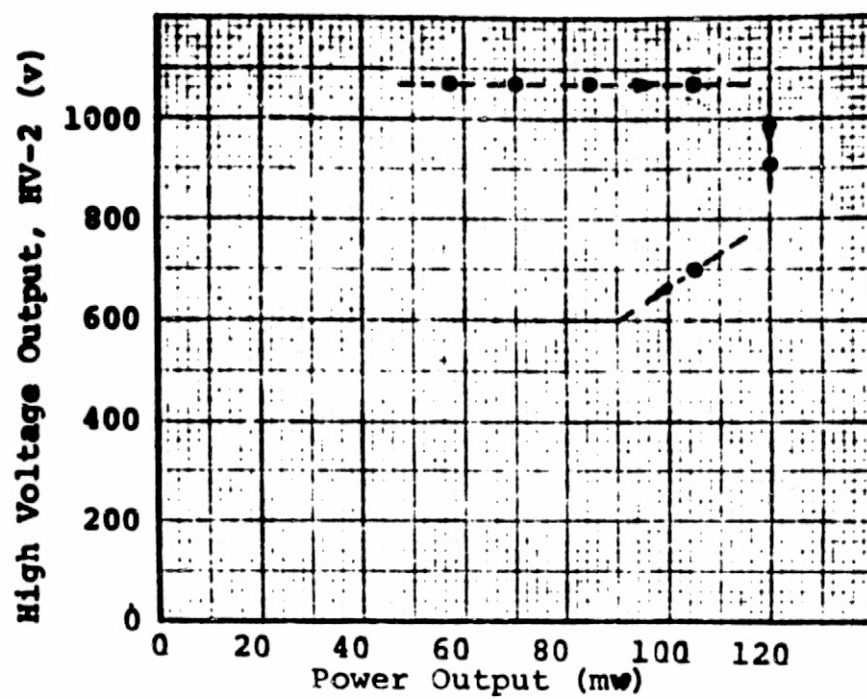
ORIGINAL PAGE IS
OF POOR QUALITY

Originally the central detector was designed with a linear dynode voltage divider of 15 M Ω per stage, but this was changed to the nonlinear divider used in the flight unit in order to improve the energy linearity of the detector.

The HV-2 supply provides regulated voltage to the dynode voltage divider. Δ HV is directly proportional to HV-2; Δ HV was derived from a separate transformer in parallel with the HV-2 transformer and supplies anode current to minimize the effect of anode current variations on the dynode voltage distribution. The result is a fairly stable output level as the counting rate varies. The effect of counting rate on gain is on the order of 2% or less over an order of magnitude rate change.

The output currents of HV-2 and Δ HV are limited by a current limit to the power supply input, which in effect, is a power limit to the dynode divider and PMT combination. The results of the backup power supply (Serial No. 3) tests are shown in Figure 3.5.2-3 and should be similar in the flight unit.

Nominal input to the central HVPS is about 15 mA at 20 volts with an upper limit of about 22.5 mA. The nominal dynode voltage divider current is 10 μ A and is several orders of magnitude greater than the background anode and dynode currents.



ORIGINAL PAGE IS
OF POOR QUALITY

Figure 3.5.2-3

As current in the PMT increases (in high charged-particle flux regions), the upper dynodes begin to shunt some current from the divider thus causing the upper dynode voltages to fall. With HV-2 fixed, the lower dynode voltages have to rise. The net result, as the incident light level is increased, is a slight rise in output (about 5-10%), reaching a maximum when the upper dynode currents reach approximately the nominal divider current. From there the output of the PMT drops sharply as light levels are increased (based on UNH tests using linear dynode voltage distribution). The behavior of the flight unit was not measured under these conditions because the integral crystal assembly did not allow for using light emitting diodes for the high light levels required. It was assumed that the nonlinear voltage divider used on the flight would behave in a similar manner.

The detector average anode current is calculated from the charge collected at the anode per MeV event. This is approximately $2(10^{-11})$ coulombs/MeV event at the design operating point.

The average background current is approximately the same as 100 counts/sec of 1-MeV events. This gives a background current of:

$$\begin{aligned} I_{\text{bkgd}} &= [2(10^{-11}) \text{ coulombs/count}] [100 \text{ counts/sec}] \\ &= 2(10^{-9}) \text{ coulombs/sec} \\ &= (0.002) (10^{-6}) \text{ ampere} \end{aligned}$$

The maximum anode current (disregarding HV supply limits) in the charged-particle regions is calculated on the basis of 10^4 counts/cm²sec of 10 MeV average energy protons (E. G. Stassinopoulos) with a detector effective area of 30 cm². This gives a maximum anode current of:

$$\begin{aligned} I_{\text{max}} &= [2(10^{-10}) \text{ coulombs/count}] [30 \text{ cm}^2] [10^4 \text{ counts/cm}^2\text{sec}] \\ &= 6(10^{-5}) \text{ coulombs/sec} \\ &= 60 \text{ } \mu\text{A} \end{aligned}$$

As indicated above, anode currents of 60 μA or greater are possible on the basis of possible light levels in the crystal. However, it is more likely the PMT output would limit at about 10-20 μA anode current. Likewise the maximum current available to the first dynode is the cathode current plus the current available through the 32.6-M Ω first dynode resistor. This maximum first dynode current would be on the order of 30 μA (assuming collapse of all other dynode voltages to zero).

With the PMT maximum currents limited to about 20 μ A anode (Δ HV) and 30 μ A first dynode (HV-2), it appears that the power supply output current limits would not be reached even in the highest charged-particle fluxes. Actual orbital data bears this out. The HV monitor output does not indicate increased drive to the HVPS.

The actual maximum light level in the crystal is not known at this time; it is not known definitely what happens to our detector and to the spacecraft at the very high charged-particle fluxes. The 10^4 counts/cm²sec of 10 MeV average energy is probably a conservative estimate because it neglects the electron flux and the effects of locally produced photons resulting from high proton flux.

It does appear that the PMT currents would be limited by the PMT and associated HV circuitry and not by the cathode incident light levels.

The flight unit central detector parameters are summarized below:

$$G = k(V)^{6.7}$$

where

G = gain

k = circuit constants

V = high voltage HV-1

HV-1 versus HV steps

Gain x 1/3 (880-1070 volts) (64 steps)

Gain x 1 (1020-1220 volts) (64 steps)

Output at anode (nominal gain)

$$Q = 2(10^{-11}) \text{ coulombs/MeV}$$

Voltage Divider

$$R_T \approx 120 \text{ M}\Omega$$

Average anode current

$$I_A < 0.01 \text{ }\mu\text{A (background)}$$

HV supply maximum current (short circuit, backup unit)

$$\text{HV-2} \quad I_{\text{max}} \approx 200 \text{ }\mu\text{A}$$

$$\Delta\text{HV} \quad I_{\text{max}} \approx 1.2 \text{ mA}$$

3.5.3 HVPS Programmer

The high voltage power supply (HVPS) programmer consists of a digital programmer and a digital-to-analog converter. The digital programmer consists of a command receiver and a 6-bit counter.

Two commands are required for the central HVPS: One is an on/off command and the other is a step command. The on/off command toggles a flip-flop (F-F), which alternately turns the supply on and off during successive commands. The flip-flop is set in the off mode when the instrument is turned on.

There are two modes of advancing the step counter: One could be called the fine tuning mode, and the other, the gross tuning mode. The fine tuning mode advances the programmer one step at a time; data is analyzed to see if the desired tube gain has been achieved. In this mode the actual step is held off until the end of a scan so as not to disturb an accumulation cycle in progress. This is accomplished with a simple latch network where the latch is set by the HV step command and reset by the end-of-scan (EOS) signal. The output of the latch is then used as the input to the counter. This mode of operation would be cumbersome and very time consuming if a large change in high voltage is required. In this case the second mode of operation

(gross tuning) is easily implemented by a two flip-flop network. The first step command received sets the first F-F, enabling the second step command to set the second F-F. The output of this second F-F then simulates the continuous presence of the EOS signal.

This accomplishes two things: It resets the latch thereby advancing the counter once on transition, and the continuous presence of this level prevents normal latch operation because the step command line is looking into a gate which is continuously enabled. Therefore, all following step commands are immediately presented as an input to the counter.

The number of steps actually advanced then would be $N-1$, where N is the number of step commands issued (the first command received sets up the control logic). It should be noted that the setup is cancelled by the EOS pulse. This provides automatic return to normal operation and eliminates the need for an additional functional command.

The digital-to-analog (D/A) converter in the high voltage programmer simply consists of a summing network and an operational amplifier. The conversion equation for the network is represented by:

$$E_0 = R_f V \left(\frac{k_0}{r_0} + \frac{k_1}{r_1} + \frac{k_2}{r_2} + \frac{k_3}{r_3} + \frac{k_4}{r_4} + \frac{k_5}{r_5} + \frac{k_6}{r_6} \right)$$

where

R_f = feedback resistor

V = +5 volts (regulated)

r_1 - r_6 = weighting resistors

k_1 - k_6 are either one or zero corresponding to the 6 bits of the step counter. k_0 and r_0 are included to introduce an offset of either 1.500 volts when the system is in the "normal x 1" gain mode or an offset of 0.000 volts when commanded in the "x 1/3" gain mode.

Chopper transistors are used as switches in the current legs to minimize offset voltages introduced while saturated. An additional operational amplifier with a gain of -1 is used for purpose of transmitting the reference voltage as analog housekeeping data.

3.6 Aspect Timing

This section deals with the quadrant generator and the generation of all aspect-related timing signals. The purpose of the quadrant generator is to provide directional data analysis of the incident particles. A simplified block diagram is shown in Figure 3.6-1.

The operation of the aspect timing follows: The period of each revolution is measured using a 390.625-Hz clock derived from an ultrastable 1.6-MHz crystal oscillator. Spacecraft specification for spin rate variations are from 0.420-0.70 rps. Hence the revolution period count limits are:

$$\frac{390.625}{0.70} \leq \text{Rev. Count} \leq \frac{390.625}{0.420}$$

$$558 \leq \text{Rev. Count} \leq 920$$

These limits allow the use of a 9-bit counter, since the tenth bit is always a one (e.g. lower limit > 512).

ORIGINAL PAGE IS
OF POOR QUALITY

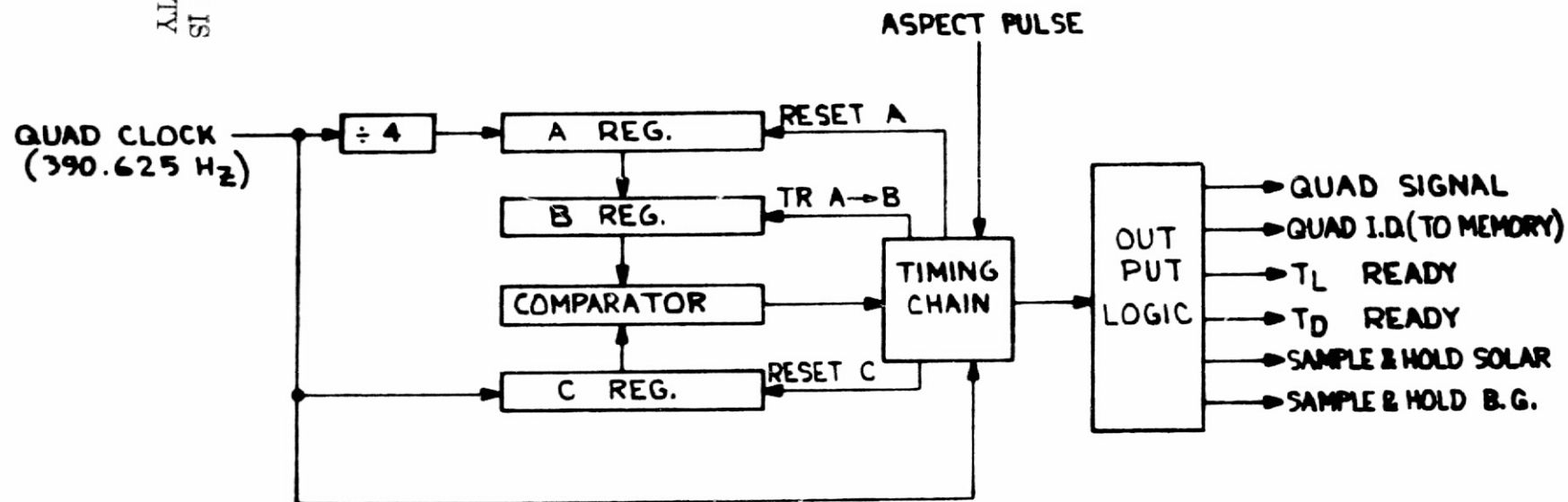


Figure 3.6-1 Simplified Block Diagram
of Aspect Timing

Therefore, the quadrant generator spin rate limits can be calculated as follows:

$$\begin{aligned}
 512 &< \text{Rev. Count} < 1024 \\
 \frac{512}{390.625} &< \text{Rev. Period} < \frac{1024}{390.625} \\
 1.31 \text{ sec} &< \text{Rev. Period} < 2.62 \text{ sec} \\
 \text{or} \\
 0.764 \text{ rps} &> \text{Spin Rate} > 0.382 \text{ rps}
 \end{aligned}$$

At the end of each revolution the A register contains a count representing one-fourth of this period. At this point the contents of A are transferred to B register, which serves as a measure of the quadrant lengths to be generated during the next revolution. It should be noted then that quadrants are always based on the length of the previous revolution. In the event of extra aspect pulses, which could occur during day/night transitions, the quadrant generator would lock back on after completion of the first good aspect pulse period.

The timing chain, consisting of a string of three one-shots, produces the necessary timing signals to cause a change in quadrant signal, transfers the contents of C register into a buffer (for the live time measurement, which will be discussed in Section 3.7), and finally resets C so that the next quadrant can be measured off.

The first three quadrants following an aspect pulse are generated in this manner and are therefore always equal in length. The last quadrant however is terminated at the first clock pulse following the occurrence of the aspect pulse. Termination based on aspect pulse is necessary since the spin rate does indeed change.

The actual termination awaiting the first clock pulse following the aspect pulse is required to maintain absolute accuracy in the live time measurement, since the clock and the aspect pulse are asynchronous.

The output of the quadrant generator is not directly used for the main channel. The quadrant signal is modified by the PHA end-of-scan inhibit.

The purpose of this manipulation is to prevent data accumulation of partial quadrants at the beginning and end of a data scan; this would unduly complicate the live time measurement to be performed. Application of the end-of-scan inhibit decision is based on the following. A latch is set by a signal called MF46L, which corresponds to main frame sync 46 of the last subframe (15.36 sec) cycle. The latch is reset by the first end-of-quadrant (EOQ) signal; the reset transition of the latch toggles a flip-flop thereby inhibiting the quadrant

signal. The MF46L signal occurs 640 msec prior to the end of a scan, which allows sufficient time to complete the worst case longest quadrant if one were in progress at the time.

The inhibit signal is maintained until the start of the first complete quadrant following the end-of-scan signal. Release of inhibit is accomplished in a similar manner as the initiation; the EOS pulse sets the same latch, which is reset by the first EOQ pulse following this event; the reset transition then toggles the flip-flop back to the enabling state.

MF3 (main frame sync 3) pulse is applied to the set input of the flip-flop to insure proper syncing of the inhibit function; this is required since the flip-flop is used in the toggle mode.

In addition to this manipulation, the PHA quadrant signal is forced to be continuously alive during radiation source calibration so that a reasonable number of counts can be accumulated over the period of one scan.

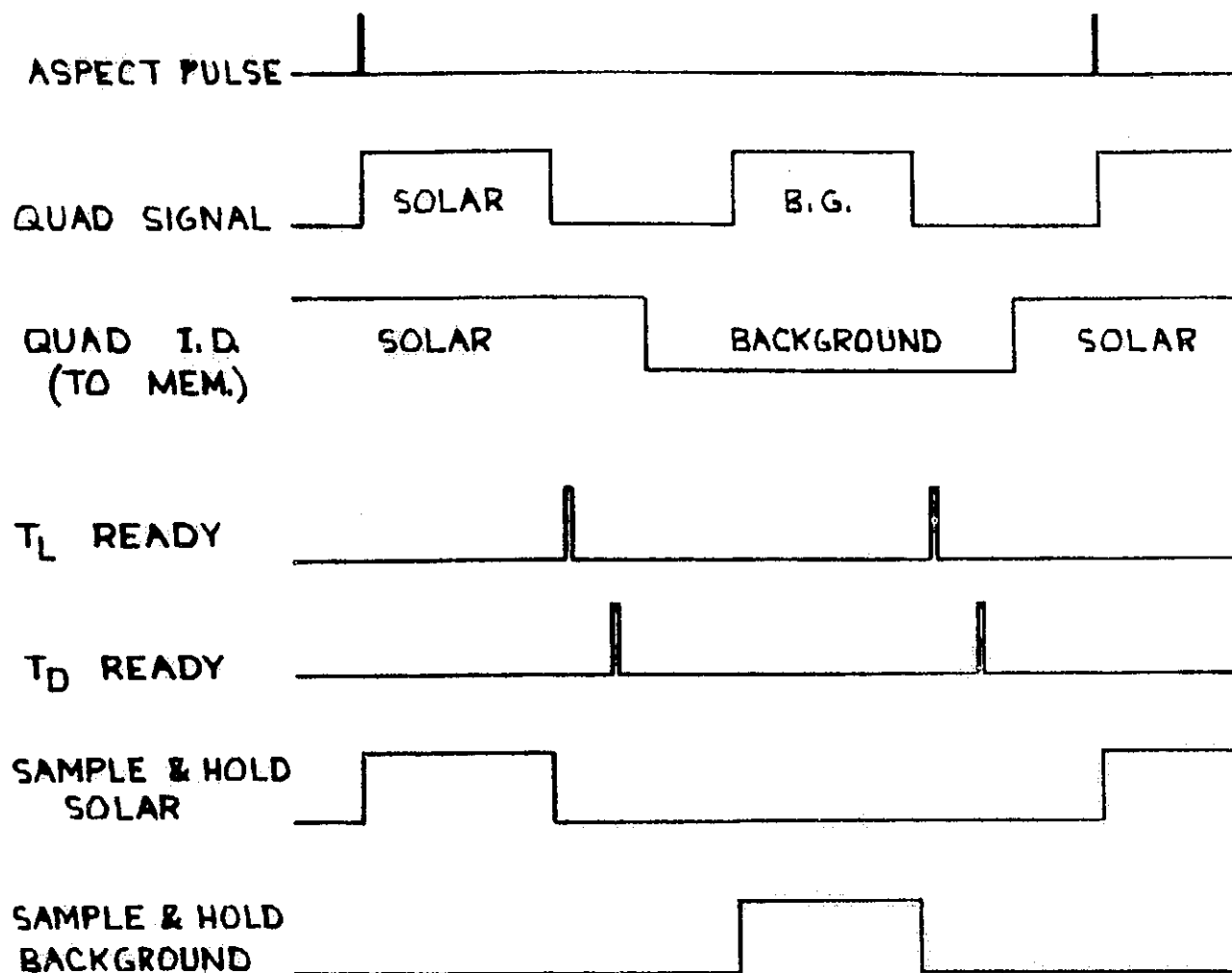
Other aspect-related timing signals generated in the output logic are:

1. Quadrant identification for the purpose of memory addressing for data write-in: This signal differs from the normal quadrant signal because the live quadrants are extended out to the middle of the neighboring dead quadrants. This is done because the live and dead times are written into the memory during the first part of the following dead quadrant and the identity of this data would otherwise be lost.

2. Sample-and-hold signals for solar and background rate meters: These signals consist of a pulse identical in width to their respective quadrants.

3. Live-time-ready (T_L ready) signal: This pulse occurs 10 μ sec after the transition from a live to a dead quadrant and is used as a memory request signal for the live time data.

4. Dead-time-ready (T_D ready) signal: The purpose of this pulse is similar to the live-time-ready pulse but occurs approximately 80 msec into the dead quadrant. Note that a T_D ready signal is issued only if the accumulated dead time has exceeded a certain minimum level. The reason for this is discussed in Section 3.8.1. A timing diagram of the principal signals related to aspect timing is shown in Figure 3.6-2.



ORIGINAL PAGE IS
OF POOR QUALITY

Figure 3.6-2 Aspect Timing (Normal Quadrant Mode)

3.7 Live Time Logic

The purpose of the live time logic is to provide temporary buffer storage of a quadrant length, and eventually update the appropriate memory word accordingly. In addition, it performs a prescaling function to a factor dependent on scan mode. The prescaling factors are:

P = 8 during full scan

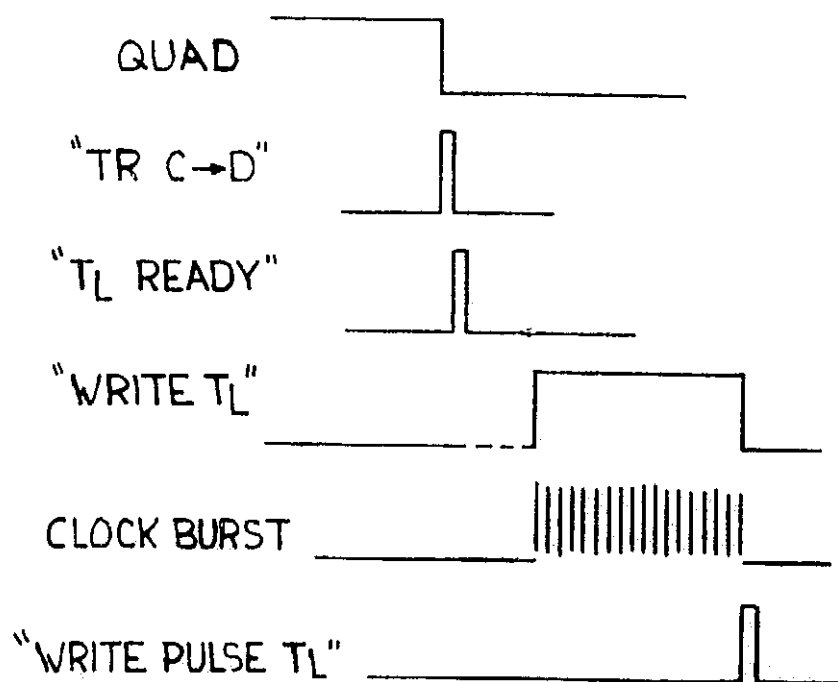
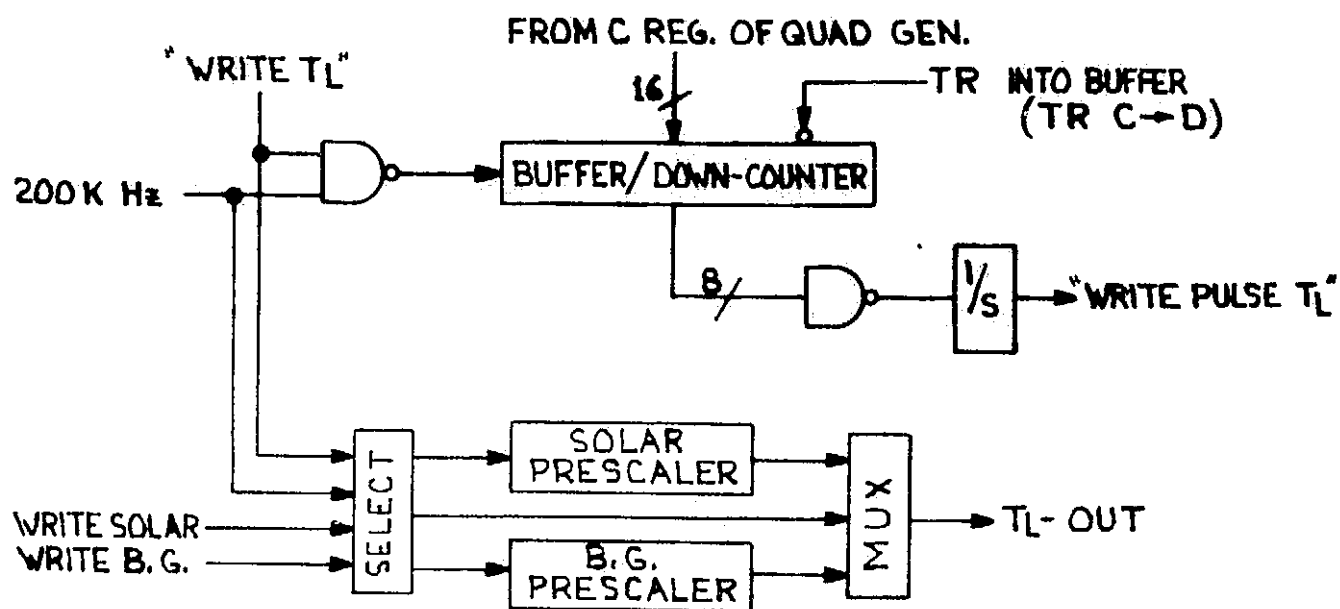
P = 2 during intermediate scan

P = 1 during short scan

It should be noted that two prescaling registers are required since they serve as a true extension of the 12-bit memory buffer and hence are not allowed to be reset until the end of a scan. The error introduced at this point, due to the loss of the prescaler content, is minimal.

A simplified block diagram and timing sequence is shown in Figure 3.7-1.

The remainder of the live time logic consists of an 8-bit register which has a dual function; it is both buffer and down-counter. Quadrant data is transferred in after completion of a quadrant. Memory access is requested by the T_L ready



ORIGINAL PAGE IS
OF POOR QUALITY

Figure 3.7-1 Block Diagram and Timing Sequence
of Live Time Logic

signal discussed in Section 3.6; after recognition by the memory, the previously accumulated data is read out of the memory into the memory data register. At this point an enabling signal called write T_L , which is in sync with a 200-kHz clock, causes countdown of the buffer towards zero by the aforementioned clock.

This pulse train is simultaneously presented to the prescaler, whose output advances the memory data register. A zero-detect gate fires a one-shot and the output pulse signals the completion of the update cycle. This pulse called write pulse T_L negates the write T_L level, thereby stopping the 200-kHz pulse train and simultaneously initiating a memory write cycle.

3.8 Dead Time Measurement

The UNH gamma ray detector uses a direct means to measure dead time to be read out with each spectrum.

Dead time is defined as the time during which the instrument cannot process gamma counts from the detector and includes PHA busy time and shield busy time.

3.8.1 Dead Time Logic

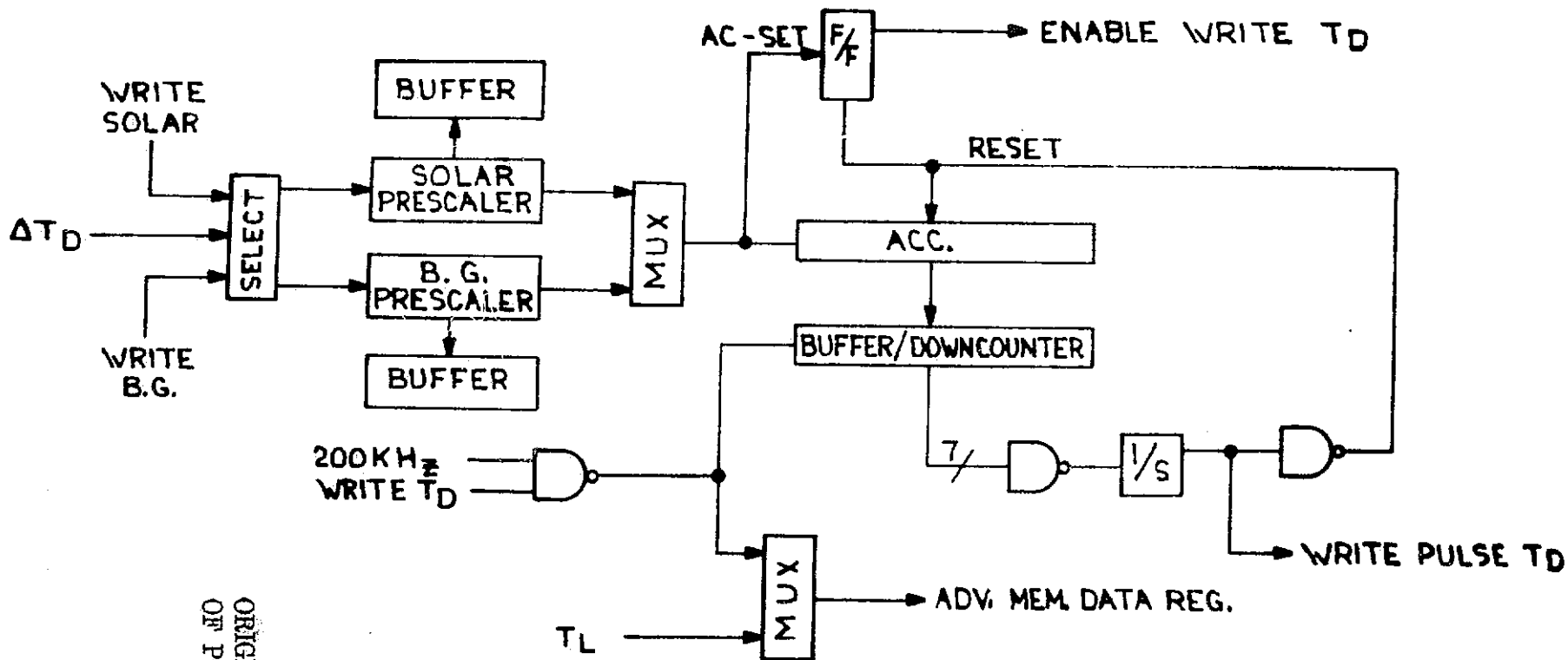
The function of the dead time logic is to accumulate the ΔT_D 's (1.5-msec parcels of dead time) issued by the dead time analog circuitry. To accommodate a maximum dead time requirement of approximately 50%, a 2-bit prescaler is inserted. These two bits are transferred into a buffer at the end of a scan and read out among the status bits. The two prescaler outputs (solar and background) are multiplexed and serve as input to a 7-bit accumulator. Counts accumulated here are buffered in the memory.

Transfer to memory is accomplished in the same manner as that of the live time (see Section 3.7). Contents of the accumulator are transferred into a buffer, which is also a down-counter, at the end of a live quadrant.

Approximately 80 msec into the ensuing dead quadrant, a memory cycle is initiated by the T_D ready pulse discussed in Section 3.6. Update of the memory word consists of a 200-kHz pulse train, which also counts the buffer down to zero. At this point a zero-detect gate fires a one-shot, the output of which terminates the 200-kHz pulse train and causes the write-in of the updated memory word.

A dead time memory cycle is allowed to occur only if the content of the 7-bit accumulator is nonzero (i.e., has accumulated at least one count). This is required since the cycle terminating mechanism consists of a zero crossing detect. Hence if one started with a count of zero, the first zero crossing would occur at the first overflow, in this case, 128 counts.

Implementation of an enabling signal for the memory cycle simply consists of a flip-flop, which is set by the first pulse advancing the accumulator and reset by the zero-crossing-detect pulse. A block diagram of the dead time logic is shown in Figure 3.8.1-1.



ORIGINAL PAGE IS
OF POOR QUALITY

Figure 3.8.1-1 Block Diagram Dead Time Logic

3.8.2 Dead Time Circuit

The function of this circuit is to measure dead time experienced by the main channel. Dead time is defined as the summation of all veto signals applied to the main channel. These signals are:

1. $\gamma > 9.1$ MeV: This veto is applied whenever an incident gamma particle causes the upper discriminator to fire.

2. Charged particle: This signal indicates activity in either the cup or the slab shields, which by system definition yields an anticoincidence veto for the main channel.

3. PHA busy: This signal indicates the processing of a legitimate event. The signal is initiated at the start of a pulse height analysis and terminated after completion of the associated memory update.

4. Inhibit PHA: This signal is generated in the central read/write logic and provides an extension of 5 μ sec to the PHA busy signal to blank out noise generated by the memory turnoff.

These signals are ORed together and presented to the dead time circuit for processing.

Due to the requirement to measure increments as small as 2 μ sec, an analog approach was taken, since an excessively high frequency clock would be required to maintain any kind of accuracy in a digital approach.

A functional block diagram of the dead time analog circuit is shown in Figure 3.8.2-1.

Basic operation follows: Increments of charge, proportional to dead time, are deposited on a capacitor. This is accomplished by allowing a constant current source to charge up a capacitor for the duration of the dead time. Hence time is converted to voltage with the relationship:

$$\Delta V = \frac{I_0 \Delta t}{C}$$

where

I_0 = value of constant source

A comparator continuously monitors the voltage buildup of the capacitor. When this voltage reaches a certain limit, a unit of time has been accumulated. The comparator trips and its output fires a one-shot.

The one-shot pulse advances a digital accumulator and simultaneously causes a dump circuit to discharge the capacitor so that a new unit of time can be accumulated. A unit of time

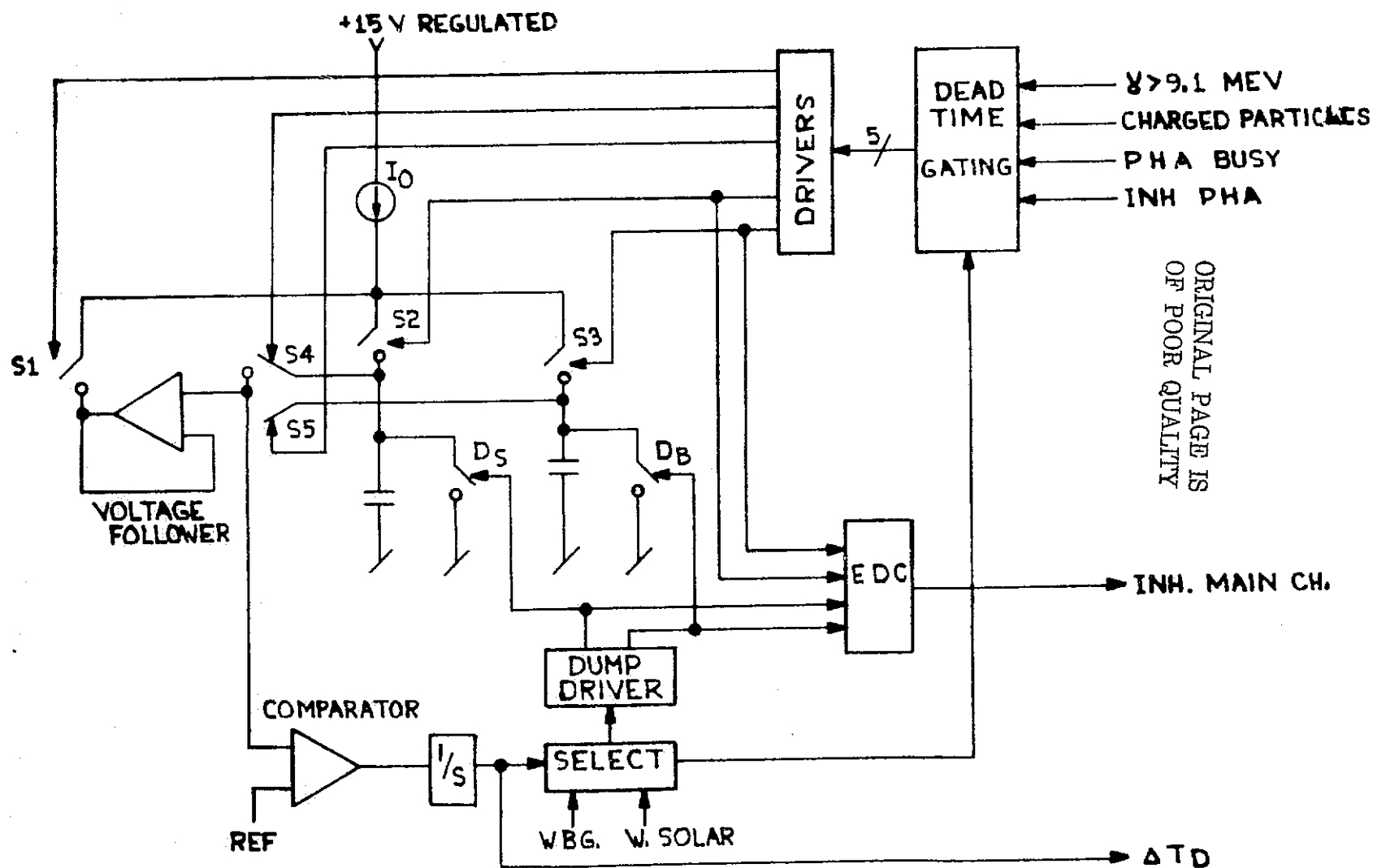


Figure 3.8.2-1 Function Block Diagram of
Dead Time Analog Circuit

corresponds to 1.5 msec; this is consistent with word length availability and accuracy considerations. Two capacitors are required, one each for dead time experienced during solar and background quadrants. The dual system is mandatory since accumulated time short of a unit would otherwise be lost at the end of a quadrant; this would result in gross errors.

This type of error is now reduced to a one-time ambiguity at the end of a scan. Maximum error of this nature would be

$$\frac{1.5 \text{ msec}}{7.5 \text{ sec}} \times 100\% = 0.02\% \text{ in short scan.}$$

Detailed Circuit Description

Dead time pulses are ORed and the output is fed into a gating network that selects the proper switches to be turned on and off. All switches used are MOS-FETS (DM05N), which have extremely low leakage characteristics. These switches are driven by high speed complementary drivers, which have an output swing of 18 volts; 6 volts turns the switch on, while -12 volts turns it off. The gating network is arranged so that under normal conditions (with no dead time present) the current source is looking into a low impedance voltage source, which tracks the voltage of the storage capacitor corresponding to the current quadrant. The purpose of this is to minimize discontinuities in the current source load when switching occurs, thereby increasing the frequency response of the system.

This voltage source is made up of a simple voltage follower, with an FET input to insure high input impedance. The input to the voltage follower is switched from one capacitor to the other in the middle of a dead quadrant so that sufficient time is allowed for the current source to adjust to the new load.

The input is also used by the comparator, which has a 3-volt reference voltage at its other input. When the capacitor has accumulated a charge corresponding to this 3-volt level, the comparator trips and the transition fires a one-shot.

The one-shot pulse activates a dump circuit, consisting of a driver stage and a dump stage. To minimize dump time, the dump stage consists of six transistors connected in parallel (three in the inverted chopper mode and three in the normal mode). The chopper mode transistors insure a low offset and are active primarily toward the end of the dump time.

The normally connected transistors have considerably more gain in their configuration and as such are used to deplete the bulk of the charge. The dump pulse itself is fed back to the gating network to switch the current source from the capacitor to the voltage follower to further increase dump efficiency. To compensate for errors introduced due to inherent propagation delays, both in the logic gating and the analog switch drivers, a network called EDC (extended dead time circuit) is included.

This circuit is no more than a high speed OR gate, whose output is fed back to the main channel as an inhibit signal. Its inputs are the complimentary driver outputs of those switches connecting the capacitors to the current source and the dump pulses. Dump pulses are included because they could extend beyond a dead time interval. As such the dump time is made an integral part of a unit (i.e., 1490 μ sec of accumulated dead time and 10 μ sec of dump time).

Accumulation of these time units, ΔT_D , is performed by the dead time logic discussed in Section 3.8.1.

3.9 Command Mode Logic

The function of the command mode logic is to implement the various modes of operation after receipt of ground commands.

The following is a list of the commandable modes:

1. Scan mode
2. Quadrant mode
3. Gain mode
4. Calibration mode
5. Day/night auto calibration mode
6. Aspect mode
7. Central HVPS mode
8. Central HVPS step mode
9. Charged-particle HVPS mode

3.9.1 Scan Mode

The scan mode determines the length of a data sampling period. The length of time is measured in terms of analog subcom (ASC) frames, where the period of an ASC frame is equal to 15.36 seconds. There are three scan modes:

1. Full scan: This scan requires the full readout of all PHA channels. The length of a full scan equals 12 ASC frames or $12 \times 15.36 = 184.32$ seconds.

2. Intermediate scan: This can equal 4 ASC frames or 61.44 seconds. Due to the reduction in telemetry time now available, only selected channels of the PHA are read out. This is further discussed in Section 3.10.

3. Short scan: This scan equals 2 ASC frames or 30.72 seconds. The same argument with respect to available telemetry time holds true here causing an even further reduction in the PHA data readout.

The command receiver consists of a latch, a modulo 3, and a decode network. In order not to disturb current data readout, the actual implementation of a command received is held off until the completion of a scan in progress. This is accomplished by the latch, which is set by the command and reset by the EOS signal. The reset transition is used to advance the modulo 3.

The three states of the modulo 3 are defined to yield the following sequence after implementation of successive commands:

F → I → S → F → etc.

State 1	State 2	State 3	State 1
---------	---------	---------	---------

where

F = full scan

I = intermediate scan

S = short scan

These are decoded by the decoder and presented to the various parts of the system requiring that information. The instrument turnon mode is full scan.

3.9.2 Quadrant Mode

The output of this logic defines which two quadrants are to be considered live. The normal quadrant mode (NQM) assigns live time to quadrants one and three, where one refers to the quadrant immediately following the aspect pulse; as such this quadrant is labeled solar quadrant and the third is called background quadrant. The alternate quadrant mode (AQM) causes a 90° phase shift of the live quadrants (i.e., the second becomes the solar quadrant, and the fourth, the background quadrant).

The command logic consists of a latch and a flip-flop. The latch is again used to hold off actual mode changes until the end of a scan. The flip-flop alternates between the two modes on successive commands received. The initial turnon condition is the normal quadrant mode.

3.9.3 Gain Mode

The central detector gain is adjusted by changing the central detector high voltage. This is accomplished by a gross gain adjustment (gain $\times 1$ or gain $\times 1/3$) or by a series of small increments (HV step). The central detector HVPS reference is described in Section 3.5.3.

The gain change per step is approximately 3% at the operating point of the detector.

3.9.4 Calibrate Mode Logic

Discussion in this section is restricted to the command receiver; details of the calibration sequence are discussed in Section 3.14.

The commandable in-flight calibration sequence consists of one scan of electronic calibration immediately followed by a scan of radioactive source calibration.

The command logic consists of a command buffer, a modulo 3, and some logic gating to implement the above-outlined sequence. One additional constraint is imposed on the command logic; that is, termination of the calibration sequence in progress after receipt of an additional calibration command.

Operation follows: The command pulse toggles the command buffer F-F "A" thereby enabling a gate to pass EOS pulses to the modulo 3. The mod 3 is at this point still in the 00 state, meaning both electronic and radiation source calibration are off.

The very first EOS pulse changes the state to 01, which enables an electronic calibration sequence. The second EOS pulse changes the state to 10, which turns off the electronic calibration and turns on the radioactive source calibration.

The state of the second F-F in the mod 3 also enables the passage of the next EOS pulse as an input to the command buffer F-F. This third EOS pulse then accomplishes two things: It advances the mod 3 to the third state 00, which corresponds to the off condition of both types of calibration, and it returns the command buffer to the off state, which disables any further passage of EOS pulses into the mod 3. The on condition of the command buffer also enables another gate, passing a second command, if issued, which resets the mod 3, terminating a calibration sequence in progress, while the trailing edge of this command pulse also resets the buffer.

Day/Night Automatic Calibration Mode

The discussion here is strictly limited to the command receiver. Details of the day/night calibration sequence are discussed in Section 3.14. The commandable modes of operation for the automatic day/night calibration are: on and off.

3.9.5 Aspect Mode

This mode selects the spacecraft reference pulse to be used for aspect timing. The command receiver simply consists of a flip-flop which alternately enables the use of the day and night azimuth aspect pulse or the magnetometer pulse. Instrument turnon mode enables the normally used day and night azimuth aspect pulses.

3.9.6 Charged-Particle HVPS Mode

The purpose and implementation of this logic is identical to that of the central HVPS.

3.9.7 Central HVPS Mode

This mode determines the on/off condition of the high voltage power supply. The command receiver consists of a flip-flop which alternately turns the supply on and off. Instrument turnon state is off.

3.9.8 Central HVPS Step Mode

The central HVPS determines the operating high voltage step.

The step command logic is discussed in detail in Section

3.3.2.1.

3.10 Main Frame Sequence

This section deals with the readout control logic, which generates the main frame sequence. The main frame data format follows:

sync	status	PHA data	dead time	N1 N2 N3	live time
------	--------	----------	-----------	----------	-----------

A complete UNH main frame data cycle consists of two such sequences; one each for a solar and background quadrant. The PHA data varies in length as a function of the scan mode. Table V shows the PHA channels readout in two scan modes. Sync and status data are nonmemory data words (i.e., they do not require a memory cycle). Hence status data is real time data thus reflecting instrument conditions at time of data transmission.

Since mode status bits are altered as the instrument mode change is implemented, it should be noted that immediately following a change in mode, an old set of event data is preceded by a new set of conditions.

A simplified block diagram of the readout mechanism is shown in Figure 3.10-1. The memory and control read/write logic blocks are discussed in Section 3.1.5. The data buffer consists of a 12-bit register, which contains memory data.

ORIGINAL PAGE -
OF POOR QUALITY

Table V

PHA Channel Assignments

Intermediate Scan								Short Scan			
PHA Data Word	1	31	87	61	152	91	273	1	1	31	91
	2	32	88	62	153	92	281	2	17	32	92
	3	33	89	63	161	93	289	3	18	33	93
	4	34	90	64	169	94	290	4	19	34	94
	5	35	91	65	177	95	291	5	20	35	95
	6	36	92	66	185	96	292	6	21	36	96
	7	37	93	67	193	97	293	7	22	37	97
	8	38	94	68	201	98	294	8	23	38	113
	9	39	95	69	209	99	295	9	24	39	129
	10	40	96	70	217	100	296	10	25	40	137
	11	41	97	71	225	101	297	11	26	41	138
	12	42	105	72	233	102	298	12	27	42	139
	13	43	113	73	234	103	299	13	28	43	140
	14	44	121	74	235	104	300	14	29	44	141
	15	45	129	75	236	105	301	15	30	45	142
	16	46	137	76	237	106	302	16	31	46	143
	17	47	138	77	238	107	303	17	32	47	144
	18	48	139	78	239	108	304	18	33	48	145
	19	49	140	79	240	109	305	19	49	49	146
	20	50	141	80	241	110	313	20	65	50	147
	21	51	142	81	242	111	321	21	81	51	148
	22	52	143	82	243	112	329	22	82	52	149
	23	53	144	83	244	113	337	23	83	53	150
	24	54	145	84	245	114	345	24	84	54	151
	25	55	146	85	246	115	353	25	85	55	152
	26	56	147	86	247	116	361	26	86	56	153
	27	57	148	87	248	117	369	27	87	57	161
	28	58	149	88	249	118	370	28	88		
	29	59	150	89	257	119	371	29	89		
	30	60	151	90	265	120	372	30	90		
						121	373				

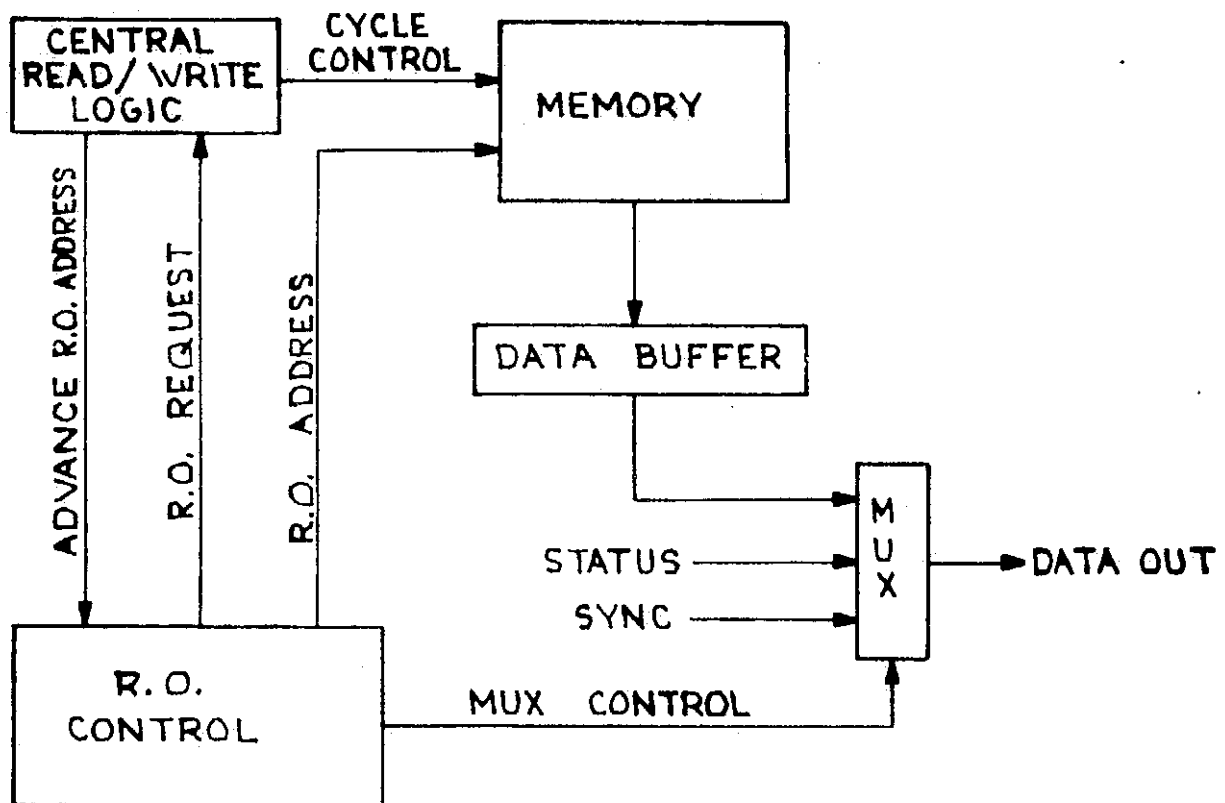


Figure 3.10-1 Block Diagram Main Frame Data Control

transfers. The data buffer is required, since the memory is also used for real time data accumulation. The data multiplexer consists of a gating network, which selects the appropriate data source for readout.

The readout control block performs two basic functions: It generates the memory read request along with the proper memory address, and it controls the data multiplexer. A modulo 12 count shows the number of bits per UNH data word. The outputs of this modulo 12 perform the bit sampling task in the multiplexer. A decoder detects the completion of a data word transmission and generates the memory readout request signal called "readout ready."

In addition, a detect bit number 1, 5, or 9 is used to synchronize a 2-bit counter, which divides the 800-Hz bit rate clock by four.

3.11 DSM Data Processor

The DSM data processor controls and handles all x-ray related data. A complete DSM data sequence is shown in Figure 3.11-1. The sequence consists of four sets of x-ray data, each covering a prescribed energy window. Each dataset represents a one-revolution sample.

The telemetry space available to UNH allowed for quadrant time readout of one revolution only per two sets of data. The two revolutions are spaced close enough in time, however, so that they can be considered equal for the purpose of rate calculations.

The sync ID serves as a sync for the data stream and also identifies the following two sets of data as belonging to the two lower or higher energy windows.

Overall sequence timing pulses are derived from a main frame sync counter. Timing pulse generation can best be understood from Figure 3.11-2.

A single one-shot can be used in this configuration as long as no two consecutive states of the counter are required to produce a timing pulse. The decoder outputs are ORed so that a transition of any one produces a one-shot pulse. The one-shot pulse is then ANDed with the inverted decoder outputs, which directs the pulse onto the proper line.

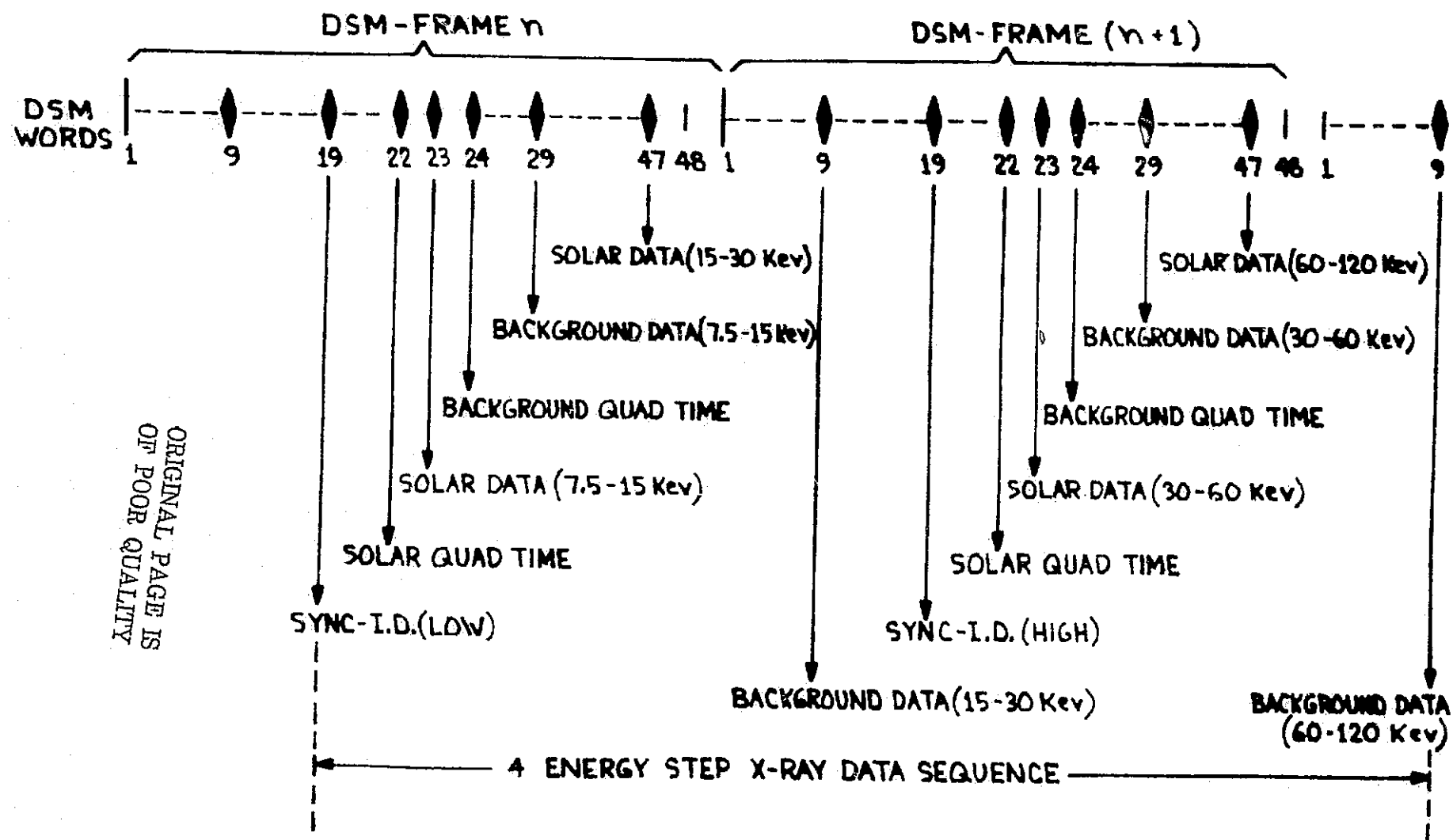
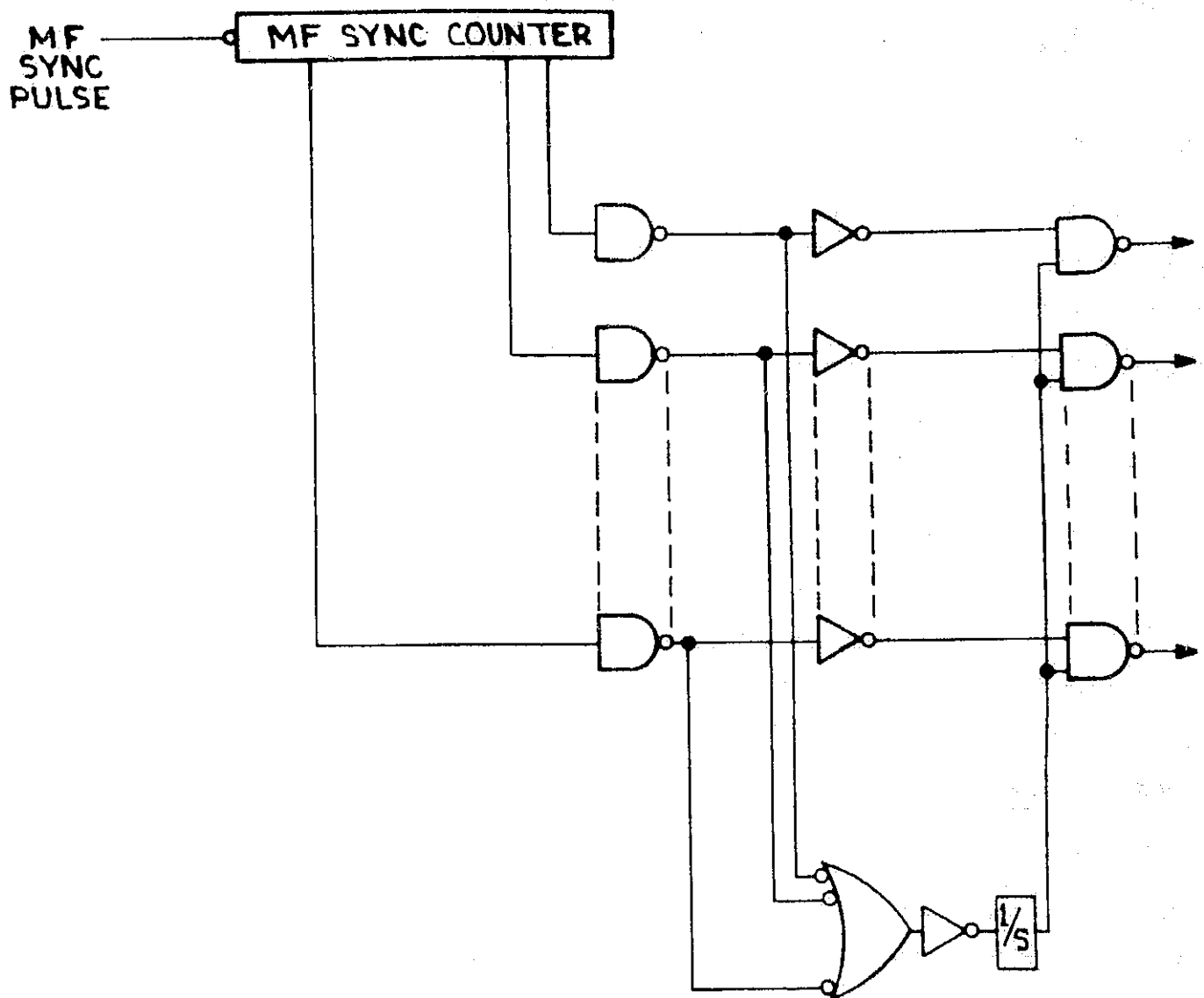


Figure 3.11-1 DSM Data Sequence



ORIGINAL PAGE IS
OF POOR QUALITY

Figure 3.11-2 Main Frame Sync Timing Generator

A block diagram of the DSM data processor is shown in Figure 3.11-3. As mentioned earlier, x-ray data is sampled during the line quadrants of one revolution at a time.

The DSM quad generator singles out these revolutions based on the main frame sync timing pulses. These data revolutions are initiated by the first aspect pulse subsequent to the occurrence of main frame sync 9 and 30.

The energy window is controlled by a 2-bit counter, which is advanced at the beginning of a DSM frame (WASC) and at main frame sync 30. The counter is synchronized to the main frame data sequence by the EOS (end of scan) pulse (i.e., the first set of data following an end of scan always corresponds to the lowest energy window). The most significant bit of the counter is used for the sync ID.

X-ray events are adaptively prescaled and accumulated in an 8-bit register. Data is transferred to a buffer and presented to a data multiplexer for final readout. The transfer characteristics of the adaptive prescaler are outlined in Table VI.

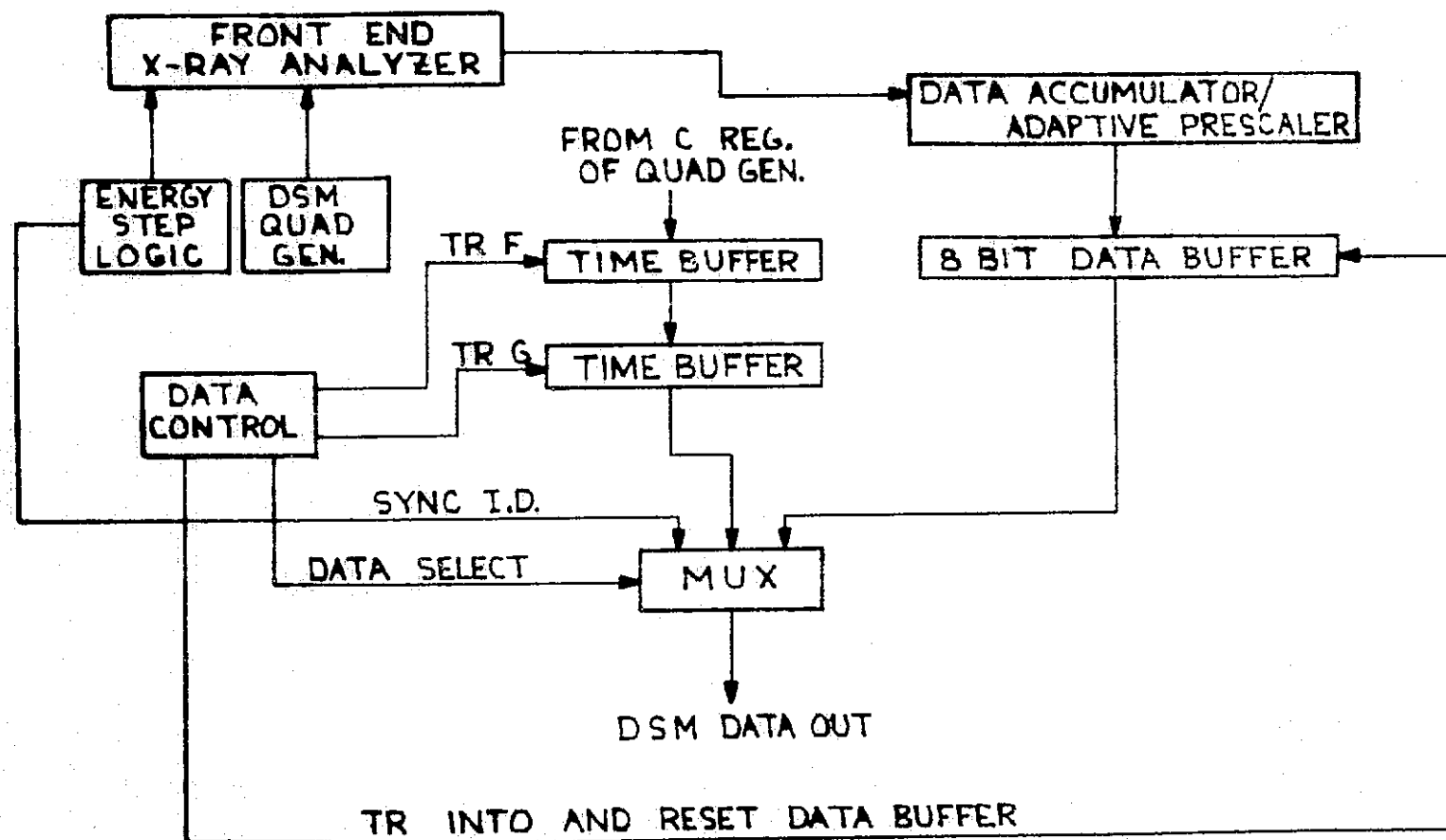


Figure 3.11-3 Data Processor Block Diagram

C _{IN}	P								C _{OUT}	H							
	1	2	3	4	5	6	7	8		1	2	3	4	5	6	7	8
	1	2	4	8	16	32	64	128		1	2	4	8	16	32	64	128
0	0	0	0	0	0	0	0	0	0	0	0	0	0	0	0	0	0
96	0	0	0	0	0	1	1	0	96	0	0	0	0	0	1	1	0
100	0	0	1	0	0	1	1	0	97	1	0	0	0	0	1	1	0
224	0	0	0	0	0	1	1	1	128	0	0	0	0	0	0	0	1
240	0	0	0	0	1	1	1	1	129	1	0	0	0	0	0	0	1
736	0	0	0	0	0	1	1	1	160	0	0	0	0	0	1	0	1
768	0	0	0	0	0	0	0	0	161	1	0	0	0	0	1	0	1
2752	0	0	0	0	0	0	1	1	192	0	0	0	0	0	0	1	1
2816	0	0	0	0	0	0	0	0	193	1	0	0	0	0	0	1	1
18688	0	0	0	0	0	0	0	0	255	1	1	1	1	1	1	1	1

1/1

4/1

16/1

64/1

256/1

Table VI

Adaptive Prescaler

Live time data is extracted from the C register of the quadrant generator. Two-level storage is provided for the live time data instead of one buffer each for the solar and background live time; this reduces the number of gates required in the multiplexer and facilitates the general timing.

The function of the storage control is to transfer the data from the primary buffer to the secondary buffer in a timely fashion. Transfer of the first quadrant (solar) of a data revolution is derived from aspect timing pulses, whereas that of the second quadrant is based on main frame sync timing. Timing of the latter is such that the readout buffer is guaranteed to be empty and sufficient time is allowed until readout of the next data word.

Multiplexer control consists of two types of signals: bit sampling and data source select. Bit sampling signals are generated by the DSM word bit counter, which counts down the number of bits per DSM word gate; data source select signals, on the other hand, are generated by a counter counting down the number of UNH-DSM word gates per DSM frame.

3.12 Analog Subcom Data Sequence (ASC data)

The UNH instrument is assigned 10 ASC words per each ASC frame. Analog data put out on these ten lines consists of eight rate meter outputs (LCRM) and two housekeeping outputs.

This section deals primarily with the latter. The first two ASC words assigned to UNH are subcommutated secondarily and comprise the analog housekeeping data.

A complete housekeeping cycle consists of six sets of these two words. Table VII identifies the housekeeping words in this six-cycle sequence, along with their values, where applicable.

The sequence is generated by a modulo 6 counter, advanced by the WASC (wheel analog subcom sync) signal; the six states are decoded and the outputs serve as the control signal for the analog multiplexers.

The analog multiplexers consists of three stages: drivers, switches, and voltage follower. The driver stage interfaces with the logic through a P-channel FET; this minimizes the load on the logic and simplifies the circuit since no additional components are required to bias the FET. A logic 1 input turns the FET off; this condition yields virtually zero

ASC 11 - Sync = 5 volts	ASC 21 - Detector Temperature
ASC 12 - Scan Mode: Full scan \cong 0.05V Intermediate scan \cong 0.9V Short scan \cong 1.8V	ASC 22 - Electronics Temperature
ASC 13 - Gain/Quad Mode: X 1/3/Alternate \cong 0.05V X 1/3/Normal \cong 0.9V X 1/Alternate \cong 1.8V X 1/Normal \cong 2.7V	ASC 23 - Central HVPS Monitor
ASC 14 - Calibration Mode: Cal Off = 0.05V Electronic Cal. = 0.9V Radiation Cal. = 1.8V	ASC 24 - Charged Particle HVPS Monitor
ASC 15 - HVPS Mode: Both Off \cong 0.05V Central On \cong 0.9V Charged Particle On \cong 1.8V Both On \cong 2.7V	ASC 25 - Low Voltage power supply monitor Preregulator output \div 5 \cong 4 volts
ASC 16 - HV Reference Generator Monitor Gain X1: 1.500 -3.612V Gain X1/3: 0.000 -2.112V 33mV/step	ASC 26 - Day/Night Auto Cal/ Mag. Aspect Enable Mode: Both Off = 0.05V D/N Auto Cal On = 0.9V Mag Aspect On = 1.8V Both On = 2.7V

Table VII

Analog Housekeeping Sequence

base current for the output transistor and the output is therefore at +6 volts. A logic 0 input turns the FET on thereby providing a path to ground, which biases the transistor on, since the emitter is tied to -6 volts.

The analog switches used are N-channel FETS. The switches are connected in such a way as to minimize the load to the analog inputs. (This specification originally came from a "no load" constraint on the high voltage monitor points; this constraint was later removed by the introduction of the high voltage monitor circuits.) A widely used configuration is to insert a high value resistor (say 1 M Ω) between the source and the gate; this would provide the proper on-bias when the diode is back biased. This arrangement, however, would connect the analog source to -6 volts through this resistor when the FET is biased off. To eliminate this load, the gate is returned to the voltage follower output through a 100K resistor.

Turnon is accomplished as follows. (See next page.)

The worst case condition occurs when the multiplexer switches from a low voltage monitor point to a high voltage point.

Assume multiplexer switches from $e_{in_2} = 0$ volts to $e_{in_1} = 5$ volts. This would imply a back bias of 5 volts for S_1 , which would keep S_1 off. However, a 12-volt transient is coupled through the diode capacitance C_{d_1} when the driver changes state. This transient starts to turn on S_1 and e_0 rises towards the value of e_{in} ; this reinforces turnon of S_1 , etc. Hence proper biasing of S_1 is achieved regeneratively. The complementary transient coupled through C_{d_2} does not affect S_1 because it is attenuated heavily by the low output impedance of the amplifier.

The voltage follower simply consists of an operational amplifier preceded by a dual FET input stage. The FET stage is inserted again to minimize the load to the analog inputs. The Zener diode and resistor in the output provide protection against externally induced voltage excursions in the event of temporary fault conditions.

3.13 Quadratic Pulse Height Analyzer

The University of New Hampshire OSO-H gamma ray detector (Higbie et al., 1972) utilizes a multichannel pulse height analyzer (PHA) to analyze the signal from the central gamma ray spectrometer. This PHA is unique because the transfer curve is neither linear nor exponential. An analysis of the resolution versus energy properties of the sensor revealed that the optimum transfer curve should be a quadratic function of the form:

$$E = C(N+N_0)^2$$

where

E = incident energy loss

N = channel number

C = constant

N_0 = constant

A measure of the resolution of the PHA is the number of channels spanning the width of a spectral line (usually at half amplitude). At least three channels are required for adequate data analysis (Purvis and Baggerly, 1968).

3.13.1 Design Considerations

The gamma ray spectrometer used on the OSO-H gamma ray detector has a resolution, R_S , which may be approximately described by the following function (Birks, 1964):

$$R_S = A(E)^{-1/2}$$

where

E = incident energy loss

A = proportionality constant

The resolution, R_E , of any PHA may be generalized by:

$$R_E = \frac{\Delta E / \Delta N}{E}$$

where $\Delta E / \Delta N$ is the energy loss represented by the local channel width at energy E .

Maximum utilization of the entire range of the PHA may be realized by maintaining the PHA resolution at a constant fraction of spectrometer resolution. Therefore,

$$FR_E = R_S$$

where F is a constant having the physical significance that F channels will be seen under the FWHM of any line.

Algebraic manipulation reveals the differential equation:

$$\frac{\Delta E}{\Delta N} = \frac{A}{F}(E)^{1/2}$$

the solution of which yields the optimum PHA transfer curve for this kind of spectrometer. This may be expressed as:

$$N+N_0 = \frac{2F}{A}(E)^{1/2} \quad \text{or} \quad E = \frac{A^2}{4F^2}(N+N_0)^2$$

where N_0 is the integration constant expressed as a channel offset. The channel width may be expressed as:

$$\Delta E = \frac{A^2}{4F^2}(2N+2N_0+1)$$

The scientific objectives of the gamma ray detector specified a dynamic range of 0.3-9.1 MeV and a resolution ratio of approximately 5. An average spectrometer resolution at 0.662 MeV is 8.0%, yielding a value of $A = 0.0651$. These numbers show that 379 channels are required to cover the range of interest. Compromises with telemetry requirements and design practicalities resulted in 377 channels being allocated to cover the range, resulting in an F factor of 4.97. The final calculated transfer function becomes:

$$E = (4.29 \times 10^{-5})(N+83.6)^2$$

3.13.2 Design Implementation

The main channel signal is shaped and amplified so that a bipolar pulse of 0.3-4 volts amplitude appears at the input of the linear gate. The bipolar shaping is used to allow ac coupling without the baseline shift with rate associated with unipolar pulse shapes. The true gamma pulse (see Section 3.3.2.1) interrogates logic to see if the main channel is not busy. If available, the main channel accepts the true gamma pulse as a request to analyze the accompanying analog signal. The linear gate is opened to allow the analog signal to pass into the peak detector, which effectively samples the positive lobe of the bipolar signal. The title peak detector is a misnomer because the circuit does not detect the peak of the pulse but rather samples it according to fixed timing relationships established in the signal shaping networks. A block diagram of the remaining portion of the PHA appears in Figure 3.13.2-1. Capacitor C_1 is charged to peak value of the signal via the peak detector which insures that errors due to incomplete charging of C_1 are negligible.

Concurrently the charge on C_2 is reestablished at its quiescent point via V_{R_2} and R_{limit} . MOS switches change the mode to analyze and I_1 starts to increase the charge stored on C_2 .

$$V_1 = V_{R_2} + \frac{I_1}{C_2} t$$

The operational amplifier causes V_2 to equal V_1 ; hence I_d is determined by V_2 and R_1 :

$$I_d = \frac{V_2}{R_1} = \frac{V_1}{R_1}$$

$$I_d = \frac{V_{R_2}}{R_1} + \frac{I_1}{R_1 C_2} t$$

The charge stored on C_1 is removed by I_d until the comparator recognizes that V_3 and V_{R_3} are equal:

$$V_3 = V_{in} - \frac{I_d}{C_1} t$$

Combining the above equations:

$$V_{in} = \frac{I_1}{R_1 C_2 C_1} t^2 + \frac{V_{R_2}}{R_1 C_1} t + V_{R_3}$$

Comparison of this equation with the desired transfer function of:

$$\frac{V_{in}}{G} = E = \frac{A^2}{4F^2} (N+N_0)^2$$

(where G is spectrometer gain in volts/MeV) reveals the fundamental interrelationships of the various circuit components and constants.

$$\frac{(C_2)V_{R_2}}{2I_1} = N_0 = 83.6$$

$$\frac{I_1}{R_1 C_2 C_1} = \frac{GA^2}{4F^2} = (4.29 \times 10^{-5})G$$

$$V_{R_3} = \frac{V_{R_2}^2 C_2}{4(R_1 C_1) I_1} = \frac{GA^2}{4F^2} N_0^2 = (0.300)G$$

Because only three equations define seven unknowns, some latitude exists for selection of the individual parameters. The spectrometer gain G was set to 0.40 volts/MeV for maximum utilization of the 4-volt dynamic range of the analog circuitry, and I_1 was minimized to maintain the low power dissipation requirement. C_1 was made equal to C_2 to ease procurement of parts. A fourth relationship was obtained by specifying the maximum conversion time allowed.

Selection of component values was aided by computer programs, which analyzed the effects of component values and tolerances on the transfer function. After final selection a computer program provided the calculated boundary conditions for each channel.

Because the PHA rate was expected to be very low, strobing techniques were used to reduce the power consumption. When a command to analyze is received, power is provided to the remainder of the PHA system via the "power on" driver. When the central read/write logic recognizes the PHA event has been recorded, a "power off" signal returns the PHA to the standby mode.

It should be noted that the counting register design forbids the spillover in the event that the PHA attempts to analyze a signal larger than 9.1 MeV, to permit correct analysis of true gamma data in the event of failure of the greater than 9.1-MeV discriminator.

3.13.3 Results

The fabricated units met or exceeded the critical design goals of speed, power, weight, and volume. A typical graph of the measured differential nonlinearity is shown in Figure 3.13.3-1. The data for this plot was obtained from the DNL (differential nonlinearity) computer program described in 4.5. The curvature exhibited by the data suggests a slight deviation from the pure quadratic function. The direction and magnitude indicate that the apparent exponent is approximately 1.99 or about 0.5% low. A small temperature dependency has been noticed for this parameter, but the stability over the expected temperature range remains within the design goal.

The errors shown in Figure 3.13.3-1 may be compared with the $\pm 0.75\%$ to $\pm 1\%$ (upper 98% of the channels) DNL specification of commercial analog-to-digital (A/D) converters (Wilkinson-type) for PHA applications (Nuclear Data, 2200 System Operating Manual; Hewlett-Packard, 5401B Data Sheet). These converters do not exhibit the quadratic transfer function which tends to accentuate DNL errors at the low end of the dynamic range.

ORIGINAL PAGE IS
OF POOR QUALITY

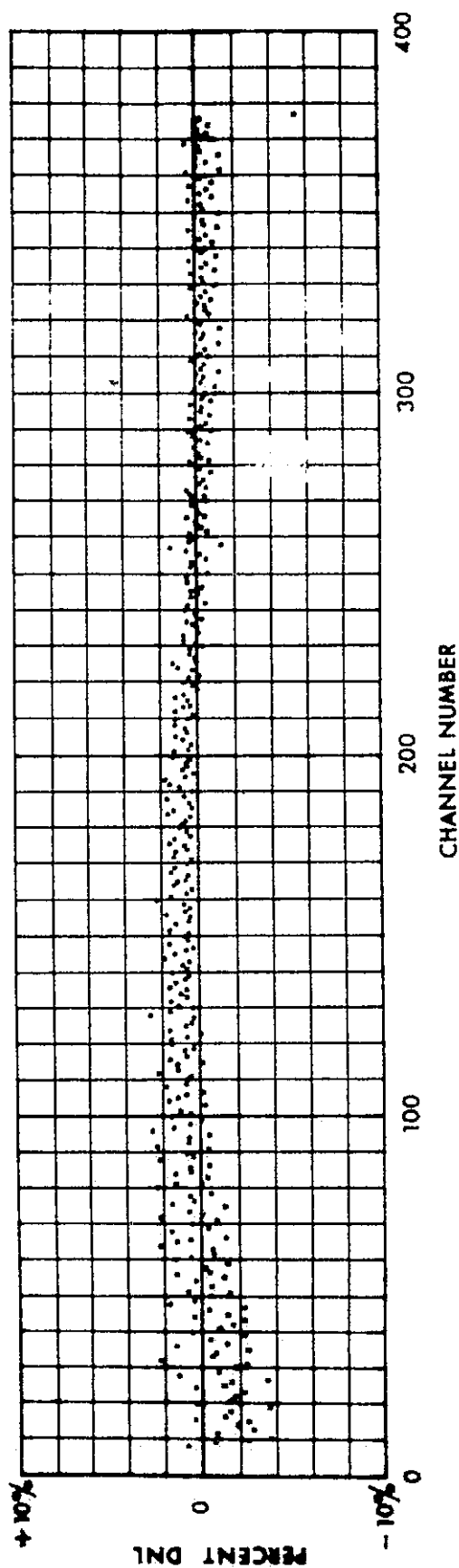


Figure 3.13.3-1 A plot of the differential nonlinearity (DNL) of the quadratic PHA.

Table VIII lists the major specifications of the A/D converter of the PHA.

Figure 3.13.3-2 shows a Co^{60} spectrum produced by the PHA. For this particular test, the programmable high voltage supply for the spectrometer was set to maximum and data accumulated for one hour. Of particular note is the excellent resolution as denoted by the peak-to-valley ratio of nearly 7 to 1.

Table VIII

QUADRATIC PHA SPECIFICATIONS
(Analog to Digital Converter)

Input Voltage Range	0.1171 to 3.6436 volts
Type of Conversion	Height to time using capacitor rundown
Clock Frequency	1.6 MHz (crystal controlled)
Output Format	9 bit binary address (parallel) plus conversion complete pulse
Conversion Time	256 μ sec.

Accuracy:

Temperature Coefficient < .05%/°C

Integral Linearity (to quadratic function)

Channel 100-377 $\pm .25\%$

Channel 10-99 $\pm 1\%$

Differential Linearity

Channel 6-15 $\pm 10\%$

Channel 16-90 $\pm 5\%$

Channel 91-270 $\pm 2.5\%$

Channel 271-377 $\pm 1.25\%$

Power (1000 events/sec) 75 mW

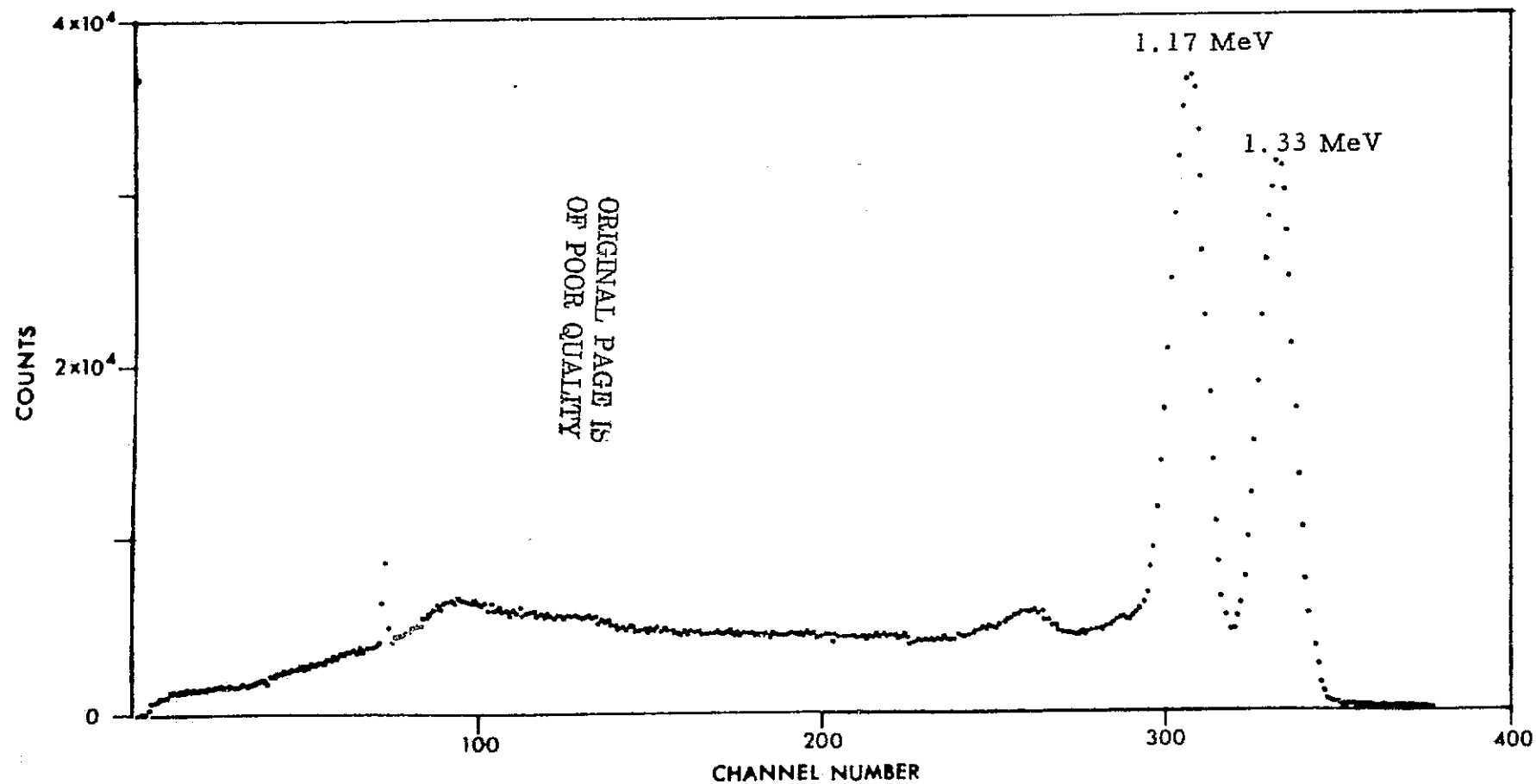


Figure 3.13.3-2

Analysis of Co^{60} by the quadratic PHA. This data was taken prior to the correction of a ground loop problem (the glitch at channel 75). The gain is not set to the nominal 0.3-9.1 MeV range.

3.14

In-flight Calibration (IFC)

The experiment has two calibration systems; one in which built-in radioactive sources are detected and processed and another in which electrical pulses of different pulse heights and frequencies are fed into the pulse amplifiers to check the data-handling system.

During normal operation the experiment is calibrated with the sources twice an orbit. At orbit dawn and dusk the anti-coincidence logic with the front slab and Co^{60} source detectors, which normally rejects gamma rays and x-rays from the Co^{60} and Am^{241} sources, is switched to coincidence. Now only pulses in the central and x-ray detectors which are in coincidence with pulses from the Co^{60} and slab detectors are processed. Because the sources emit coincident particles with the gamma and x-rays, radiation from the sources is exclusively detected. Since the spectra of the sources are known, a complete calibration of the gamma ray and x-ray systems is provided.

The calibration period begins automatically at the start of the first DMF data full scan or 12 telemetry subframes. The calibration period is synchronized with the DMF data blocks so that calibration data would appear in only one full scan data block or an even number of the shorter scan blocks. The automatic calibration function may be inhibited or enabled by spacecraft command.

Transitions of the day/night signal produce one-shot pulses to set a latch, which is reset by the EOS (end of scan) pulse. The reset transition is used to set a flip-flop, whose output is ANDed with the commandable day/night calibration inhibit line. (This command is discussed in Section 3.9.)

The output of this gate is ORed with the commandable source calibration signal. (Operation of the calibration command receiver is discussed in Section 3.9.) The output of the flip-flop also enables the countdown of EOS pulses. The purpose of this counter is to maintain the source calibration for a fixed period of time (independent of the scan mode). The duration of a source calibration is equal to that of a full scan period. Hence the counter and decoder supply the terminating pulse at the appropriate time (i.e., duration of RS cal = 1 full scan = 3 intermediate scans = 6 short scans). Due to the relatively low count rate of the calibration source, the PHA quadrant is forced to be continuously alive for the entire sequence.

3.14.1 Central Detector Radioactive Source

The central detector energy scale is calibrated by means of a Co^{60} source (Forrest et al., 1972). This source is in the form of a small disc (approximately 1/2-inch diameter) of plastic scintillator material with radioactive Co^{60} imbedded in it. The Co^{60} produces gamma rays of 1.17 and 1.33 MeV that are always in coincidence with a beta particle. The betas interact with the plastic to produce light pulses, which are transmitted to a photomultiplier, and thus provide signals which can be used to accept or reject the calibration gamma events. The Co^{60} produces lines at 1.17, 1.33, and 2.50 MeV (sum peak), which are used to establish the PHA energy scale and the quadratic transfer function. In addition, the 1.33 MeV peak-to-valley ratio is an indicator of the energy resolution of the detector.

The Co^{60} gamma leakage amounts to about 5%, which is about the practical limit for this scheme.

In operation the central detector calibration worked quite well.

3.14.2 X-ray Detector Radioactive Source

The x-ray calibration source consists of Am^{241} deposited in a 1/16- by 1/16-inch NaI crystal. The Am^{241} emits x-rays of 59 keV that are in coincidence with an alpha particle. The alpha particle produces a light pulse in the NaI, which is seen by the front slab PMT thus producing signals that can be used to gate the x-ray events.

The scheme was not satisfactory because of very low counting rates in the x-ray detector due to poor geometry.

3.14.3 Electronic Calibration

The electronic calibration is 184.32 seconds (or 12 subframes) in duration, synchronized with the data blocks, and should only be used in the full scan mode. During the cycle pulses of varying frequencies and pulse heights (usually 10% above or below a central detector discriminator threshold or x-ray PHA threshold) are introduced at the central detector amplifiers and γ -ray PHA. The pulses are varied and synchronized with each telemetry subframe. During the sequence detector pulses are inhibited and only the simulated pulses are processed.

The main channel is checked at five energy levels and three frequencies. Five energy levels are used since the PHA requires at least three checkpoints in defining its transfer characteristic; hence three levels are chosen inside the acceptable energy range, while an additional two are placed just outside the upper and lower limit to verify discriminator operation. The three frequencies are mandatory to define the LCRM (rate meter) response.

Table IX illustrates the electronic calibration sequence; for example, during the first DSF, 10-MeV pulses are fed into the gamma ray channel. This is above the 9.1-MeV discriminator level so it would not be accumulated in the DMF data but would stimulate the > 9.1 -MeV count rate meters. The response of the count rate meters is a function of the frequency.

GAMMA-RAY PULSES					CUP/SLAR PULSES			X-RAY PULSES		
Cycle No. (DSF)	Pulse Height (Mev)	PHA Channel Data	Count Rate Meter Data	Frequency Hz	Pulse Height To Threshold	Count Rate Meter Data	Frequency (Hz)	Pulse Height (keV)	PHA Channel Data (keV)	Frequency Hz
1	10.10	None	>9.1 Mev	781	Below	No	6,250	16.5	13 to 30	6250
2	0.27	None	None	48	Below	No	781			
3	0.33	6	0.3 to 9.1 Mev	6250	Below	No	100,000	13.5	7.5 to 15	6250
4	1.00	70	0.3 to 9.1 Mev	781	Below	No	6,250			
5	8.19	354	0.3 to 9.1 Mev	48	Below	No	781	13.5	7.5 to 15	6250
6	10.10	None	>9.1 Mev	6250	Above	Yes	100,000			
7	0.27	None	None	781	Above	Yes	6,250	16.5	None (Antico Reject)	6250
8	0.33	None (Antico Reject)	None (Antico Reject)	48	Above	Yes	781			
9	1.00	None (Antico Reject)	None (Antico Reject)	6250	Above	Yes	100,000	13.5	None (Antico Reject)	6250
10	8.19	354	0.3 to 9.1 Mev	781	Below	No	6,250			
11	10.10	None	>9.1 Mev	48	Below	No	781	13.5	7.5 to 15	6250
12	0.27	None	None	6250	Below	No	100,000			

Table IX

Electronic Pulse Calibration Format

ORIGINAL PAGE IS
OF POOR QUALITY

During the third DSF, the 0.33-MeV pulses should be seen in the sixth PHA channel. This PHA count could be calculated from the frequency and PHA live time. The pulses would also be seen in the 0.3-9.1 MeV solar and background count rate meters. During the eighth and ninth DSF, the anticoincidence rejection capability is checked.

The pulse heights of the cup and slab pulses are 10% above or below their discriminator levels. When the pulse heights are above the discriminator level, the responses of the count rate meters are functions of the frequencies. Three frequencies are required here because of the LCRM's. The sequence is selected to optimize efficiency of the calibration cycle relative to anticoincidence rejection.

The x-ray channel is checked at one frequency, since frequency response is not considered a critical parameter here. X-ray energy level testing is performed as indicated for the following reasons. Discrimination of the four energy windows in the x-ray range is accomplished by one set (upper and lower) of discriminators preceded by a variable attenuator. Due to the simplicity of the attenuator circuits it was decided that only the discriminators need to be checked during calibration; this greatly reduces the complexity of the IFC circuitry. The input to the x-ray channel is varied slightly above and below

the 15-keV energy level. These levels would be centered around the upper discriminator level when the prescribed energy window is 7.5-15 keV, since attenuation factor equals 1 (no attenuation) here. When the energy window is stepped to 15-30 keV, these IFC levels are centered around the lower discriminator, since an attenuation factor of 2 is enforced here. Hence no data is expected during the two upper energy windows, since the attenuator divides the IFC levels by a factor of 4 and 8, which corresponds to a factor of 2 and 4 below the lower discriminator level.

The frequency select circuit consists of a modulo 3, which is advanced by the WASC signal. The decoded outputs select the required frequencies from the 1.6-MHz countdown chain. The x-ray level select is also derived from this modulo 3 counter. The main channel level select control is generated by a modulo 5, whose sequence is consistent with the switching requirement in the analog IFC circuitry to produce the necessary level changes. The cup and slab IFC level select is decoded directly from the subframe counter.

3.15 Ground Support Equipment (GSE)

The UNH ground support equipment consisted of the following:

1. A spacecraft simulator to provide the proper timing signals and supply voltages to the instrument. This unit also supplied the commands via front panel push buttons.
2. A monitor to decode the instrument/spacecraft signals into ASC, DSF, and MF data. All data was displayed on NIXIE readouts, and status was decoded on front panel lights. This was a stand-alone unit because the readout could be advanced manually, although this would be a very slow process. In the automatic mode a large portion of the data could be roughly monitored.
3. A Varian 620/i minicomputer to store and printout instrument data. The teletype was used to print data at a rate slower than real time.

The GSE was used at Time-Zero for bench tests of both units 1 and 2. The Varian 620/i was developed into a larger system, which was used to process data of tests at BBRC, quick look data, and the final data.

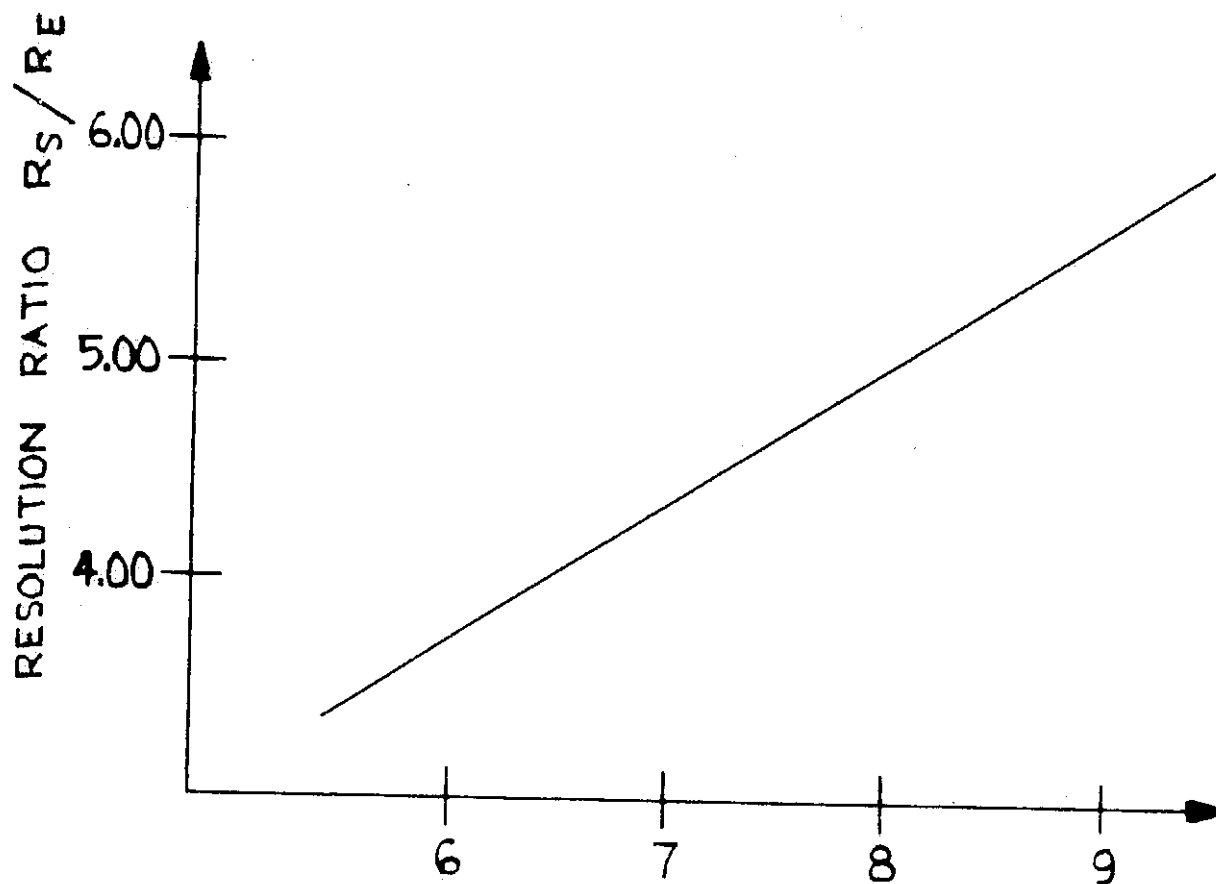
4. Instrument Performance

The following charts, graph, tables, and figures relate the instrument performance to the contract specifications and the informal revisions. In general, these specifications apply to the entire electronics system, exclusive of the detectors. Specific exceptions will be acknowledged as they are discussed.

4.1 Energy Resolution

The instrument design fixed the energy resolution of the electronics to be approximately five times smaller than a typical detector resolution. Naturally, if better detector resolution is provided, the ratio of detector resolution to electronic resolution will be smaller. Therefore, Figure 4.1-1 relates the electronic resolution to the detector resolution in the form of a graph. The numbers used are based on the following physical parameters:

1. Number of channels.
2. Energy range of PHA.
3. Pure quadratic function.



Detector Resolution (% at .662 Me V)

Plotting Info:

Curve = straight line

8% =4.97

6% =3.73

ORIGINAL PAGE IS
OF POOR QUALITY

Figure 4.1-1 Resolution Ratio versus Detector Resolution

4.2 Electronics Duty Cycle

The average full scan duty cycle for data taking is approximately 99.4% (here duty cycle for data taking is defined as live time divided by possible live time). The worst case is when the quadrant generator omits a quadrant because of end of scan. This represents 1 of 90 or 1.1% artificial dead time. On the average this will occur less often than every second scan. In the intermediate scan the average duty cycle drops to 98.3%, and in the short scan, 96.7%. The worst case figure for the short scan is 93.4%.

4.3 Pulse Height Dynamic Range

All detector analog systems were designed for a 30% overrange capability within their linear range of operation. No modes of operations have revealed this number to be inadequate.

4.4 Overall Stability

The temperature data suggests the following stability figures over the -10° to $+30^{\circ}\text{C}$ temperature range:

Main channel gain	$\pm 1.8\%$
X-ray gain	$\pm 2.3\%$
Charged-particle gain	$\pm 1.0\%$
Log count rate meters	$\pm 0.5\%$
Housekeeping readouts (status)	$\pm 2.6\%$
High voltage power supplies	$\pm 0.24\%$

It should be noted that the method for injecting charge into the amplifier system for gain measurement relies on the absolute capacitance of the coupling capacitor. These capacitors, in general, were not NPO types but rather were DUR-MICA types which have a temperature coefficient of (typically) 100 p/m, which can lead to a 0.5% shift.

The projected stability over the expected orbital quiescent range of 6°C is ± 1 channel for data appearing in channel 286 and above. Data at the low end of the PHA could vary as much as four channels. These projections assure that the thermally induced changes in the electronics may be approximated by a linear function, when in fact the variations tend to be concentrated at the extremes of the -10° to $+35^{\circ}\text{C}$ range. Thus one can conclude that the figures mentioned above are worst case estimates.

4.5 PHA Differential Nonlinearity

The quadratic pulse height analyzer was measured for differential nonlinearity using a commercial sliding pulser as a stimulus. The accumulated counts are transferred (via paper tape) to a time-shared computer for final analysis. The analysis program utilizes the linear relationship between channel number (N) and channel width (ΔE).

$$\Delta E = \frac{A^2}{4F^2}(2N+2N_0+1)$$

where A, F, N_0 are various constants defined in Section 3.13. A straight line is fit to the data points and the deviations listed and plotted as shown in Figure 4.5-1 and 4.5-2.

Because of the statistical nature of the analyzed data, sufficient counts must be accumulated in each channel to reduce the statistical uncertainty to below the level of the measurement. The plot (Figure 4.5-3) delineates this time requirement based on the worst case PHA channel (271), the inherent inaccuracies of the test equipment, and the 70% confidence level commonly used.

Average values of DNL at -10°C are listed in the table below. The percentages are measured widths referred to the calculated widths.

CHANNEL NO.	COUNTS	DEVIATION	% DEVIATION	NOTES
340	118692	-702.696	-0.588549	
341	119704	34.1758	2.85584E-2	
342	118791	-1153.95	-0.962068	
343	119951	-269.079	-0.223822	
344	119733	-762.207	-0.632562	
345	121198	427.666	0.354115	
346	119641	-1404.46	-1.16028	
347	120788	-532.59	-0.438994	
348	121120	-475.717	-0.391228	
349	121873	2.15527	1.76849E-3	
350	120677	-1468.97	-1.20264	
351	121997	-424.1	-0.346427	
352	122365	-331.228	-0.269957	
353	123535	563.646	0.458355	
354	122111	-1135.48	-0.92131	
355	123161	-360.609	-0.29194	
356	123057	-739.737	-0.597542	
357	124429	357.135	0.287845	
358	123165	-1181.99	-0.95056	
359	124354	-268.12	-0.215146	
360	124267	-630.247	-0.504612	
361	125770	587.625	0.477442	
362	123928	-1519.5	-1.21127	
363	125621	-101.63	-8.08366E-2	
364	125259	-738.758	-0.586326	
365	126276	3.11523	2.46707E-3	
366	125191	-1357.01	-1.07233	
367	126558	-265.141	-0.209063	
368	126897	-201.268	-0.158356	
369	128203	829.604	0.651317	
370	126429	-1219.52	-0.955375	
371	127663	-260.65	-0.203755	
372	127275	-923.778	-0.720583	
373	128573	99.0947	7.71322E-2	
374	127625	-1124.03	-0.873042	
375	129010	-14.1602	-1.09748E-2	
376	129078	-221.288	-0.171144	
377	122699	-6875.42	-5.30615	**

THE TEST REQUIREMENTS ARE:

CHANNEL NUMBERS	MAXIMUM DEVIATION (%)
1 - 5	50.0
6 - 15	10.0
16 - 90	5.0
91 - 270	2.5
271 - 377	1.25

ORIGINAL PAGE IS
OF POOR QUALITY

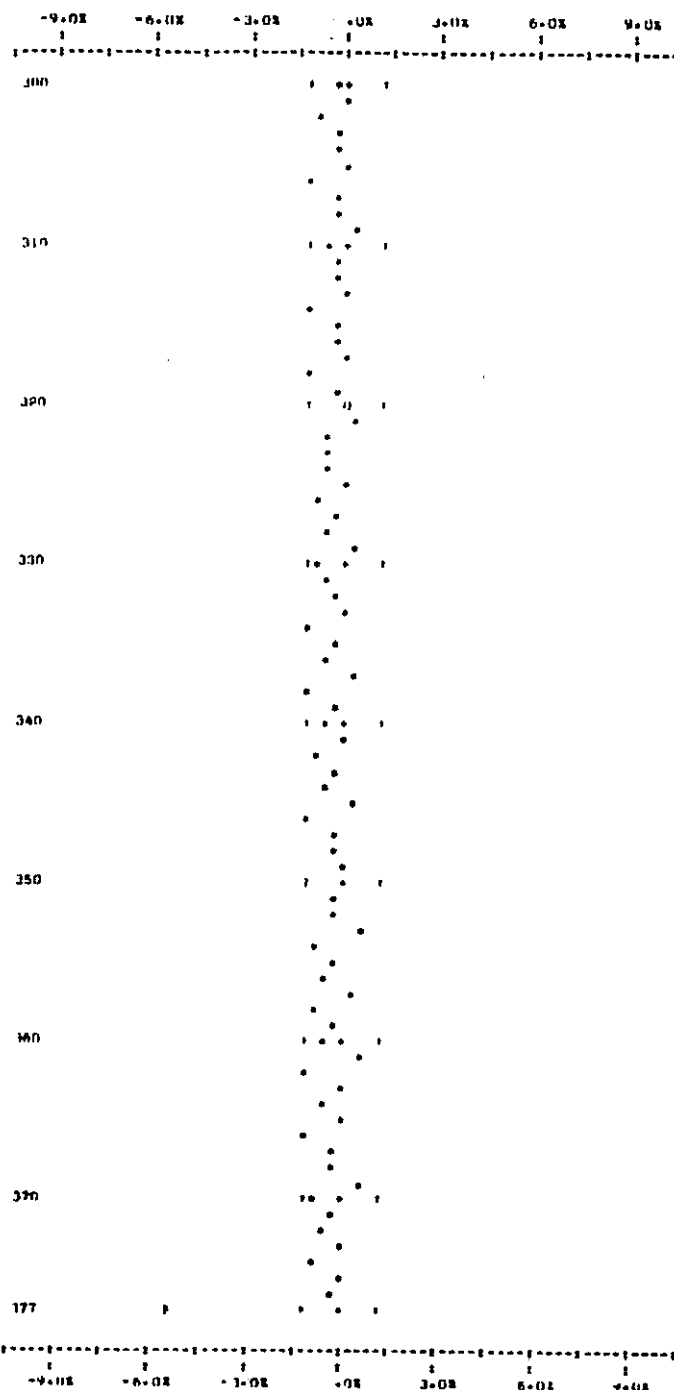
Figure 4.5-1 Differential Nonlinearity Analysis Printout
(for portion of spectrum)

SYMBOL TABLE:

- = ZERO REFERENCE
- † = SPECIFICATION LIMIT OF ACCEPTANCE
- = DATA POINT (IN SPEC.)
- = DATA POINT (OUT OF SPEC.)
- 0 = COINCIDENCE BETWEEN • AND DATA POINT
- † = COINCIDENCE BETWEEN † AND DATA POINT

09/02/71 16:34 L

PHOTO AT -10 C

A PLOT OF CHANNEL 300 TO 377
EACH HORIZONTAL SPACE IS 0.3

ORIGINAL PAGE IS
OF POOR QUALITY

Figure 4.5-2 Differential Nonlinearity Analysis Plot

ORIGINAL PAGE IS
OF POOR QUALITY

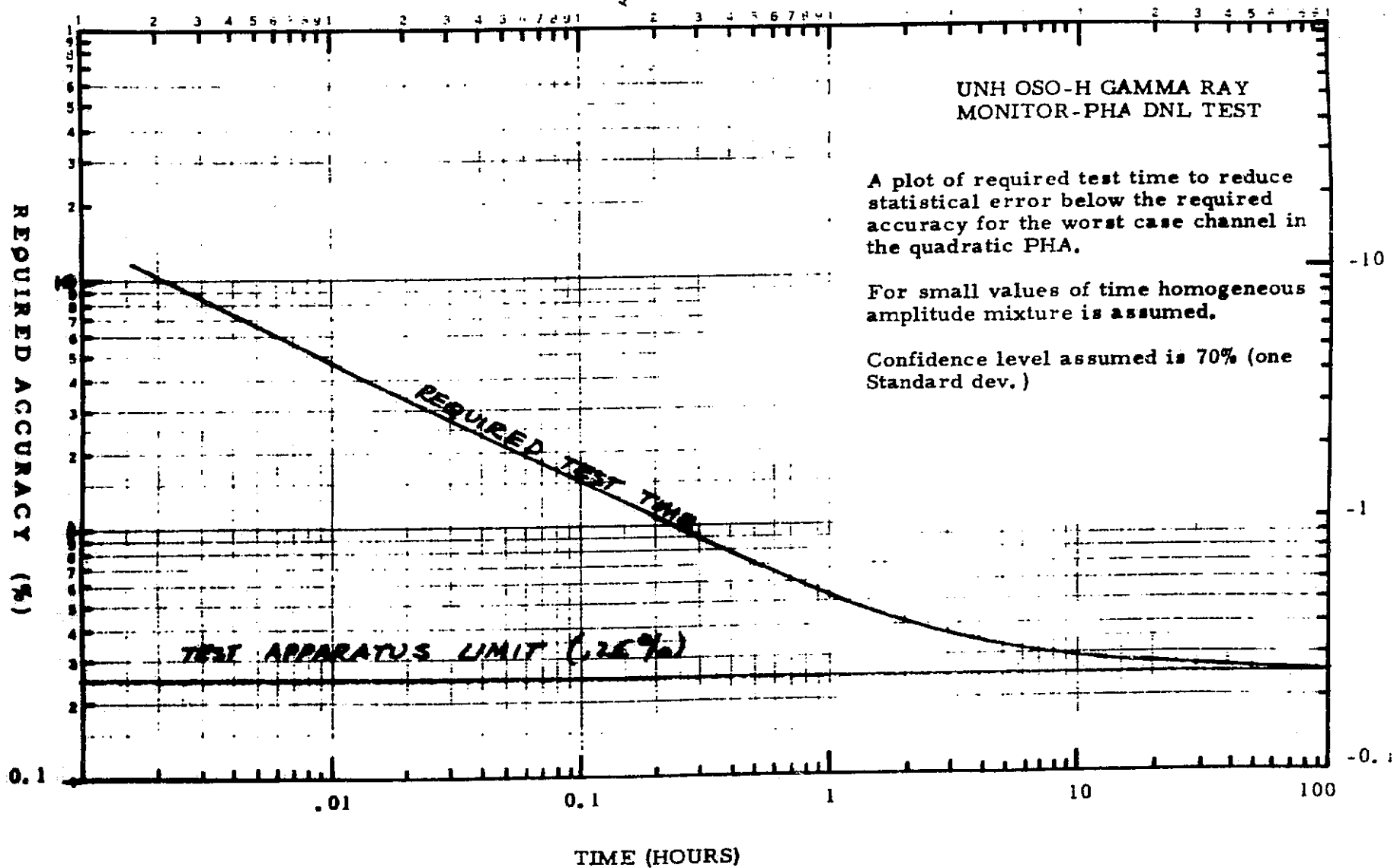


Figure 4.5-3 PHA DNL Test

Channel	Average DNL Value
1-7	100%*
8-15	2.1%
16-90	1.1%
91-270	.79%
271-376**	.45%

*Channels 1-5 are completely dead and
channels 6 and 7 are highly nonlinear.

**Channel 377 was artificially narrowed
by the ULD.

4.6 Maximum PHA Dead Time

The PHA dead time may be expressed as:

$$T_D = NP + T_0$$

where N = channel

P = period of the PHA clock

T_0 = sum of all circuitry delays
and memory cycles

T_0 has been measured to be $20 \mu\text{sec} \pm 0.5 \mu\text{sec}$ on the average (readout requests can alter the memory wait time), while P is accurately fixed by a crystal to be $0.625 \mu\text{sec}$.

$$T_D = (0.625)N + 20$$

For a maximum analyzable event, $T_D = 255.6 \mu\text{sec}$, which is less than the requested $256 \mu\text{sec}$.

4.7 Live Time Accuracy

The 1.6-MHz crystal clock is counted down to 391 Hz (period=2.560 μ sec) for general timing purposes. Therefore, the live time circuitry (which uses this clock frequency) has a time resolution of 2.56 μ sec. However, this clock frequency is prescaled by a factor of 8 for full and intermediate scan and not at all for short scan. Whenever prescalers delete the least significant bits of a measurement, the formula for conversion biases the answers to the middle of the uncertain range. Then errors may be expressed as \pm from some average value. If the uncertain range is N counts wide, the maximum error may be expressed as N/2. For the live time measurements, this value is expressed as a percentage of the total live time for each accumulation mode:

<u>Mode</u>	<u>Maximum Error</u>
Full scan	$\pm 0.011\%$
Intermediate scan	$\pm 0.017\%$
Short scan	$\pm 0.017\%$

These values include the basic digitizing error which results from comparing a continuous function to a discretely incrementing one.

4.8 Quadrant Placement

The quadrant generator relies on a BBRC-supplied signal for sun line placement, but the 5.5° tolerance imposed allows 30.5 μ sec for all circuit delays and signal recognition. The absolute location of the quadrants is accurate to within $\pm 0.23^\circ$ at the nominal spin rate of 30 rpm and repeatable to much less than this.

4.9 Performance Summary

Figure 4.9-1 provides a complete comparison of the instrument to the specifications requested in the UNH sub-contract to Time-Zero Corporation.

Figure 4.9-2 lists the detector parameters.

PARAMETER	DESIGNED/MEASURED VALUE	CONTRACT VALUE	REQUESTED VALUE
Energy Resolution	4.97 for 8% detector	≈ 5	≈ 5
Duty Cycle	99.4%	$> 90\%$	$> 90\%$
Gating Efficiency	Measurement Waived by UNE	$\leq 0.01\%$	$< 0.01\%$
Pulse Height Dynamic Range	$> 130\%$	$\geq 130\%$	$\geq 130\%$
Overall Stability	$\pm 0.24\%$ to $\pm 2.5\%$ (see text)	$\leq 1\%$	$\leq 1\%$
PHA Integral Nonlinearity	Measurement Not Defined	$\leq 0.25\%$	$\leq 0.25\%$
PHA Differential Nonlinearity			
Ch 1-7	100%	$\geq 10\%$	$\leq 50\%$
Ch 8-15	2.1%	$\leq 10\%$	$\leq 10\%$
Ch 16-90	1.1%	$\leq 5\%$	$\leq 5\%$
Ch 91-270	0.79%	$\leq 2.5\%$	$\leq 2.5\%$
Ch 271-377	0.45%	$\leq 1.25\%$	$\leq 1.25\%$
PHA Dead Time	255.6 μ sec	$\leq 256 \mu$ sec	$\leq 256 \mu$ sec
PHA Live Time Accuracy	0.011%	$\leq 0.33\%$	$\leq 0.01\%$
Quadrant	$\pm 0.23^\circ$	$\pm 2.5^\circ$	$\pm 2.5^\circ$

UNH OSO-7 DETECTOR PARAMETERS

CENTRAL DETECTOR

(3" BY 3" NAI)

1. $G_0 = 67 \text{ cm}^2$ (isotropic projected area)
2. Resolution $< 8\%$ at 662 keV
3. Angular Response 120° FWHM at 662 keV
4. Photopeak Sensitivity (R = SF)

<u>E</u>	<u>S (cm²)</u>
0.100 MeV	33
0.500 MeV	17
1.00 MeV	8
4.00 MeV	3

X-RAY DETECTOR

(1 1/4" BY 1/4 NAI)

Area 7.9 cm²

CUP

CsI (NA)

1. External Area $\sim 1.3 \times 10^3 \text{ cm}^2$
2. Mass $\sim 1.3 \times 10^4 \text{ gr}$ (28 lbs)

SLAB

CsI (NA)

1. External Area $\sim 1.7 \times 10^2 \text{ cm}^2$
2. Mass $\sim 4 \times 10^2 \text{ gr}$ (0.9 lbs)

Am²⁴¹ α rate $\sim 1.2 \times 10^3 \text{ Hz}$
 Co⁶⁰ β rate $\sim 1.5 \times 10^3 \text{ Hz}$

SATELLITE ORBITAL PARAMETERS

1. Period 93 minutes
2. Inclination 33 degrees
3. Altitude Excursion $328 \pm 566 \text{ km}$
4. Vertical Cutoff $3.0 \pm 17 \text{ Gv}$
Rigidity

Figure 4.9-2

5. Gamma Ray Response Function

Because of the complexity of the instrument response function, the actual response was measured on the spacecraft after it was fully loaded and spinning on a test stand (Higbie et al., 1972). The response test was carried out at BBRC using the following radioactive sources and gamma energies:

Sn¹¹³ - 0.392 MeV
Cs¹³⁷ - 0.662 MeV
Zn⁶⁵ - 0.511 and 1.115 MeV
Na²⁴ - 1.368 and 2.75 MeV

Five 7-track magnetic tapes made at BBRC and containing the calibration data were merged into a single 9-track tape at the UNH Computation Center. Datasets on this tape were compared with the log book records and erroneous records were corrected, then separated into solar and background records, each preceded by a proper header card.

Since the gain of the system changed by about 7% during the calibration period, gamma ray lines 1.460 MeV (K⁴⁰) and 2.615 MeV (Tl²⁰⁸) observed in the background spectra were used to determine gain as a function of time over the 5-day period. Background data averaged over 10-minute intervals distributed throughout the calibration period was used to determine offset

(N_0) and gain (C) values for the instrument transfer function. The value for N_0 averaged over the entire calibration period was then used to determine C for individual graphs; linear interpolation was used to find C for intermediate times. After determining C for each dataset, the spectra were smoothed and then gain corrected to a standard C ($= 0.444 \times 10^{-5}$) in the manner described by Higbie et al., 1972.

Datasets with the same elevation (θ) and azimuth (ϕ) angles were added together and average spectra for each set of θ and ϕ determined.

The runs with the shadow cone in were then subtracted from the corresponding spectra with the shadow cone out. This provided a rough correction for the effect of scattering and room background correction for Sn^{113} , Cs^{137} , and Zn^{65} sources.

Na^{24} spectra were treated differently from the other three sources. In the case of Na^{24} spectra, room background was first subtracted from the source spectra. This had to be done because of the short (15 hours) half-life of Na^{24} .

6. Postlaunch Operation

The OSO-7 gamma ray detector in orbit operated as expected except the gain fluctuations were much greater than expected. The low voltage power supply was kept on for the life of the instrument with the exception of initial turnon and several days in November 1972.

The instrument main channel was observed to undergo an unexpectedly large drop in gain shortly after turnon in orbit, which was attributed to a problem with the photomultiplier. The instrument high voltages were turned off to allow the PMT to recover but subsequent turnon indicated a lasting gain drop with very slow recovery. It was expected that the PMT might undergo a gradual drop in gain due to aging; the high voltage supply was built with a programmable output allowing for an overall gain compensation by approximately a factor of 3. We were, therefore, able to set the detector back up to the normal operating point. Since the PMT was a last minute replacement in our flight unit with a new nonlinear bleeder chain, it is not possible, from the behavior of this tube, to isolate the cause of the aging difficulty. Some possible causes might be:

1. Inadequate aging.

2. Abnormal aging due to the use of the nonlinear voltage divider on the dynodes.

3. More than usual fatigue effects due to the high gain PMT used.

4. Current limit of HV supply set too high. (See Section 3.5.2 for description of central detector power supply.)

The changes in gain with passage through the trapped radiation regions considerably changed our operations from what we expected, in that we were forced to turn the high voltages off during the worst orbits to avoid further gain loss. As time went on we were able to increase our operating time by more accurate prediction of the bad orbits, and during periods of favorable apogee we could even leave the instrument on full time. The on time was also increased when high solar activity was predicted and decreased during periods of low activity.

For an average of about one orbit per day, the instrument was operated in the alternate quadrant mode, again during periods of low solar activity.

The short and medium scan modes were never used because of the gain instability.

The commands for the instrument originated at UNH and were called in to the OSO operations control center at GSFC. Normally the daily commands consisted of HV on/off (to avoid the problems of the trapped charged-particle regions). The HV step and gain mode commands were used to adjust the gain mainly to make up for our initial gain loss.

6.1 Quick Look System

The quick look (Q/L) system consisted of a direct data link (2400 bps) to the OSO-OCC at GSFC and the Varian 620/i at UNH. Data for several orbits each day was transmitted to UNH shortly after playback to enable UNH to make decisions about the operation of the instrument and to issue appropriate commands.

Quick look data at UNH was recorded on 7-track tape for subsequent playback and analysis, and calibration spectrums were displayed on an X-Y scope as the data was being received. When data was not being received, other programs could be run on the Varian 620/i to display the data on the 7-track tapes.

6.2 Failure

At 2315 UT (universal time) on December 25, 1972, the UNH instrument failed, and several attempts to restart it by cycling power on/off were not successful. Data became locked up in all channels so that not even housekeeping data was available. Spacecraft wheel current increased just before the data locked up and subsequent tries at turning on indicated excessive current draw.

The UNH data indicates that the problem was probably in the low voltage supply, possible a short in one of the output lines.

Main channel data indicated that the main channel high voltage was constant; the Co^{60} calibration source leakage peaks were steady, with a normal drop during a belt pass, and subsequent upward recovery. The x-ray and shield high voltage cannot be determined from the data.

Both high voltage readouts indicated a rise in high voltage, but since the MC voltage did not rise, it is probable that the readouts were in error. Both readouts returned to the -12 volt line and would both rise if this line rose. A plot of the readout values versus the -12 volts indicated that this was probably the case (Figure 6.2-1).

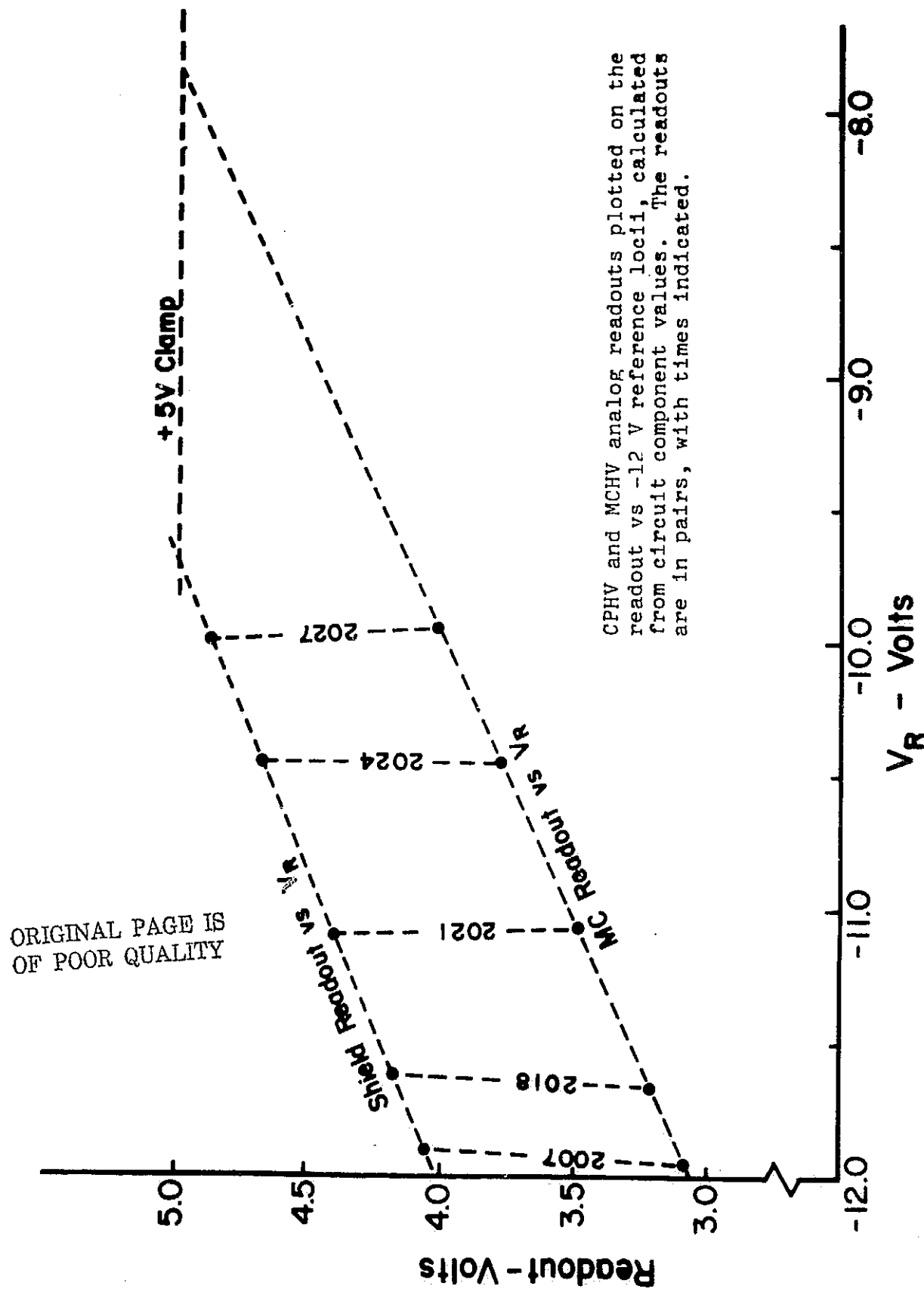


Figure 6.2-1

Prior to failure counts in the lowest channel of main channel data increased. Normally the first ten channels have no counts because of a low end peak detector threshold, and an increase in the first channel counts indicated that the analyzer was turned on when no signal was present. This could be due to a change in threshold level or noise triggering the threshold. A similar increase was seen in the lowest x-ray channel. The x-ray used the same threshold detector for channels 1 and 3, so a change in threshold would show up in both channels. However, the lowest x-ray channel was closer to tube noise. Change in threshold levels downward could be caused by a downward drift of the 6-volt supply. Noise on the supply lines could be caused by an overload.

The temperature sensors indicated an increase in the temperature difference between the detector and blivet 2 (digital) with detector temperature falling and electronics temperature increasing. This could be due to increased power dissipation in blivet 2. Both thermistors were tied to the 5-volt line, indicating that the dc level on this line was fairly steady.

Analog status lines (word 1) dropped by about 4% prior to lockup. These readouts were derived from the digital 5-volt line. The 20-volt readout also dropped by about 3%.

The HV reference (ramp) readout did not change. This is derived from the regulated 5-volt line.

Indications are that at least the -12, 5, and 20 volt lines changed toward zero. The 6-volt line might have changed, producing lowered threshold levels. Possibly an overload on one of the low voltage lines produced excessive currents, which could generate noise and cause voltages to drop. Whatever the fault was, it was permanent. Later turnons produced the fault within minutes. The instrument locked up in ASC word 1; in main frame word 1; and in the digital subframe (x-ray), in preferred bit patterns.

The analog interface appeared to be working, as well as some portion of the DSF readout. Beyond that there is no usable data.

Based on the above information, we concluded that an overload developed on the -12 volt line causing it to move to about -8 volts or higher. This caused excessive current draw in the low voltage converter, possibly causing noise on other lines and eventually a slight decrease in other lines. It is not clear if the -12 volt overload was to ground or to some positive voltage. The fault did not clear when power was shut off.

7. Data Processing

7.1 Quick Look Data Processing

The quick look data processing has a twofold purpose:

1. To provide a means of near real time monitoring of the instrument.
2. To provide data for preliminary analysis.

Our Q/L programming was not ready until several weeks after launch so the initial operation of our instrument was done from GSFC. Once we established our Q/L system, we were able to receive, via modem, spacecraft playback data as it came into GSFC. Typically we would receive five playbacks each day and could look at the calibration data as it came in to verify that the gain was correct and the instrument was operating properly. To print out housekeeping and x-ray data, other programs had to be loaded; this could only be done at times when we were not receiving data.

Because of our gain problems, it was necessary to monitor the instrument as much as possible near the beginning of the instrument life in orbit. As our knowledge increased, we

eventually went to block data transmissions daily, then weekly. This allowed more computer time for software development and data analysis.

All quick look data processing was done on the Varian 620/i.

Data for preliminary analysis was hard to obtain at first because of the slow speed at which the teletype printed out. With the addition of a medium speed printer, considerably more data could be printed out.

Quick look data printouts displayed main channel data, ASC (housekeeping data), and x-ray data. The formats were basically dumps of raw data. Because the Q/L was considered temporary and we were limited in our programming capabilities, no real attempt was made to implement the Q/L system as a real tool for operating and maintaining the instrument. However, experience with the Q/L data was useful in the development of programs for the final data analysis.

As the experimenter data tapes came in from GSFC, the Q/L data was replaced by PASS1 data (see Section 7.2.1).

7.2 Final Data Processing

The final data processing was done in part on an IBM 360/50 and in part on a Varian 620/i. The IBM 360 was used to process the GSFC-supplied experimenter data into raw experiment data (including ASC and x-ray) and gain-corrected main frame data (including various orbital parameters).

The first output (PASS1) produced data for the gain correction program (PASS3) as well as optional outputs of engineering plots (rates, etc.), and one-line summary (status, live time, etc.) for each scan.

The PASS1 and PASS3 data is output to 7-track tapes, which can be processed on the Varian 620/i. The Varian programs mainly consist of data-handling subroutines; such as read, display, sum, time select, parameter select, and others; which can be used in a flexible manner.

The sequence of analysis is:

1. Run PASS1 on IBM 360 (see Section 7.2.1).

2. Generate calibration data using CAL1 (see Section 7.2.2); select epoch times so that the instrument gain will fit to a smooth function. The data is graded as quality 1, 2, and 3, depending on how closely the gain function will fit the actual calibration points. Quality 1 indicates good fit ($\pm 1\%$), quality 2 is questionable ($\pm 2\%$), and quality 3 is definitely not a fit.

3. Generate the gain functions for the various epoch times using CAL2 (Section 7.2.3). The fit is checked, and if not correct, the epoch times are reworked, and CAL2 is run again.

4. Run PASS3 (Section 7.2.4) using the CAL2 gain functions to normalize gain. Data is tagged according to quality.

The VAPREDICT program (Section 7.2.5) is a stand-alone program used to generate values of maximum rates and counts encountered in radiation belt passes. This data was used to operate the instrument (HV on/off) and to help evaluate the CAL1 output.

7.2.1 PASS1

There are six possible options of this pass. The options can be executed in any combination depending on the parameters specified on the control card. The options are as follows:

1. Engineering plot
2. Line summary
3. Calibration cards
4. X-ray tape
5. Good time cards
6. Main frame data tape

The engineering plots are constructed for the various log rate meters which monitor the counting rates of the scintillators comprising the instrument. Temperature, voltages, and status are also monitored. The output of the program is stored on a Memorex-3660 disk and then 7-track plot tapes are created in a second job step. The plots contain status information and housekeeping information rates for the central detector, cup, and slab.

Each line in the one-line summary represents information for three minutes of satellite data. This corresponds to the accumulation of a complete gamma ray spectrum. Time, rates, status, sync errors, and warnings are printed.

The calibration data consists of the central channels of the three gamma peaks in the calibration spectrum interpolated from a quadratic least squares fit to each peak. The total counts in each peak and the midpoint of the time interval during which the calibration was accumulated are also included.

The x-ray data is obtained from the experimenter tapes with detailed spin and timing information to allow exact time correlations of the x-ray data with solar activity indices from other experiments. This data is stored on a 9-track tape which is Fortran compatible and may be used on the IBM 360/50. A 7-track reformatted version is also generated for use on a Varian 620/i.

The good time cards consist of begin and end midpoint of the accumulation times for good continuous data. Only data collected when the central detector was on and with no time gaps is considered good. These cards are later used as input to PASS3.

Main frame data for each quadrant scan collected when power was on is written onto a 9-track tape along with analog data and readout time. The tape is then converted to 7-track for use on the Varian 620/i with Tektronix-4010 display unit interface.

7.2.2 CAL1

This program reads a series of input cards, the first of which contains the N_0 to be used in the calculation of the gain constant (for our purposes, a constant N_0 of 80.2 was used). The other input cards are calibration cards generated by PASS1. Each card contains midpoint of accumulation time, three peak channels, and three peak counts. From this information CAL1 calculated an N_0 for each input card from the relation:

$$N_0 = \frac{\sqrt{E_1} n_2 - \sqrt{E_2} n_1}{\sqrt{E_2} - \sqrt{E_1}}$$

An average N_0 is then calculated for all the cards read.

The program then calculates a gain constant for each card using weighted average:

$$C = \sum_i w_i \frac{E_i}{(n_i + N_0)}$$

where

$$E_1 = 1.17323 \text{ MeV}$$

$$E_2 = 1.33248 \text{ MeV}$$

$$E_3 = 2.525 \text{ MeV}$$

$$w_i = \frac{N_i}{N_1 + N_2 + N_3}$$

N_i = number of counts under the peak at energy E_i

n_i = the channel that corresponds to the energy E_i

An error statistic is calculated for each calibration in the following way:

$$i = 1, 3$$

$$ER_i = [E_i - C(n_i + N_0)^2] / E_i$$

$$ERROR = \sqrt{\sum_{i=1,3} (ER_i)^2}$$

A magnetic tape record is generated for each calibration card and contains time at midpoint of accumulation, C, and N_0 . The program then prints a listing of all the cards read; time, Co⁶⁰ channels, counts, N_0 , C, and the error indicator.

This listing is reviewed by our project engineer and epoch times are derived from this source in conjunction with the output from the Van Allen Predict program (see Section 7.2.5).

7.2.3

CAL2

This program reads in deletion cards, epoch time cards, and the output tape from CAL1. The deletion cards contain the times of tape records to be ignored and a 1 in column 80. The epoch time cards contain the epoch times, the quality indicator, and a 2 in column 80. The quality indicator is a number from 1 to 3, 1 being good quality and 3 being poor quality. This indicator is carried over on the PASS3 tape to all spectra falling within the range of this epoch. The calibration input tape records generated by CAL1 contain midpoint of accumulation time, C, and N_0 (80.2). The deletions must always precede the epoch cards, both being in chronological order. The epoch time cards and the tape records merge so that a certain number of calibrations correspond to each epoch time.

CAL2 fits a gain function to data of a given epoch, T, in the form:

$$C(t) = q + r(t-T) + s(t-T)^2$$

Let N be the number of calibrations for one epoch.

$$\begin{aligned} \text{For } N = 1 \quad r &= s = 0 \\ q &= c_1 \end{aligned}$$

$$\begin{aligned} \text{For } N = 2 \quad s &= 0 \\ c_1 &= q + r(t_1 - T) \\ c_2 &= q + r(t_2 - T) \\ r &= \frac{c_2 - c_1}{t_2 - t_1} \\ q &= c_1 - (c_2 - c_1) \left(\frac{t_1 - t}{t_2 - t_1} \right) \end{aligned}$$

For $N = 3$ using linear least squares fit:

$$\Delta = \sum_i (C - C_i)^2 \text{ with } s = 0$$

$$\frac{\partial \Delta}{\partial q} = \frac{\partial \Delta}{\partial r} = 0$$

$$\Delta = \sum (q + r \Delta t_i - C_i)^2 \text{ where } \Delta t_i = t_i - T$$

7.2.4 PASS3

PASS3 reads in as input a control card, Van Allen cards, good time cards, calibration cards, and the experimenter data tape.

The control card contains the parameters needed for the initial call to FEEDER (read experimenter tape).

The Van Allen cards contain the Van Allen data accumulated in the previous PASS3 production run in the form of calendar time, peak flux, and integrated flux. Each time a new file of data is read, the Van Allen data values are calculated from the orbit data records found at the beginning of the file. If no Van Allen cards are entered, the program initializes the Van Allen data array to zeroes and begins accumulating VA (Van Allen) data from the first file read on tape 1 of this run.

The good time cards (generated by PASS1) contain the beginning and end times of good complete scans of data (solar or background or both). This is data in which the sync word was present, in which there was no data missing (no time gaps), and which was accumulated when the central detector was on.

The calibration cards (generated by CAL2) contain the epoch time, data quality indicator, and q, r, s , and N_c used to gain correct the spectra.

PASS3 stores the values from each of these cards in arrays; the calendar times are converted to seconds of century. The first good time is then read and the experimenter tape is searched until the corresponding time to the nearest second is found. Processing begins at background or solar quadrant depending on what is specified in the good time card (BO or SO). PASS3 processes six major frames at a time (equivalent to one solar quadrant or one background quadrant) until the first end time is reached. Processing stops at background or solar depending on what is requested in the good time card (BK or BO). PASS3 then reads the next begin time and continues processing in the same manner as just described until the last end time is reached.

For each quadrant accepted as good data, orbit and attitudinal parameters are calculated and the gamma spectrum is gain shifted. The status word is realigned with the data spectrum and interpreted. Various flags are set to indicate the condition of the data processed, e.g. the presence of bit errors.

The output of PASS3 is a tape containing the parameters, calculated angles, gain-shifted spectrum, interpreted status, and flags for each half-scan or six major frames processed. This tape has a record length and block size of 3540 bytes.

A short listing is produced by PASS3 containing a printout of the first good time serial numbers, the decomm run numbers, the run date, and various warnings when unusual problems occur.

7.2.5 VAPREDICT Program

This program is a stand-alone program which computes certain parameters for the satellite's passage through the Van Allen Belt. The basic subroutines called are HEIGHT and VABELT which are also used in the primary data analysis.

The dataset is prepared from data supplied by NASA (E. G. Stassinopolous) in a preparatory step and stored on disk. Normal operational use requires an ephemeris data tape supplied by NASA (J. B. Joyce) and the dataset stored on disk.

The predict program computes for a given period of time the peak flux encountered, the time of the peak flux, the integral flux during the orbit, the times where the satellite encountered and then left regions with fluxes $> 10^3$ protons/cm²sec with the corresponding positional information.

Estimated uncertainties are less than one minute for the orbital elements, three weeks from epoch. At the three-sigma confidence level the VA data is off by a factor of 2 in the worst case.

8. Initial Scientific Results

8.1 Assessment of Detector Operation

Before it was possible to utilize the data obtained from the instrument, a considerable effort was carried out to determine that the instrument was operating properly and that any apparent scientific results would be valid. This initial effort was used to design the computerized data analysis scheme (see Section 7).

This effort included checks on instrument parameters that were tested before launch; such as, the central detector's differential and integral linearity, live time checks, energy threshold variation, and correct data sequencing. It also included checks for phenomena that could not be measured before launch since they were strongly influenced by the postlaunch environment. These phenomena included both short- and long-term gain stability and the background spectral intensity and variation. A full description of these tests is given in the "Users' Guide" for this instrument, prepared and submitted to the National Space Science Data Center, and will not be repeated here. However, it is sufficient to say that both qualitatively and quantitatively the instrument operated as expected with two exceptions. These exceptions follow:

1. Greater than expected gain sensitivity to the trapped radiation belts.

2. Greater than expected shield counting rate and central detector spectral features (apparently caused by local production of gamma ray radiation in the spacecraft and detector material).

Neither of these effects caused a serious loss of the instrument's scientific data gathering ability.

8.2 Review of Solar Gamma Ray and Neutron Measurements

The experimental investigations to detect solar neutrons and gamma rays, which were reported in literature by 1970, were reviewed previously by Chupp, 1971. Up to that time there was no conclusive evidence for the existence of either solar neutron or gamma ray fluxes. On the other hand, there were at least three highly disputed claims of observations of both solar neutrons and gamma rays all in times of modest or low solar activity. None of these "possible" events occurred in coincidence with the optical phase of any flare. Nonetheless, since they are published as positive fluxes, we should keep the reports and the conditions of solar activity under which they were observed in mind. The Tata result of Apparao et al., 1966, was obtained under very quiet solar conditions; that of Daniel et al., 1967, was made several hours before a subflare. This result was seriously questioned by Holt, 1967, since no neutron decay protons were seen by the OGO-A satellite, which was in orbit at the time. The OGO-A should have seen them if the neutron flux was 10^{-1} neutrons $\text{cm}^{-2}\text{sec}^{-1}$ as reported. This criticism has now been countered by Daniel et al., 1971, who have revised their result downward nearly an order of magnitude to 1.5×10^{-2} neutrons $\text{cm}^{-2}\text{sec}^{-1}$ based on a new measurement of the atmospheric neutron flux which allowed them to convert the measured solar neutron counting rates to an

absolute flux. It seems this result will not go away. In the case of gamma rays, Kondo and Nagase, 1969, reported an extremely large (800%) increase in the gamma ray flux (3-10 MeV) 10 minutes after a 1N flare and associated radio burst. The last positive report of a gamma ray increase was given by Hirasima et al., 1970, who reported a gamma ray line flux coincident with a 1000-MHz radio burst. As satellite experiments in the future continue to search for gamma ray and neutron events, it will be interesting to see if any enhancements are found under similar activity conditions as in the cases just discussed. Then we can decide if indeed these peculiar observations are most probably positive or spurious.

Several significant experiments summarized in Table X have been discussed in literature since the review mentioned above. Joseph, 1970, has reported the results of measurements at Tata using a new type of high energy detector and a plastic scintillator. The basic neutron detecting element for the new detector consists of a CsI(Tl) crystal slab of 4 3/8-inch diameter by 0.5-cm thick and associated photomultiplier in a 1-cm thick plastic scintillator anticoincidence shield. Fast neutrons, $10 \text{ MeV} < E_n < 500 \text{ MeV}$, produce nuclear reactions, primarily stars, giving rise to proton, alpha particle, or other ion pulses in the slab. Pulse shape discrimination has also been used to separate out neutron-induced star events

Table X

Summary of the recent Solar Neutron and Gamma Ray Observations to August 1972
(For observations before 1970, see Chupp 1971)

Reference	Instrument	Radiation and Energy Range	Neutron or Gamma Ray Flux ($\text{cm}^{-2}\text{sec}^{-1}$)	
			Continuous	Flare Associated
Joseph thesis (1970)	Plastic Scintillator Telescope with antishield	n 15-150 MeV γ 5-30 MeV		2B, 1N 2-26-69 n $< 1.2 \times 10^{-2}$ γ $< 10^{-2}$
Cortellessa et al. (1971)	Plastic Scintillator with antishield	n 10-200 MeV	$< 5.5 \times 10^{-3}$	1N 6-30-70 Protons $< 6 \times 10^{32}$ above P0=60 MV 30 MeV
Eyles et al. (1972)	Scintillator Recoil Telescope with antishield	(i) n 50-350 MeV γ > 80 MeV (ii) Test of Elliot Model	n $< 3 \times 10^{-3}$ γ $< 4 \times 10^{-4}$	(i) 1B 5-29-69 n $< 23 \text{ cm}^{-2}$ γ $< 6 \text{ cm}^{-2}$ (ii) 2B 3-21-65 n $< 4.2 \times 10^{-3}$ Theo. $\sim 5 \times 10^{-2}$ for Class 4
Sood (1972)	Cerenkov pair Telescope with Pb converter	γ > 20 MeV		1N 10-17-68 γ $< 2.6 \times 10^{-4}$ (10 min rise) $< 1.1 \times 10^{-5}$ (active disc)
Lockwood et al. (1972) OGO-6	He ³ proportional counter with antishield	n 1-20 MeV	$< 1.8 \times 10^{-3}$	Null Results
Leavitt et al. (1972) OSO-6	Scintillator Recoil Telescope	n > 40 MeV	$< 4 \times 10^{-4}$	Null Results

ORIGINAL PAGE IS
OF POOR QUALITY

from gamma ray events which produce energetic electrons in the crystal. The sensitivity (area x efficiency) of this detector for fast neutrons is $\sim 0.75 \text{ cm}^2$ above 10 MeV. In addition, the detector is sensitive to gamma rays in the energy range 4-30 MeV, but no estimate is given for the efficiency. The properties of the scintillator block were very similar to those previously discussed by Forrest and Chupp, 1969. The basic properties of the detector needed in this discussion are the sensitivities for solar neutron and gamma rays, which are 22 cm^2 for neutrons ($> 10 \text{ MeV}$) and 30 cm^2 for gamma rays (5-30 MeV). These instruments have been flown in 1969 from Hyderabad ($\lambda_{\text{gm}} = 8^\circ \text{N}$) during coincidental solar activity. During a 2B (and following 1N) flare on February 26, 1969, the plastic block detector observed no increase; therefore, limiting fluxes for solar neutrons were $\leq 10^{-2} \text{ cm}^{-2} \text{ sec}^{-1}$ (5-30 MeV). On April 19, 1969, the smaller volume CsI(Tl) star detector was flown during a 1B flare with no enhancement observed. The corresponding upper limit for solar neutrons in this event was $1.5 \times 10^{-2} \text{ cm}^{-2} \text{ sec}^{-1}$ which is essentially the same as for the larger plastic block detector. The reason for this is: Even though the sensitivity of star detector is much lower than for the former, its background counting rate is correspondingly much lower. All of these limit estimates apply to the case of an assumed neutron spectrum produced by a solar proton exponential rigidity spectrum with $P_0 = 60 \text{ MV}$ (Lingenfelter and Ramaty, 1967).

Cortellessa et al., 1971, have carried out several careful measurements using an anticoincidence shielded plastic scintillator in 1970, which studied both continuous emission possibilities as well as in small flares. The detector was sensitive both to neutrons and gamma rays with the biases for neutrons set at equivalent proton recoil energies of 10, 20, and 30 MeV. Self-gating effects due to recoil protons from the surface of the inner detector interacting in the antishield were reduced by surrounding the inner detector with 1 cm of aluminum. The effective neutron energy range of the detector then was 10-200 MeV, with an efficiency for solar neutrons of $\sim 11\%$ based on an assumed solar neutron production spectrum due to a solar proton spectrum with characteristic rigidity $P_0 = 60$ MV. The continuous solar neutron flux limit was 5.5×10^{-3} neutrons $\text{cm}^{-2}\text{sec}^{-1}$, in the energy range of the detector, for flights in 1970. In addition, failure to detect any neutrons in a flight during a 1N flare on June 30, 1970, gave a limit for accelerated protons at the sun of $< 6 \times 10^{32}$ protons with energies > 30 MeV, for $P_0 = 60$ MV. In order for these workers to achieve the improved limits (shown in Figure 8.1-1), care had to be taken to keep instrumental instability effects on the counting rate B , to less than $2 (BT)^{-1/2} \times 100$ for an observing time T . In this case the instability effects were reduced to 0.28%.

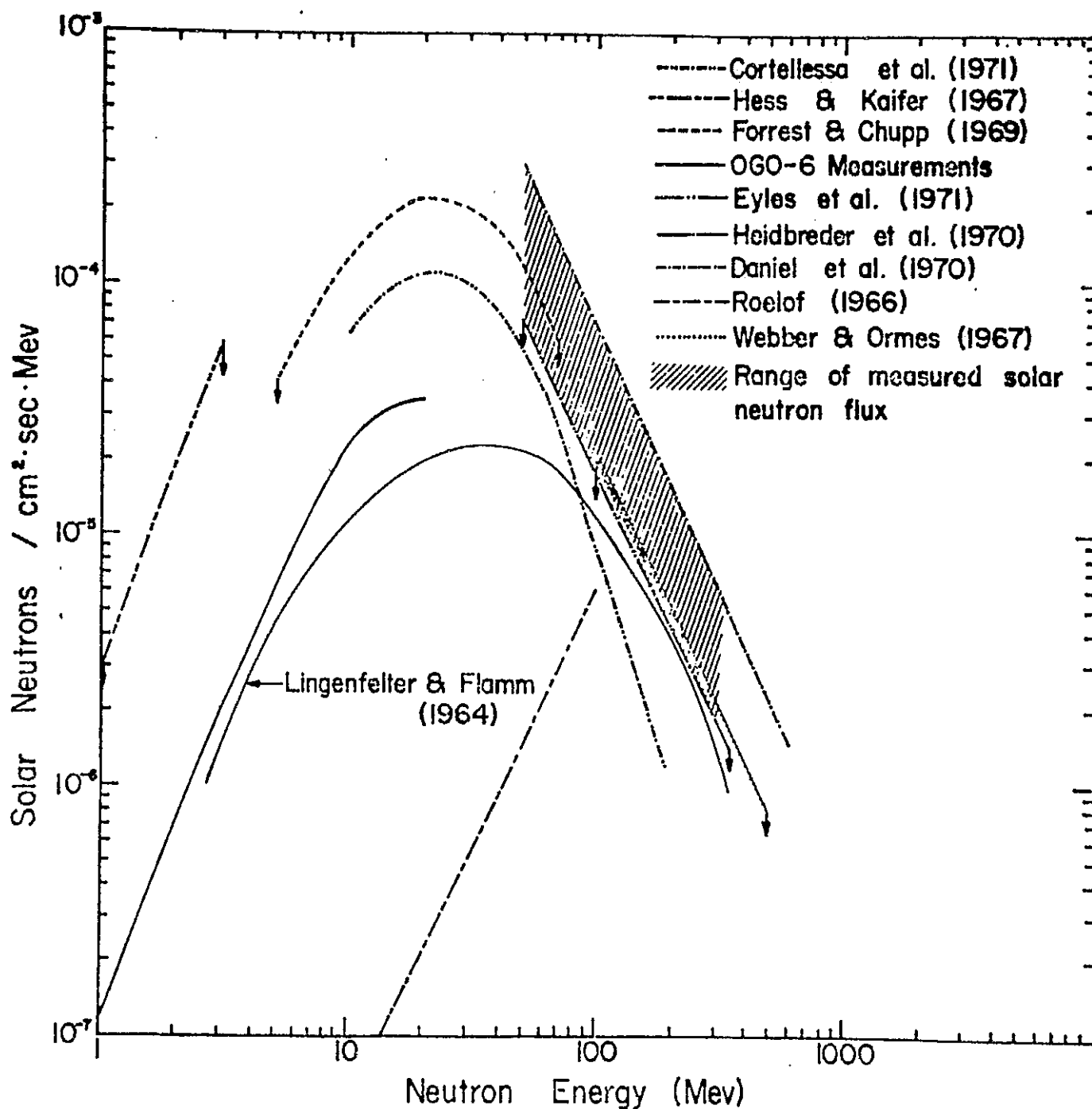


Figure 8.1-1

Summary of the upper limits to the differential solar neutron flux at the earth.

Eyles et al., 1972, have reported on the results of balloon flights with a recoil telescope designed to test the predictions of Elliot, 1969, concerning acceleration of charged particles before the optical flare with consequent release into the solar atmosphere thus providing the energy source for the optical flare. The apparatus consists of a polyethylene block of thickness 16.5 gm/cm^2 as a converter, followed by a recoil proton telescope, all in an anticoincidence shield comprising the neutron telescope. This unit was followed by a Cerenkov element 1-cm thick to eliminate 95% of relativistic charged particles. The detector's neutron response was effective over an energy range from 50-350 MeV with a maximum efficiency at $\sim 190 \text{ MeV}$ of $\sim 1.4\%$, falling steeply on both sides of the maximum. Using the converter area of $\sim 181 \text{ cm}^2$ gives a maximum sensitivity of $\sim 2.5 \text{ cm}^2$. The telescope half-angle for neutrons was $\sim 22^\circ$. The detector was also sensitive to gamma rays with energies about 20 MeV. At 100 MeV the gamma ray efficiency was 35%. This detector was flown in 1969 to give limits both during active periods and quiet periods. The neutron and gamma ray limits for continuous emission are $3 \times 10^{-3} \text{ cm}^{-2} \text{ sec}^{-1}$ (50-350 MeV) and $4 \times 10^{-3} \text{ cm}^{-2} \text{ sec}^{-1}$ ($\sim 20 \text{ MeV}$), respectively. This neutron limit is even lower than that mentioned above by Cortellessa et al., 1971. Even though the sensitivity is an order of magnitude lower for the telescope, the background is much lower. During a 1B flare on November 1, 1969, the limiting neutron and gamma ray fluxes

found were $\leq 4 \times 10^{-2} \text{cm}^{-2} \text{sec}^{-1}$ and $\leq 10^{-2} \text{cm}^{-2} \text{sec}^{-1}$, respectively. There was, however, an opportunity to test to some extent the predictions of Elliot's model (Elliot, 1969) four hours before a 2B flare on March 21, 1969. No neutron flux was detected above a limit of 4×10^{-3} neutrons $\text{cm}^{-2} \text{sec}^{-1}$. Since Elliot's model predicts a flux of $\sim 5 \times 10^{-2}$ neutrons $\text{cm}^{-2} \text{sec}^{-1}$ for a class 4 flare, the authors do not consider this example as a real test of the preflare acceleration model since even much lower fluxes are expected for smaller optical class flares.

Sood, 1972, has also conducted a search for high energy gamma rays from the sun in order to test the Elliot model (Elliot, 1969). His instrument consisted of a pair telescope with a Pb converter. In addition, unidirectional Cerenkov elements were used to detect the relativistic electrons. The instrument was not sensitive to photons with energies < 20 MeV but had an overall efficiency for π^0 gamma rays of $\sim 38\%$ and the area solid angle factor was $22 \text{ cm}^2 \text{sr}$. Several flights were carried out in 1967 and 1968 from Kampala, Uganda, while the sun was moderately active. For a generally active solar disk, the limiting flux was $\leq 1.1 \times 10^{-4}$ gammas $\text{cm}^{-2} \text{sec}^{-1}$ (> 50 MeV), and for a 1N flare on October 19, 1968, the limiting flux was 2.6×10^{-4} gammas $\text{cm}^{-2} \text{sec}^{-1}$ assuming a 10-minute burst. One flight took place ~ 8 hours before a 2B flare on October 31,

1968, but since no 350-MeV protons (π^0 threshold) were observed in space following this flare, the author does not consider this a definite test of the Elliot model. In any case, if one did, the limiting flux would be 1.1×10^{-4} gammas $\text{cm}^{-2}\text{sec}^{-1}$.

In 1969 the OGO-6 satellite carried out neutron monitoring measurements in the energy range 1-20 MeV from June 1969 to December 1969 (Lockwood et al., 1972). The detector was a high pressure He-proportional counter in a plastic scintillator moderator to thermalize the fast (MeV) neutrons. The anti-coincidence charged-particle shield consisted of 22 proportional counters. Typical sensitivities for solar neutron spectra with characteristic rigidities $P_0 = 60$ MV and 125 MV are 0.38 cm^2 and 0.37 cm^2 , respectively. By carefully selecting the lowest background data (primarily low latitude) and using only data in a 6-months' period when no solar proton events were evident, a quiet time limit of 1.8×10^{-3} neutrons $\text{cm}^{-2}\text{sec}^{-1}$ was obtained. This result is about an order of magnitude lower than previously available in the same energy range. In addition, several small flares occurred during the experiment's lifetime, but no positive evidence for enhanced neutron fluxes was seen. No limit estimates were given for flares because of large statistical uncertainties. Figure 8.1-1 summarizes the current results on the continuous flux limits for solar neutrons as summarized by Lockwood (private communication).

A recoil proton telescope was also flown on the OSO-6 satellite to search for solar neutrons. Details on the instrument are not currently available, but continuous flux limits have been presented (Leavitt et al., 1972) as $< 4 \times 10^{-4} \text{ cm}^{-2} \text{ sec}^{-1}$ for solar neutrons with energies greater than 40 MeV. Observations made by this instrument during solar activity are inconclusive.

A very interesting and new approach has recently been described by Kirsch, 1972, using mountain altitude cosmic ray neutron monitors. Monte Carlo calculations (Alsmiller et al., 1968) have been carried out which give the conversion efficiency of solar neutrons in the Earth's atmosphere for yielding secondary neutrons as a function of atmospheric depth. Therefore, Kirsch has used these basic results and calculated the efficiency for detecting different assumed solar neutron spectra at the altitudes of existing neutron monitors. For example, at 550 gm/cm^2 atmospheric depth, corresponding to the Chacaltaya monitor, the secondary neutron flux is 32% of the primary neutron flux assuming the producing proton spectrum at the sun has a characteristic rigidity of $R_0 = 125 \text{ MV}$. Of particular interest here is the study made of the Chacaltaya and Mina Aguilas monitor data during the November 12, 1960, event for which Lingenfelter and Ramaty, 1967, predicted significant neutron fluxes. They predicted a flux of $10^{-33} \text{ neutrons/cm}^2 \text{ sec}$ at the earth as a result of

3

solar neutron production in the slowing down phase after particle acceleration. Kirsch's analysis, 1972, indicates that the observed solar neutron flux is smaller by a factor of $10^{-2} - 10^{-3}$. Therefore, it is concluded that the assumption of isotropic proton emission from the solar flare region is not fulfilled. One of the basic difficulties with this technique is the fact that any solar neutron effect must override the diurnal variation of cosmic rays.

All of the more recent results discussed above are summarized in Table X and should be self-explanatory.

8.3

August 1972 Flare Measurement

In August 1972, the University of New Hampshire gamma ray detector aboard OSO-7 observed gamma ray lines and continuum emissions from the sun that were associated with the 3B flare on August 4 and the 3B flare on August 7, 1972. The 3B H α flare (on August 4) began at 0621 UT, reached its maximum intensity at 0638 UT, and ended at \sim 0852 UT (Preliminary Report SESE-PRF-Boulder 092, 093). The University of New Hampshire experiment measured the solar gamma ray line and continuum fluxes of August 4 until the satellite was eclipsed by the earth at 0633 UT.

On August 7 a 3B H α flare began at 1500 UT during satellite nighttime, and as the satellite emerged into the sunlight, excess gamma ray line radiation was observed.

August 4, 1972

Figure 8.3-1 shows the time-integrated solar and background gamma ray spectrum taken during the rise of the optical flare just before the satellite entered nighttime. The background quadrant spectrum shown is well below the corresponding solar quadrant flare spectrum. The solar spectrum is the sum of three normal, separate, consecutive, 3-minute scans, and the

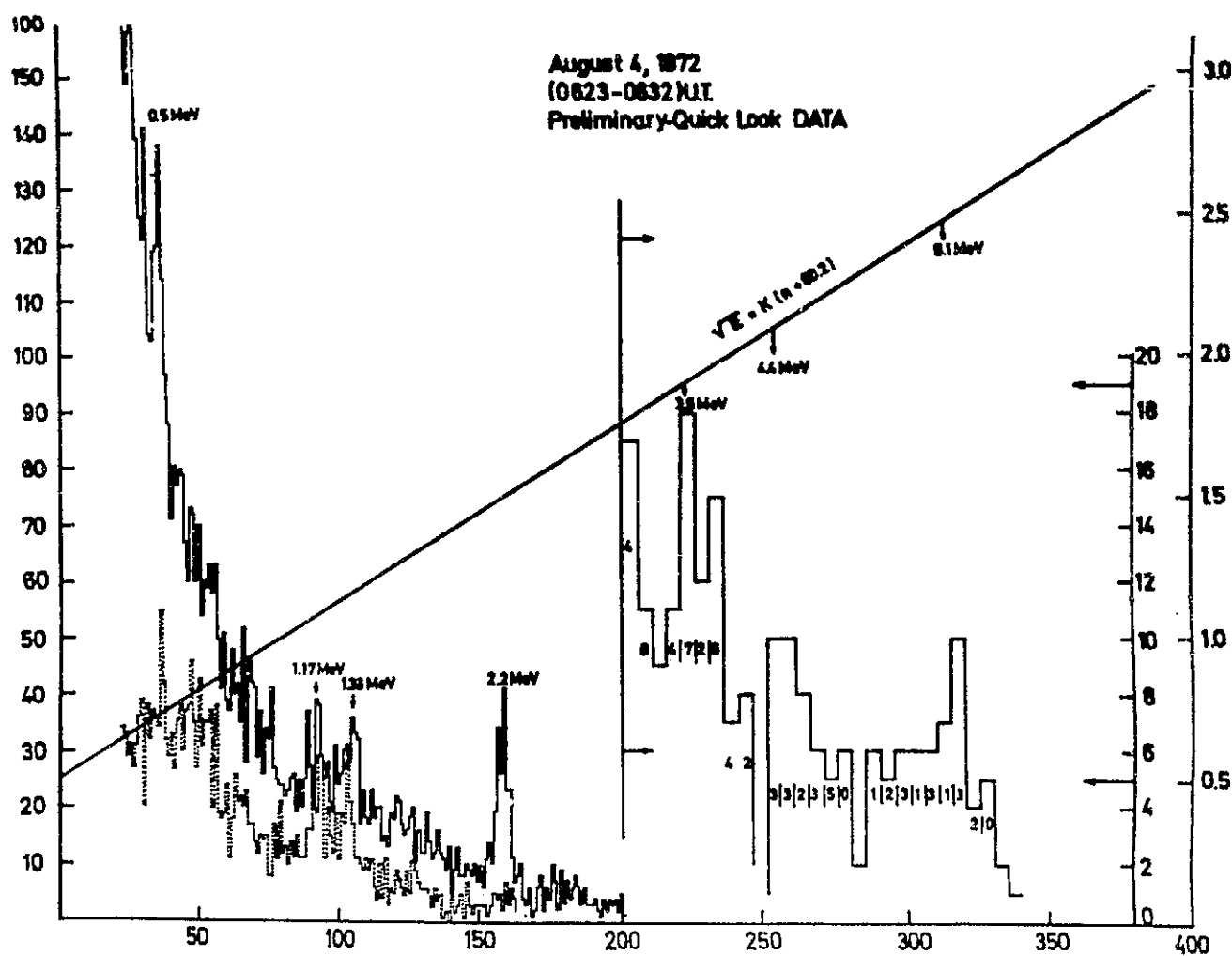


Figure 8.3-1

The time integrated gamma ray spectrum is shown plotted for the solar and background directions against the analyzed channel number. The left ordinate is the total counts observed in 91.4 seconds of livetime and applied to channels $n < 200$. The livetime for the background spectrum is 101 seconds. The inner ordinate on the right is the total counts in 5 consecutive channels and applies to channels $n > 200$. The outer ordinate in the square root of the gamma energy, \sqrt{E} , corresponding to a given channel number as given by the straight line $\sqrt{E} = k(n + 80.2)$ in the figure. The constants in the calibration curve are obtained from the inflight calibrations preceding and following the flare event, which is identified by the UT time and date shown.

ORIGINAL PAGE IS
OF POOR QUALITY

total live time for the summed spectrum is 91.4 seconds. In Figure 8.3-1 the left ordinate shows the counts observed in the indicated live time for the 0623-0632 UT time interval. The abscissa shows the channel number in which the counts are accumulated. Also above channel 200 the ordinate scale is shifted, as shown on the right, and to improve statistical accuracy the total number of counts in five consecutive channels is shown during the live time. The numbers under the histogram give the typical number of background counts observed in the five channels. On the far right ordinate the square root of the energy, \sqrt{E} , corresponding to a given channel according to the relation $E = k(n+n_0)^2$ is shown by the straight line in the figure. The constants, k and n_0 , are found from in-flight calibration data. The calibration curve is our best fit from the two calibrations which took place before and just after the event.

It is evident that only the solar quadrant gamma ray flux is significantly enhanced in both the ~ 0.5 - and 2.2-MeV spectral regions during the rise time of the optical flare. In addition, the general continuum below the line features is enhanced over the background quadrant thus indicating a continuum enhancement to above 2 MeV. Several comparison spectra showing solar and background rates before and after the flare were given by Chupp et al., 1973. Above channel 200, where the counts are summed in successive groups of five channels, there are three

or more statistically significant peaks. Because of the necessity of summing channels to improve statistics, it is not possible to specify precisely the photopeaks, but they may be associated with gamma rays of energies 3.4-3.8 MeV, 4.2-4.6 MeV, and 5.9-6.3 MeV, respectively. The leakage Co^{60} calibration lines at 1.17 and 1.33 MeV are also clearly evident in both the solar and the background spectra. Other features or possible photopeaks may be evident in the flare spectrum shown in Figure 8.3-1; however, we note with caution that it is necessary to separate out the hard x-ray burst spectrum before treating small features. This problem is the subject of a separate paper (Suri et al., 1973). It will be emphasized later that gamma ray line emissions are expected from the sun at all of these energies. In the case of the 4 and 6 MeV features, the association with photopeaks at 4.4 and 6.1 MeV is circumstantial, but gamma ray lines at these energies are expected at about the intensity shown.

The 4-channel x-ray spectrometer covering the energy range 7.5-120 keV also recorded the event in coincidence with the gamma ray spectrometer. Figure 8.3-2 (center) shows the counting rates in each x-ray channel versus time from \sim 0400 UT on August 4, 1972, until the eclipse of the satellite at \sim 0633 UT and for three successive orbits through the decay of the event. The rise of the event is recorded by each channel, with 30-second time resolution until saturation occurs in the

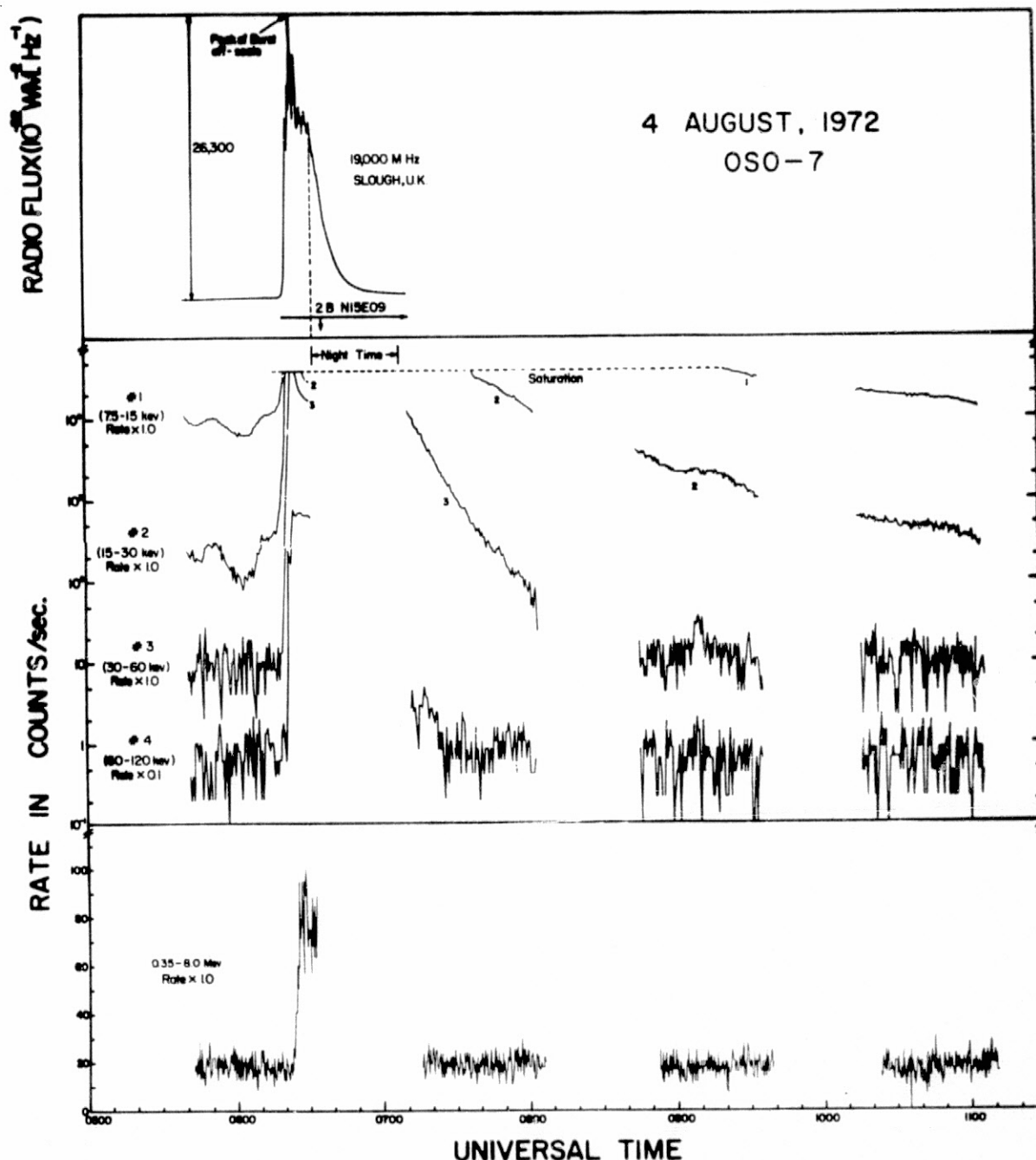


Figure 8.3-2

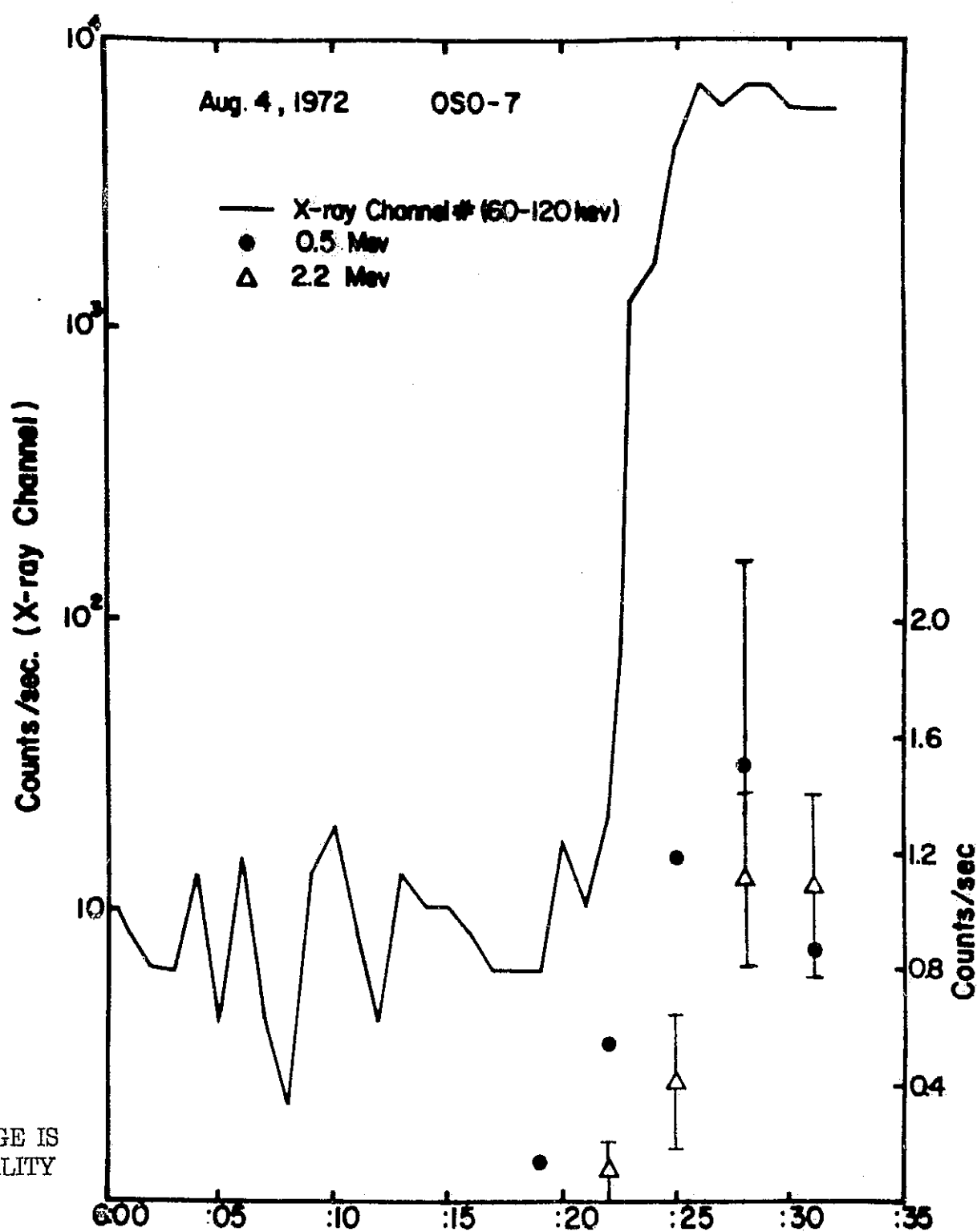
In the center portion of the figure, the uncorrected counting rates in each of the four X-ray channels is shown plotted against Universal Time on Aug. 4, 1972. The lower portion of the figure shows the uncorrected total counting rate in the gamma ray detector between the lowest and uppermost channels of the analyzer. The corresponding energy interval for this rate is 0.35-8.0 MeV. The radio flux is shown in the upper figure,

first 3 channels. The time of saturation occurs earlier as the mean energy of the x-rays is lower. The event seen in channel 3 (30-60 keV) begins to decay just before 0627 UT, well in advance of the eclipse by the earth. Also channel 4 (60-120 keV) does not saturate but reaches a plateau before being eclipsed. The lower part of Figure 8.3-2 shows the total counting rate in all gamma ray channels recorded with a rate meter with a 15-second time resolution. The top of Figure 8.3-2 shows the time history of the radio burst at 19,000 MHz as reported in UAG-21 (Lincoln and Leighton, 1972). The excellent correspondence in time between the radio, x-ray, and gamma ray continuum is self-evident.

A time history of the photopeak counting rate (before the eclipse) is shown in Figure 8.3-3 on an expanded time scale for the 0.5 and 2.2 MeV lines along with x-ray channel 4 (60-120 keV). After the OSO-7 returned to daylight at ~ 0705 UT there was no residual detectable evidence for gamma ray lines except for a weak indication of a 2.2 MeV flux at the 3σ level.

August 7, 1972

Unfortunately, the solar gamma rays observed during this event were recorded well after the rise and the maximum phase of the optical event since the satellite was in nighttime. Figure 8.3-4 shows a sequence of counting rate spectra which were



ORIGINAL PAGE IS
OF POOR QUALITY

Figure 8.3-3

The photopoint counting rates (right ordinate) shown for the 0.5 MeV and 2.2 MeV lines versus time during the August 4 event. The time profile (-) for the counting rate in one x-ray channel (60 - 120 kev) is shown (left ordinate) covering the period of satellite day from about 20 minutes before the optical onset and until the satellite went into eclipse.

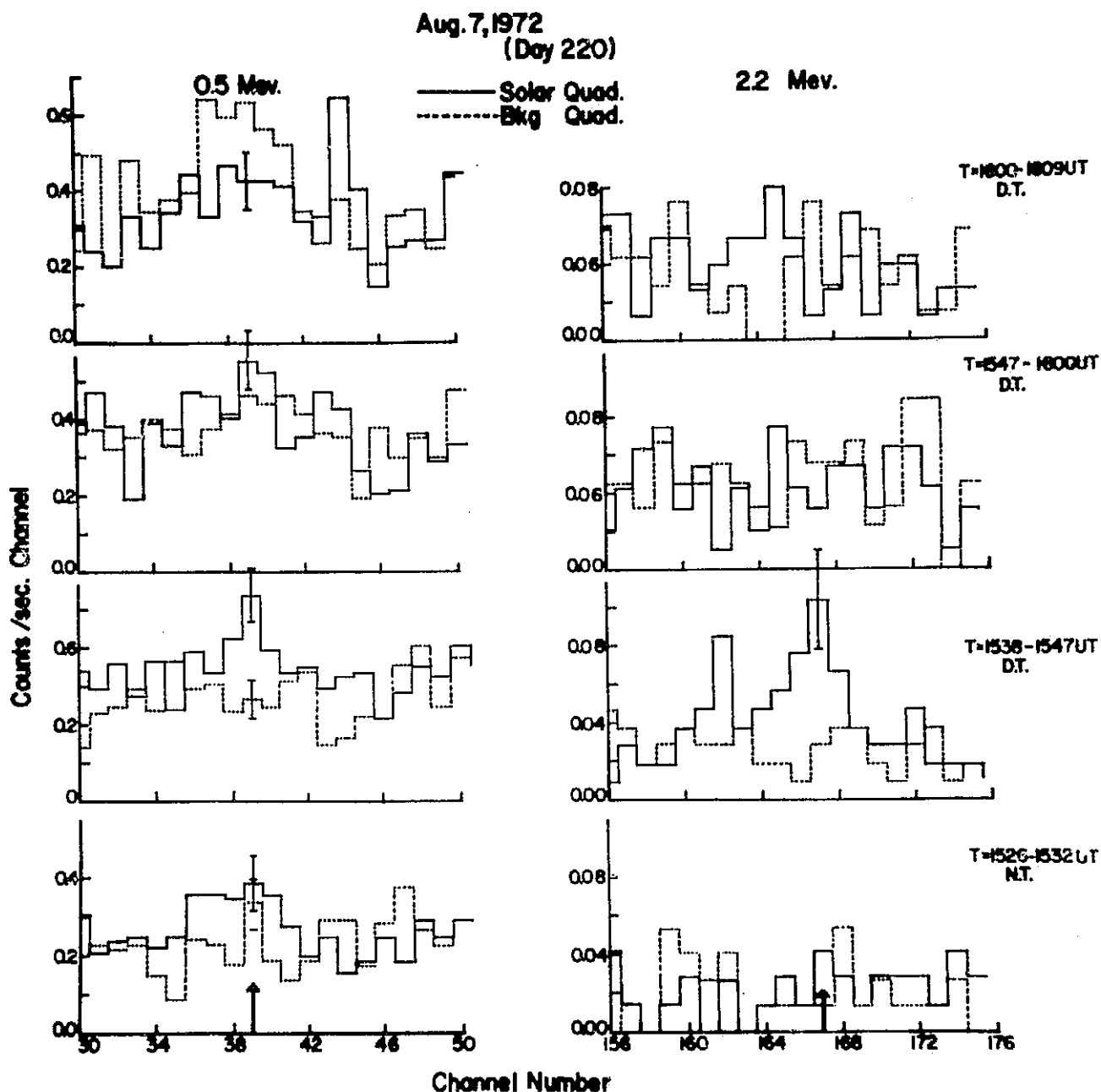


Figure 8.3-4

Gamma ray pulse height spectra are shown for the energy regions 435 keV - 610 keV (on the left) and for 2.1 MeV - 2.4 MeV (on the right) on August 7, 1972. The lower spectrum was taken at nighttime just before the satellite sunrise, but while the 3B optical flare was in progress.

ORIGINAL PAGE IS
OF POOR QUALITY

The second spectrum from the bottom was taken just after the sunrise calibration and during the declining phase of the optical flare. The top two spectra were taken at later times in the same orbit during the satellite daytime. The accumulation time intervals are shown for each spectrum. _____ Solar Quadrant, Background Quadrant.

taken at nighttime and during the satellite daytime period while the 3B H α flare was still in progress. In this figure only portions of the energy spectrum around 0.51 and 2.2 MeV are shown. The spectra shown are the sum of three separate, consecutive, full scans as indicated by the time interval of 9 minutes. By comparing the lowest spectrum (nighttime) with the spectrum immediately above it (daytime), it is evident that there are significant increases corresponding to photon energies of 0.5 and 2.2 MeV. In both figures the enhancement appears only in the solar quadrant spectra just after sunrise.

A remark should be made about the upper spectrum in Figure 8.3-4, which shows an increase in the 0.5-MeV region in the background quadrant. At this time quadrant was viewing the earth with good aspect but at lower rigidity ~ 3.0 GV; therefore, it registered atmospheric radiation. Atmospheric fluxes of 0.51-MeV radiation seen from OSO-7 are discussed separately (Dunphy, 1974).

8.4 Preliminary Interpretation

Several interesting inferences are now available from the OSO-7 observations. From the time profile of the 0.5- and 2.2 MeV lines shown in Figure 8.3-3 we can put an experimental upper limit on the acceleration time for solar protons during the flare of August 4. Since the time resolution of the instrument for the gamma lines is 3 minutes, one can see that the 0.5-MeV radiation rises to its maximum in no longer than about 10 minutes and it could be shorter. Unfortunately, the statistics are not good enough on the 4.4- and 6.1-MeV lines to plot a time profile curve. Such lines should show a time profile that is exactly that of the protons, since these are prompt reemissions. Further analysis of this data may improve this.

From elementary considerations we may also estimate the flux of protons at the sun required to produce the observed gamma ray intensity, assuming protons are released toward the photosphere. This is most easily done using the measured intensity of the 4.4- and 6.1-MeV gamma ray lines, since they are predominantly produced by protons in the energy range $E_p \sim 10-50$ MeV where the excitation cross-section is significant. The basic process giving rise to the gamma rays is inelastic scattering: The protons on C^{12} populate the first excited state at 4.4 MeV, followed by prompt deexcitation of the

excited nucleus with a characteristic emission line at 4.4 MeV. This process denoted as $C^{12}(P, P', \gamma)$ and source strength, S , at the sun may be expressed as:

$$S\left(\frac{\text{gammas}}{\text{sec}}\right) = N(n_i t) \sigma$$

where N is the number of protons per second incident on the solar atmosphere, $(n_i t)$ is the thickness of the target measured in the number of carbon nuclei cm^{-2} , and σ is the average inelastic excitation cross-section over the energy range 10-50 MeV. The target area density $n_i t$ may be expressed as:

$$(n_i t) = f_c R / m_p$$

where f_c is the fractional solar atmospheric atomic abundance of carbon relative to hydrogen $\sim 5.3 \times 10^{-4}$, R is proton range in hydrogen for 50-MeV protons, and m_p is the proton mass (grams).

The source strength obtained from the observed flux is $S(4.4) \sim 10^{26}$ photons per second emitted isotropically from the sun. Using this result, $R(50 \text{ MeV}) = 1 \text{ gcm}^{-2}$ and $\sigma(4.4) \sim 1.2 \times 10^{-25} \text{ cm}^2$, the proton current in the solar atmosphere is $N \approx 10^{30}$ protons per second. This means that over approximately the 1000 seconds the main burst lasted, about 2×10^{33} protons of energy 10-50 MeV were impinging into the denser solar atmosphere.

Deuteron production in the solar atmosphere from neutron capture may also be estimated from the observed flux of 2.2-MeV photons which also gives directly the production rate of such photons on the sun. Since this production rate is the capture rate of neutrons, it is also the production rate of deuterons by this source, and for the observed flux of 2×10^{-1} photons $\text{cm}^2\text{sec}^{-1}$, we find $\sim 6 \times 10^{26}$ deuterons produced per second by neutron capture. This is undoubtedly a very small source of deuterons since many more must be produced in the helium breakup reactions which produced the neutrons in the first place (Lingenfelter and Ramaty, 1967).

Further analysis of the OSO-7 solar events will be required before we can be sure of final conclusions and interpretations. One of the principal goals of further analysis is to determine if nuclear line emission is only observable in very large events or if it is more frequent and if its frequency is correlated with the frequency of the larger (X class) x-ray bursts. In addition, the gamma ray spectra will have to be studied very carefully for evidence of Doppler line shift or broadening. Finally, by correlating with solar proton observations, we hope to learn more about the spectrum of the protons accelerated at the sun.

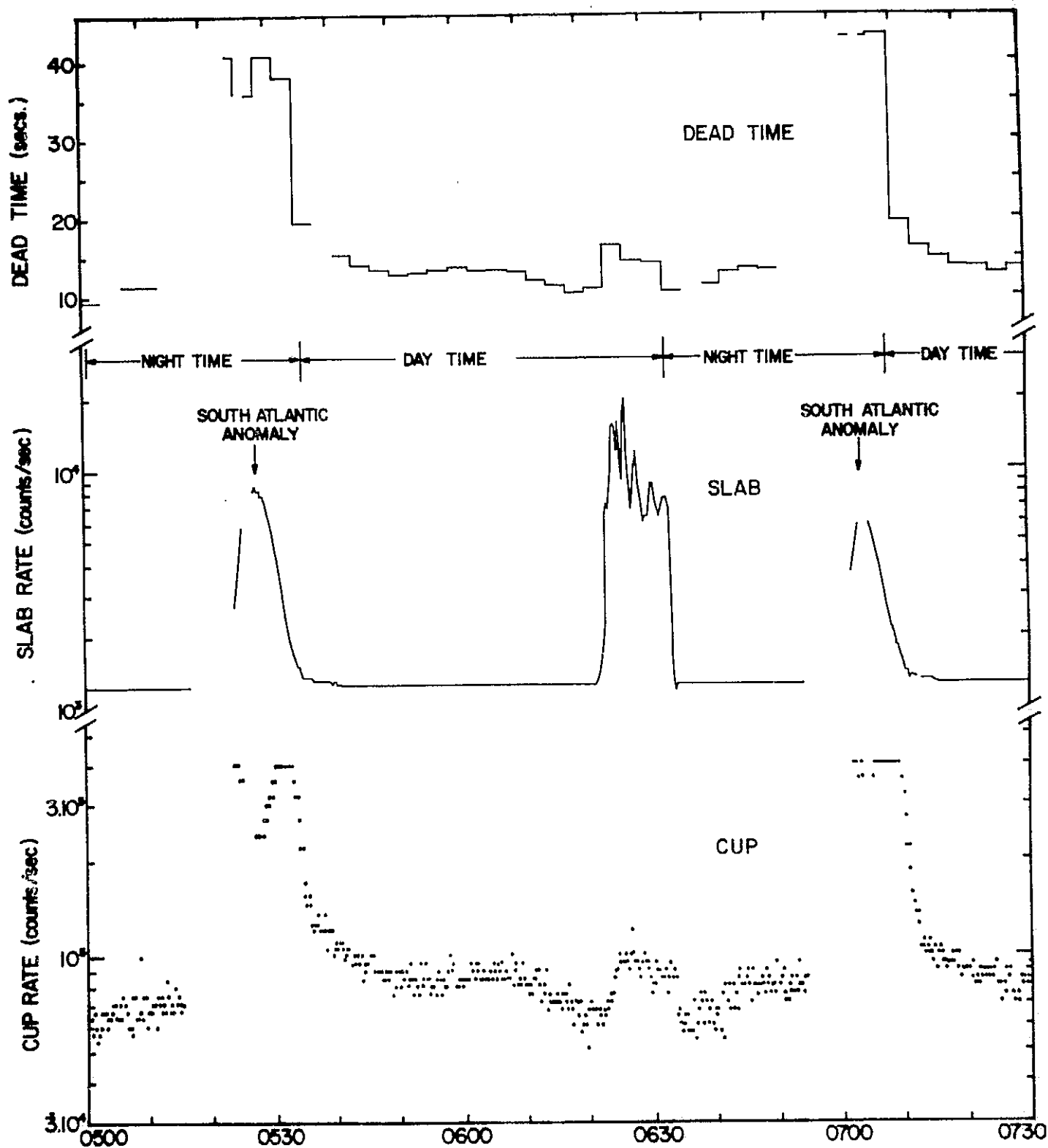
8.5 Justification as an Extraterrestrial Event

It must be considered that the events recorded by the UNH gamma ray monitor during August 1972 could be explained by local atmospheric and spacecraft background effects or the possibility of an atmospheric "hot spot".

The UNH detector has a wide angular response ($\sim 100^\circ$) that can graze the earth's atmosphere while in the solar direction and did graze it during part of the time interval under question. By a fortunate coincidence the satellite was in a high geomagnetic cutoff during both events. The cutoff on August 4 varied from 15.8-15 GV and on August 7 from 15-12 GV.

In Figure 8.5-1 we see a unique set of solar/background quadrant spectra. These unique spectra are only seen at the time of the flare; the detector did not record any similar spectra when the satellite was in a similar aspect to the earth's atmosphere on nonflare occasions.

The copious enhancement of low energy protons during the 2B event on August 2 could have produced solar protons raining into the earth's atmosphere. These protons would have flooded the spacecraft causing a background enhancement in both quadrants; this is the case in the South Atlantic anomaly.



UNIVERSAL TIME

Figure 8.5-1

ORIGINAL PAGE IS
OF POOR QUALITY

There is, in fact, no evidence for an excess flux of solar protons or precipitated trapped protons at the satellite during the timespan surrounding the flare observations. By looking at the shield counting rates in Figure 8.5-1, we see no abnormal enhancement. Trapped particle effects can be seen during passage through the South Atlantic anomaly well before and well after the flare observation. The flare gamma rays cause an increase in the shield rates which differ clearly in character from the trapped particle effects. This difference can also be seen between the respective dead time increases.

Another possible explanation of the gamma ray lines during the August events is a "hot spot" in the earth's atmosphere with no excess protons at the spacecraft and seen only in the solar quadrant. If this were a valid explanation, then the background quadrant would have seen the "hot spot" 15 minutes earlier because of the monitor's broad angle. No increased flux was seen in the background quadrant; therefore, the phenomenon would have to be on a short time scale and localized.

The spectra obtained in the solar quadrants during the flares must therefore be attributed to gamma rays from the sun.

8.6 Solar Flux Values

The largest flux values measured by the UNH detector on August 4 at 0621 UT are $(2.2 \pm 0.2) \times 10^{-1}$ and $(7 \pm 1.5) \times 10^{-2}$ photons $\text{cm}^{-2}\text{sec}^{-1}$, respectively, for the lines at 2.2 and 0.5 MeV.

The interpretation of these observations implies production of discrete gamma ray lines by a variety of high energy processes taking place in the solar atmosphere. The probable sources of the gamma ray lines are positrons and neutrons produced in the nuclear reactions and high energy protons. Annihilation of positrons with electrons produce the 0.51 MeV annihilation line, while the 2.23-MeV line results from the capture of neutrons by the hydrogen atoms. Inelastic scattering of fast protons on the less abundant C, N, O, and Ne nuclei produce a large number of weaker deexcitation gamma ray lines: 4.43 MeV (C^{12*}) and 6.13 MeV (O^{16*}) are likely to be the most prominent. We believe that the line features we observe in the 2B H α flare are the annihilation line (0.51 MeV), the neutron capture line (2.23 MeV), and the deexcitation lines C^{12*} (4.43 MeV) and O^{16*} (6.13 MeV).

Figure 8.3-4 is a plot of the counting rate spectra measured during the onset (nighttime) and declining phase (daytime) of the August 7 event. The first solar spectrum measured after the commencement of the satellite day shows

enhancement in the regions corresponding to the photon energies of 0.5 and 2.2 MeV. Although the enhancement is not as large as observed for the August 4 event, but since it appears only in the solar spectrum, it can be argued that it could not arise due to local satellite or atmospheric effects.

The enhancement in the background quadrant \sim 0.5-MeV region in the upper spectrum of Figure 8.3-4 is perhaps genuine. During this time the detector was looking at the earth with good aspect and picked up 0.51-MeV annihilation radiation from the atmosphere.

Table XI lists tentative fluxes at the earth for the gamma ray lines observed during the flares of August 4 and 7.

It is clear that the gamma ray production expected during the solar flares has now been observed; and in addition, the presence of simultaneous neutron production is indirectly confirmed through the observation of the 2.2-MeV gamma ray line.

By comparing the UNH measurements with radio, optical, and x-ray observations, it is possible to deduce several physical properties associated with the release of solar protons. The measurements show the time release of solar protons to be within 10 minutes of the start of the hard x-ray burst. From nuclear

ORIGINAL PAGE IS
OF POOR QUALITY

Table XI

Associated Flare and the time of Observations	Tentative Designations and Preliminary Solar Flux at 1AU Photons $\text{cm}^{-2}\text{sec}^{-1}$			
	0.5 MeV	2.2 MeV	4.4 MeV	6.1 MeV
2B (H α) 4 Aug 1972 0626 - 0632 UT (Before H α Max)	$(7\pm 1.5) \times 10^{-2}$	$(2.2\pm 0.2) \times 10^{-1}$	$(3\pm 1) \times 10^{-2}$	$(3\pm 1) \times 10^{-2}$
3B (H α) 7 Aug 1972 1538 - 1547 UT (After H α Max)	$(3.4\pm 1.1) \times 10^{-2}$	$(4.8\pm 1) \times 10^{-2}$	$< 2 \times 10^{-2}$	$< 2 \times 10^{-2}$

reaction rate estimates, the relative contributions are determined for various reactions to produce the several observed gamma ray lines.

8.7 Summary of Flare Results

1. Gamma ray lines were observed during the impulsive phase of the August 4, 1972 flare for ~ 10 minutes. It is likely this was also the case on August 7, 1972.

2. The number of protons required to produce the time-integrated gamma ray flux is 2×10^{33} with $E_p(> 30 \text{ MeV})$ on August 4, 1972.

3. The source of β^+ and neutron production and $(p,p'\gamma)$ reactions is due to nonthermal reactions of accelerated solar ions in the ambient solar atmosphere. Thermonuclear reactions do not appear to play any significant role.

4. A preliminary analysis of the continuum emission on August 4, 1972 (Suri et al., 1973) indicates that $\sim 5 \times 10^{36}$ electrons ($> 100 \text{ keV}$) were accelerated over ~ 600 seconds. From the hard x-rays (30-60 keV) on August 4 there is evidence for two stage electron acceleration in this event (Figure 8.3-2).

5. No white light observations are available during the initial phase of the August 4 event, so the time relation of these emissions to the protons is not verifiable.

6. The temperature and the density of the plasma in the positron-electron annihilation region is $< 7 \times 10^6 \text{°K}$ and $n_e \geq 1.6 \times 10^{11} \text{ cm}^{-3}$, respectively.

Two words of caution should be emphasized here:

1. The calculations on gamma ray and neutron production by charged particles in the solar atmosphere have not taken into account the directivity of the proton motion in solar magnetic fields. This will influence at least the neutron and positron production and the resulting gamma ray yields.

2. We must not generalize about flares and particle acceleration from this meager gamma ray data. As observed before and even during the August activity, there are cases of hard electron acceleration (e.g. 60-120 keV burst, August 2, 2055 UT) with no observable optical flare and no detectable gamma ray lines.

PLEASE NOTE: The initial scientific results presented here are essentially unmodified; see the list of reports and publications for further information and the most recent results.

8.8 Continuing Program - Solar Analysis

The analysis efforts that are continuing with this OSO-7 data in the field of solar physics are as follows:

1. Continue the theoretical interpretation and model development based on the solar gamma and x-ray observations made on August 4 and 7, 1972. This will include collaboration with other groups in data sharing and Monte Carlo calculations as required and possible. It should be pointed out that some of the interpretations and models depend not only on our gamma ray measurements but also on measurements of other particles and at other wavelengths which are just now becoming available.

2. Continue to search for gamma ray line and continuum emission from other smaller solar flares. This requires a systematic search based on correlation with other observations such as optical, radio, and x-ray measurements. We also intend to overlap in time numerous smaller flares and sum the spectra to increase our sensitivity for these smaller flares. In this task (and those described below) the data from our auxiliary x-ray detector will be used to help identify periods of solar activity. The overall proton energy range we can cover in this analysis is that covered by the gamma ray and x-ray detectors or from ~ 10 keV-10 MeV. The results of this effort could have an important bearing on some aspects of gamma ray production models mentioned in item 1 above.

3. Carry out a more detailed search for preflare and postflare emissions of gamma ray lines and continuum. The only analysis carried out so far has involved single events in the August 1972 series and has been negative. To test, for example, the Elliot model (Elliot, 1973), which predicts preflare gamma rays, it will be necessary to sum together data for several flares. Since the Elliot model suggests that protons may be stored for as long as a day before a flare, it will be necessary to carefully select appropriate time periods and normalize the spectra before summing. We expect to be able to achieve limiting flux sensitivities of 10^{-3} photons $\text{cm}^{-2}\text{sec}^{-1}$ in a line.

4. Initiate a study of the solar-geophysical gamma ray event which was observed on August 4, 1972 starting at ~ 1400 UT and continuing through the day. In this event gamma rays at the spacecraft were observed at low L values (< 2) starting several hours (~ 8) after the major flare. The evidence indicates these were locally produced gamma rays by protons impinging on the spacecraft and also gamma rays from the earth's atmosphere. To produce the observed gamma rays, protons with energies above ~ 10 MeV (which is, of course, well below the geomagnetic cutoff at the satellite) are required. This type of event may be similar to that reported by Sood et al., 1970, who observed an increase in the charged-particle

flux near the geomagnetic equator during a magnetic storm. In this case, however, the geomagnetic field was in the recovery phase following a magnetic storm.

In this phase of our analysis program, we intend to analyze this event thoroughly and search for other events. Such events may be examples of dumping of protons from the inner radiation belt and, therefore, may be of great value in understanding the loss of trapped particles.

5. Continue our collaborative efforts with the "Campaign for Integrated Observation of Solar Flares" (CINOF). This involves a detailed and comparative study of 9 small solar flares that occurred in June 1972. We have been invited to be a coordinator for this program. In addition, we intend to expand our collaborative efforts with the AFCRL (Air Force Cambridge Research Laboratory) Solar Radio Astronomy Group in Bedford, Massachusetts, in a joint and comparative study of selected solar events. We would like to study and compare the time history, spectral development, and energy content in the radio, x-ray, and gamma ray energy ranges.

6. Carry out a search for continuous (or quasi-stationary) emission of gamma ray lines or continuum from the sun, especially during undisturbed periods. This will complement the studies carried out in items 2 and 3 above,

which cover active periods. This study is important since we may be able to directly determine whether proton populations exist near the sun during nonactive periods.

7. In the course of carrying out the research proposed in item 6 above, we will have the data necessary to search for gamma rays associated with solar M regions. Such events, if discovered, would be similar to the recurrent solar cosmic ray events seen by McDonald and Desai, 1971. The results of such a study, if positive, will further our understanding of the trapping of solar particles.

8.9

Continuing Program - Cosmic Analysis

In the search for gamma ray objects and events with the large angular aperture OSO-7 gamma ray monitor, the objects and events can be put into four categories. These categories depend on whether the emission is in gamma ray lines or a gamma ray energy continuum and whether the objects are transient or steady in time. Table XII shows this schematically and gives some typical events or objects in each category.

The effectiveness of the gamma ray monitor is greatest for Category A and smallest for Category D. That is, for a given flux it is easier to identify an event and separate its effects from the detector's background if the event produces unique gamma ray lines and is transient in time, as compared to an event that produces a gamma ray continuum and is steady in time. Note that we have already observed events in Categories A and B during the solar flares of August 4 and 7, 1972.

We propose to study events in all categories with the OSO-7 data emphasizing the easier ones at first and then the more difficult ones as we continue to learn more about the detector's background intensity and spectral variations in time and space.

Some examples of cosmic objects and events in the four categories follow:

Table XII

Time	Gamma Ray Lines	Gamma Ray Continuum
Transient	A	B
	Diffuse Objects such as: 1. Older supernova remnants. 2. Solar flares. 3. New supernova.	Dense Objects such as: 1. New supernova. 2. Solar flares. 3. New γ ray bursts*.
Stable	C	D
	1. Gum Nebula. 2. Galactic Center and Disk.	1. Diffuse "isotropic" γ rays.

* Klebesadel et al. (1973)

ORIGINAL F
OF POOR C

A. Supernovae are expected to produce a large amount of radioactive isotopes during their flash phase. The gamma ray lines from these isotopes will be able to escape unscattered as soon as the shell expands enough to become thin compared to the gamma ray mean free path of $\sim 10 \text{ gcm}^{-2}$. This is expected to occur several months after the initial flash of the supernova, and its decay is then dependent only on the half-life of the radioactive isotopes. Clayton, 1973, has reviewed this problem and has pointed out that supernovae hidden optically in the galactic disk would be visible in gamma rays. An example of current interest is in the SN (Kowal, 1972) which occurred in the galaxy NGC 5253. The first observation was on May 13, 1972, and the OSO detector was viewing the direction to the galaxy in the night sky for some weeks. We have already carried out a search for gamma ray emissions in the early phases (~ 1 month) (Chupp et al., 1973), but according to the above arguments the gamma rays may be emitted later.

B. The first gamma ray evidence of a supernova is expected to be a broad energy continuous feature centered at $\sim 500 \text{ keV}$ (Brown, 1973). The feature is due to the Compton scattered photons from the radioactive isotopes trying to escape from the thick expanding shell. This is in the transient phase, but it is important to search for because the gamma ray flux may be most intense during this time period.

Another example of an event in this category is the gamma ray bursts recently reported from the Vela satellites (Klebesadel et al., 1973). We have searched our data during all the time periods when these gamma ray bursts have been reported with null results. Upper limit fluxes in our energy range are presently being determined, and they will be reported at the upcoming conference on these transient events. We furthermore plan to search for similar but as yet undetected gamma ray bursts in our data.

C. Time constant emission of gamma ray lines has also been suggested to arise in diffuse objects such as the Gum Nebula (Ramaty and Boldt, 1971) and the observation of a gamma ray line at 473 keV at a flux level of $\sim 2 \times 10^{-3} \text{ cm}^{-2}\text{sec}^{-1}$ has been reported (Johnson et al., 1972) from the Galactic Center. The flux level reported above should be well above our ultimate sensitivity after a careful summation of our data. Furthermore, some of the interpretations of this line predict strong emission at 4.43 and 6.13 MeV (Fishman and Clayton, 1972), which we would be able to observe.

D. Isotropic Gamma Ray Flux. This is possibly the most difficult analysis to make with the OSO-7 or any other detector (since the flux is independent of direction and a constant detector background would give the same kind of response). The upper limit that the analysis to date have

allowed us to set are consistent with the recent Apollo 15 results (Trombka et al., 1972). However, careful interpretation and removal of our detector backgrounds, especially at higher energies, will allow us to determine absolute flux levels. The 10-to-1 sensitivity difference between our front to back directions gives the OSO-7 detector an advantage over the one used on Apollo 15. Figure 8.9-1 shows, for illustration, a comparison of our detector's energy loss spectrum with that of Apollo 15. This, of course, is the raw data we must start with before determining a gamma ray spectrum. The data shown are not necessarily inconsistent since our instrument has directional properties and a different energy response function than the Apollo detector's.

It should be emphasized that this problem is one of the most fundamental in physics that can be studied with our instrument. Very likely the only experimental test of the big bang matter and antimatter cosmology (Ormes, 1973) is the detection of the red-shifted annihilation photons which could produce a bump in the gamma ray spectrum at ~ 1 MeV. It is therefore essential that the OSO-7 data be used to study this problem in order to confirm or refute the Apollo 15 observations (see also Stecker et al., 1971).

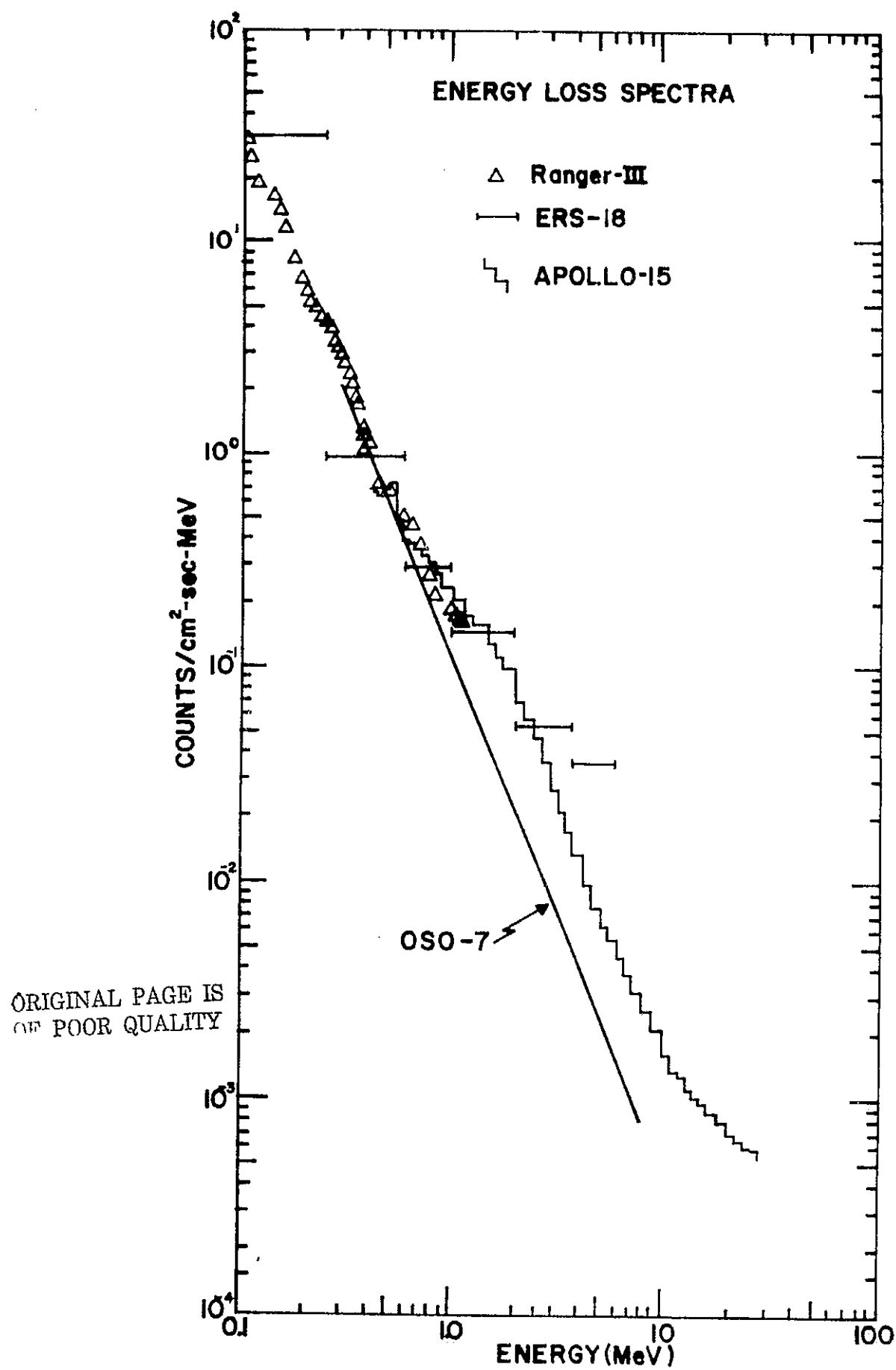


Figure 8.9-1

In this summary we have identified several scientific problems that our data applies to in cosmic gamma ray astronomy. We feel that we can determine definitive answers to some of these problems. These include the presence of the gamma ray line flux from the Galactic Center and the intensity of the isotropic gamma ray flux, especially above 2.5 MeV. In the search for gamma ray lines from the galactic disk, even upper limits would set constraints on the rate of and/or nature of supernovae in our galaxy. Furthermore, we have tried to program analysis procedure so that unexpected or unanticipated phenomena (such as the gamma ray bursts) can be detected and studied.

9.1 New Technology

This instrument incorporates the following significant improvements in satellite gamma ray spectrometers;

1. Direct measurement of instrument dead time (see Section 3.8). This improves the counting rate measurement.
2. Quadratic pulse height analyzer (see Section 3.13). This improves our data collection rate by a factor of 3 over an equivalent resolution linear analyzer (Burtis et al., 1972).
3. Cobalt 60 radioactive source calibration (RS cal) (see Section 3.14.1). This technique employs a very efficient Co^{60} calibration source to provide several energy lines in the central detector. The development and fabrication of this source is discussed in Forrest et al., 1972 (see Appendix A).

References

- Alsmiller, R. G., Jr., R. I. Boughner, J. Geophys. Res. 73, 4935 (1968).
- Apparao, M. V. Krishna, R. R. Daniel, B. Vijayalakshmi, V. L. Bhatt, J. Geophys. Res. 71, 1781 (1966).
- Birks, J. B., The Theory and Practice of Scintillation Counting (N.Y.: Pergamon Press), p. 158, 1964.
- Brown, R. T., Ap. J. 179, 607 (1973).
- Burtis, D. W., D. Aalami, R. H. Evelyn-Veere, A. A. Sarkady, IEEE Trans. Nucl. Sci. NS-19, No. 1 (1972).
- Chupp, E. L., Space Sci. Rev. 12, 486 (1971).
- Chupp, E. L., D. J. Forrest, P. R. Higbie, A. N. Suri, C. Tsai, P. P. Dunphy, Nature 241, 333 (Feb. 2, 1973).
- Chupp, E. L., D. J. Forrest, A. N. Suri, R. Adams, C. Tsai, Proc. Int. Conf. on Supernovae, Lecce, Italy (May 1973).
- Clayton, D. D., Proc. Int. Symp. and Workshop on Gamma-Ray Astrophys., NASA/GSFC (May 1973).
- Cortellessa, A., P. D. C. Benedetto, C. Paizis, Solar Phys. 20, 474 (1971).
- Daniel, R. R., G. Joseph, P. J. Lavakare, R. Sunderrajan, Nature 213, 21 (1967).
- Daniel, R. R., G. S. Gokhale, G. Joseph, P. J. Lavakare, J. Geophys. Res. 76, 3152 (1971).
- Dunphy, P. P., Ph. D. Thesis, Physics Dept., Univ. of N. H. (1974).
- Elliot, H., in Solar Flares and Space Research, (ed. by C. de Jager and Z. Svestka), North-Holland Pub. Co., Amsterdam, (1969), p. 356.
- Elliot, H., in High Energy Phenomena on the Sun (Washington, D.C.: NASA Sci. & Tech. Office), NASA SP-342, 1973.

- Eyles, C. J., A. D. Linney, G. K. Rochester, Solar Phys. 24, 483 (1972).
- Fishman, G. J., and D. D. Clayton, Ap. J. 178, 337 (1972).
- Forrest, D. J., E. L. Chupp, Solar Phys. 6, 339 (1969).
- Forrest, D. J., P. R. Higbie, L. E. Orwig, E. L. Chupp, Nucl. Instrum. Methods 101, 567 (1972).
- Higbie, P. R., E. L. Chupp, D. J. Forrest, I. U. Gleske, IEEE Trans. Nucl. Sci. NS-19, No. 1 (Feb. 1972).
- Hirasima, Y., K. Okudaira, T. Yamagami, Acta Phys. 29, Suppl. 2, 683 (1970).
- Holt, S. S., J. Geophys. Res. 72, 3507 (1967).
- Johnson, W. N., III, F. R. Harnden, Jr., R. C. Haymes, Ap. J. 172, L1 (1972).
- Joseph, G., Thesis, University of Bombay, India, 1970.
- Kirsch, E., Solar Phys. (1972).
- Klebesadel, R. W., I. B. Strong, R. A. Olson, Ap. J. 182, L85 (1973).
- Kondo, I., F. Nagese, in Solar Flares and Space Research, (ed. by C. de Jager and Z. Svestka), North-Holland Pub. Co., Amsterdam, (1969), p. 135.
- Kowal, C. T., IAU Circular 2405 Central Bureau for Astronomical Telegrams, Smithsonian Astrophysical Observatory, Cambridge, Massachusetts.
- Leavitt, C. P., D. S. Robb, F. Young, Bull. Am. Phys. Soc. 17, 687 (1972).
- Lincoln, J. Virginia and Hope I. Leighton, World Data Center A. Report UAG-21, U.S. Dept. of Commerce, NOAA, Environmental Data Service, Ashville, North Carolina, Nov. 1972.

- Lingenfelter, R. E., R. Ramaty, in High Energy Nuclear Reactions in Astrophysics, (ed. by B. S. P. Shen), W. A. Benjamin Press, New York, (1967)., p. 99.
- Lockwood, J. A., S. O. Ifedili, R. W. Jenkins, Solar Phys. (1972).
- McDonald, F. B., and U. D. Desai, J. Geophys. Res. 76, 808 (1971).
- ~~Omnes~~, R., "Physics at the Origin of Time," unpublished report (1973). See also F.W. STECKER and J.I. TROMBKA (EDS.), GAMMA-RAY ASTROPHYSICS NASA SP-339, 335, WASHINGTON, D.C. (1973)
- Purvis, A. E. and L. C. Baggerly, Nucl. Instrum. Methods 60, 179-181 (1968).
- Ramaty, R., and E. A. Boldt, GSFC Report on the Gum Nebula and Related Problems X-683-71-375 (1971).
- Sood, R. K., Solar Phys. 23, 183 (1972).
- Sood, R. K., C. A. Green, and H. Elliot, Acta Physica Hung. 29, Suppl. 2, 657 (1970).
- Stecker, F. W., D. L. Morgan, Jr., J. Bredekamp, Phys. Rev. Letters. 27, 1469 (1971).
- Suri, A. N., D. J. Forrest, E. L. Chupp, C. R. Reppin, Bull. Am. Phys. Soc. 18, No. 4 (1973).
- Suri, A. N.
in preparation (1974).
- Trombka, J. I., A. E. Metzger, J. R. Arnold, J. L. Matteson, R. C. Reedy, L. E. Peterson, GSFC-NASA preprint X-641-72-421 (1972).

List of Reports and Publications

The work described in the following papers was supported by NASA under Contract Nas 5-11054.

Published Papers1969

"Onboard Calibration System for Gamma Ray Spectrometers in Space Satellites," E. L. Chupp, P. J. Lavakare, A. A. Sarkady. IEEE Trans. Nucl. Sci. NS-16, No. 1 (1969).

1972

"An Electrically Gated Gamma and X-ray Calibration Scheme," D. J. Forrest, P. R. Higbie, L. E. Orwig, and E. L. Chupp. Nucl. Instrum. Methods 101, 567 (1972).

"A Gamma Ray Monitor for the OSO-7 Spacecraft," P. R. Higbie, E. L. Chupp, D. J. Forrest, I. U. Gleske. IEEE Trans. Nucl. Sci. NS-19, 606 (1972).

1973

"Experimental Gamma Ray Response Function for the OSO-7 Spacecraft," P. R. Higbie, D. J. Forrest, I. U. Gleske, E. L. Chupp, and D. W. Burtis. Nucl. Instrum. Methods 108, 167 (1973).

"Solar Gamma Ray and Neutron Observations," E. L. Chupp, D. J. Forrest, and A. N. Suri. High Energy Phenomena on the Sun (Washington, D.C.: NASA Sci. & Tech. Office), NASA SP-342, p. 285-300, 1973.

"Observations of Solar Gamma Ray Lines During the Solar Activity of 02 August to 11 August 1972," E. L. Chupp, D. J. Forrest, P. R. Higbie, A. N. Suri, C. Tsai, and P. P. Dunphy. Nature 241, 333 (1973).

"Solar Neutron Production during the Events on 04 and 07 August 1972," C. Reppin, E. L. Chupp, D. J. Forrest, and A. N. Suri. Conference Papers - 13th International Cosmic Ray Conference (Denver, Colo.: Univ. of Denver), Vol. 2, p. 1577-1582, 1973.

"Gamma Ray Observations during the August 1972 Solar Activity," E. L. Chupp, D. J. Forrest, and A. N. Suri. Correlated Interplanetary and Magnetospheric Observations (Dordrecht, Holland: D. Reidel Publishing Company), p. 450-462, 1973.

"Observations of Gamma-Ray Emission in Solar Flares," D. J. Forrest, E. L. Chupp, A. N. Suri, and C. Reppin. Gamma-Ray Astrophysics (Washington, D.C.: NASA Sci. & Tech. Office), NASA SP-339, p. 165-174, 1973.

"Gamma Ray Observations from OSO-7 (26 July to 14 August 1972)," E. L. Chupp, D. J. Forrest, C. Reppin, A. N. Suri, and C. Tsai. World Data Center A for Solar-Terrestrial Physics (Asheville, N.C.: NOAA Environmental Data Service), UAG Report 28, Part II, p. 325-329, 1973.

"Gamma Ray Emissions from McMath Region 11976," E. L. Chupp, D. J. Forrest, A. N. Suri, and C. Reppin. Conference Papers - 13th International Cosmic Ray Conference (Denver, Colo.: Univ. of Denver), Vol. 2, p. 1595-1601, 1973.

1974

"Solar Burst at $\lambda=2$ cm on July 31, 1972," J. P. Castelli, D. A. Guidice, D. J. Forrest, R. R. Babcock. J. Geophys. Res. 889, 79 (1974).

"Search for Gamma Ray Lines from Supernovae and Supernova Remnants," E. L. Chupp, D. J. Forrest, A. N. Suri, Ron Adams, and C. Tsai. Supernovae and Supernova Remnants (Dordrecht, Holland: D. Reidel Publishing Company), p. 311-316, 1974.

"Gamma-Ray and Neutron Measurements and their Relation to the Solar Flare Problem," E. L. Chupp, D. J. Forrest, and A. N. Suri. Space Res. XIV, 463 (1974).

"Prospects and Problems for Experimental Gamma Ray Line Astronomy," E. L. Chupp. In Proc. of Seminar on the Problem of Particle Acceleration and Nuclear Reaction in Space (Leningrad, USSR), August 19-21, 1974.

"High Energy Gamma Ray Radiation Above 300 keV Associated with Solar Activity," E. L. Chupp, D. J. Forrest, and A. N. Suri. In Proc. of the Joint IAU-COSPAR Symposium (Buenos Aires, Argentina), June 11-14, 1974.

"Solar Gamma Rays and Other Nuclear Secondaries," D. J. Forrest, E. L. Chupp, and A. N. Suri. In Proc. of X-rays in Space Conference (Calgary, Alberta), August 14-21, 1974.

Abstracts1972

"Capabilities for Celestial Nuclear Gamma Ray Monitoring on OSO-7," E. L. Chupp, D. J. Forrest, and P. R. Higbie. Bull. Am. Astron. Soc. 4, 228 (1972).

"Flare Nuclear Gamma Ray Line Search by OSO-7," D. J. Forrest, A. N. Suri, and E. L. Chupp. Presented at 3rd Workshop on OSO's (Stanford University), September 5-8, 1972.

"Solar Gamma Ray Line Observations Associated with Solar Flares in Early August 1972," D. J. Forrest, E. L. Chupp, A. N. Suri, P. R. Higbie, C. Tsai, and P. P. Dunphy. Presented at AGU Meeting (San Francisco), December 4-7, 1972.

"Search for Solar Nuclear Gamma Rays Associated with \geq Class M X-rays on OSO-7," E. L. Chupp, D. J. Forrest, P. R. Higbie, and C. Tsai. Presented at 53rd Meeting of the AGU (Washington, D.C.), 1972.

1973

"Line Width of Solar Flare Gamma Ray Emissions," P. P. Dunphy, E. L. Chupp, D. J. Forrest, and A. N. Suri. Bull. Am. Phys. Soc. 18, Series II, 695 (1973).

"Continuum Solar X-ray and Gamma Ray Observations on August 4, 1972," A. N. Suri, D. J. Forrest, E. L. Chupp, and C. Reppin. Bull. Am. Phys. Soc. 18, Series II, 695 (1973).

"Review of Solar Gamma Ray Observations in August 1972," E. L. Chupp. Presented at 7th ESLAB Symposium (Saulgau, Germany), May 22-25, 1973.

"Search for Gamma Ray Bursts with the Gamma Ray Monitor on OSO-7," D. J. Forrest, C. Tsai, and E. L. Chupp. Presented at the Workshop/Conference on Transient Cosmic Gamma and X-ray Sources (Los Alamos, New Mexico), September 1973.

"Gamma Ray Production in Solar Flares," E. L. Chupp, D. J. Forrest, and A. N. Suri. Bull. Am. Phys. Soc. 18, Series II, 100 (1973).

1974

"Solar Flare Nuclear Secondaries," D. J. Forrest, E. L. Chupp, A. N. Suri, and P. P. Dunphy. Bull. Am. Phys. Soc. 19, Series II, No. 4, 458 (1974).

"OSO-7 Limits on the Line Emissions from the Galactic Center Region," A. N. Suri, P. P. Dunphy, E. L. Chupp, and D. J. Forrest. Bull. Am. Phys. Soc. 19, Series II, No. 4, 531 (1974).

"Gamma Ray Lines in Solar Flares," E. L. Chupp. Bull. Am. Phys. Soc. 19, Series II, No. 1, 14 (1974).

In-House Reports

1972

"A Data Analysis System for the Gamma Ray Monitor on OSO-7," P. R. Higbie, A. Buck, S. Croteau, M. Simmons, E. L. Chupp, and D. J. Forrest.

"OSO-7 UNH Gamma Ray Monitor Central Detector," I. U. Gleske.

"Background Effects from the UNH Gamma Ray Monitor on OSO-7," D. J. Forrest. Presented at Gamma Ray Local Production and Shielding Conference (Durham, N.H.), June 1972.

1974

"General Characteristics of Gamma Ray Counting Rates from the OSO-7 Spacecraft," M. R. Fernald.

"A Function to Predict Integrated Counting Rates from the OSO-7 Gamma Ray Detector," Mark R. Fernald.

Theses

1971

"Autocorrelation and Power Spectrum Analysis for X-ray and Gamma Ray Spectrometer Data," Chung-jen Tsai. Master's Thesis, University of New Hampshire (Physics Department).

1974

"Analysis of the 0.511 MeV Radiation at the OSO-7 Satellite," P. P. Dunphy. Ph.D. Thesis, University of New Hampshire (Physics Department).

Papers in Preparation

"Interpretation of the Width and Energy of the Positron Annihilation Gamma Ray Line Observed during the Flares of 4 and 7 August 1972," P. P. Dunphy, E. L. Chupp, D. J. Forrest, A. N. Suri, and C. Tsai.

List of Abbreviations

AFCRL	Air Force Cambridge Research Lab
AQM	Alternate quadrant mode
ASC	Analog subcom
A/D	Analog to digital
BBRC	Ball Brothers Research Corporation
bps	Bytes per second
CP	Charged particle
CSP	Charge-sensitive preamp
DNL	Differential nonlinearity
D/A	Digital to analog
ETR	Eastern Test Range
EDC	Extended dead time circuit
GRM	Gamma ray monitor
HV	High voltage
HVPS	High voltage power supply
IFC	In-flight calibration
IC	Integrated circuit
LCRM	Log count rate meter
LVPS	Low voltage power supply
MF	Main frame
NQM	Normal quadrant mode
OCC	Operations Control Center
OSO	Orbiting Solar Observatory

PM	Photomultiplier
PMT	Photomultiplier tube
PHA	Pulse height analyzer
Q/L	Quick look
RS cal	Radioactive source calibration
rpm	Revolutions per minute
S/C	Spacecraft
T_D	Dead time
T_L	Live time
T-Z	Time-Zero Corporation
UT	Universal time
UNH	University of New Hampshire
VA	Van Allen
WASC	Wheel analog subcom

AN ELECTRONICALLY GATED GAMMA AND X-RAY CALIBRATION SCHEME*

D. J. FORREST, P. R. HIGBIE, L. E. ORWIG and E. L. CHUPP

Department of Physics, University of New Hampshire, Durham, New Hampshire 03824, U.S.A.

Received 22 February 1972

Gamma and X-ray calibration sources can be made by placing specific radioactive isotopes into small scintillator buttons in which more than 98% of the emitted photons are accompanied by electronic gating pulses. This property allows these sources to be used in a number of different spectrometry calibration schemes without the disadvantage of introducing extra counts

into an unknown spectrum of interest. Fabrication techniques and test results for calibration sources using ^{60}Co will be given. We will also describe a closed-loop system using these sources, that automatically corrects for gain variations in real time and is designed for a balloon flight, and an externally commanded system for a satellite.

1. Introduction

Any X-ray or gamma ray spectrometry measurement requires, by definition, an energy calibration. It also requires very good gain stability if the energy resolution of the measurement is not to be compromised. The requirements on gain stability are becoming more critical as higher resolution detectors come more into use. This is especially a problem in space research and other experiments where the detector must be left unattended for long periods of time and where external conditions and counting rates can change.

The usual method of determining an energy calibration is to accumulate spectra before and/or after the measurement of interest with radioactive sources having spectral lines of known energy. This, of course, provides no information on the system gain in the time between the calibration runs; hence great care is required in the design of the experimental equipment to minimize temperature, counting rate, and other effects which can change the system gain.

Another method is to place a weak radioactive source near the experiment and to accumulate its spectrum with the spectrum of interest. This method provides information on gain changes during the run of interest, but it does not provide any correction if a gain change does occur. However, if the complete spectrum is taken in the form of many short runs, then computer techniques¹⁾ can be used to correct for gain changes and the short runs can be added together to produce a final spectrum. This method has the disadvantage that the calibration peak must stand above the normal background in order to be recognized so a gain correction can be applied. While

computer techniques can remove the calibration peaks, the statistical inaccuracies due to the external counts cannot be removed.

A more sophisticated method would be to use a digital spectrum stabilizer loop. This method automatically corrects for any gain changes in real time by comparing the counting rates in two small equal energy windows on each side of a calibration peak. Counts in these windows are determined by inspecting the digital output of the pulse height analyzer and gain corrections are made in the analog section of the detector-amplifier pulse height analyzer chain of circuitry. Hence all portions of the detector and electronics affecting gain are within the closed loop. The normal gain situation is achieved when there are equal counts in each window. If a gain change occurs such that the calibration peak moves toward one of the fixed predetermined windows then the counting rate in that window will increase while that in the other window will decrease. This condition provides the signal for a gain correction to re-equalize the counting rate. If two such stabilizers are used, one at the lower end of the pulse height spectrum to control the zero level and one at the higher end to control the gain, then the linearity of the system is the only parameter that must remain stable to be assured that the energy calibration is known and constant at all times.

It should be noted, however, that there are several disadvantages to this system. The first is that in the usual setup the spectrum of the external radioactive calibration source is superimposed on the pulse height spectrum of interest. Another disadvantage is that the gain correction signals depend on the statistical fluctuations of the counting rate in the two windows.

* This work was supported by NASA under Grant NGL 30-002-021 and Contract N45-11054.

Ferguson²) has shown that while the average gain can be held constant, the gain fluctuations can cause an effective decrease in the energy resolution. This would occur if the gain change per count is of the same order as the detector's characteristic energy resolution. However, if an external gain change does occur, it is the product of the gain change per count and the total calibration peak counting rate that allows the stabilizer to keep the peak in the correct pulse height channel. The above conditions are made worse if the calibration peak is riding on a background counting rate. For this reason the intensity in the calibration peak must be picked keeping the worst case background in mind if the background rate may change during the run of interest.

This paper describes the construction details and uses of a radioactive calibration source, which produces an electronic gating pulse when a calibration gamma ray is emitted. The presence of this gating pulse allows the use of this source in any of the above calibration or stabilizing schemes without the disadvantage of introducing extra counts into the unknown spectrum. Basically the method for doing this is to incorporate a radioactive isotope, which emits both a gamma ray and a charged particle in coincidence, into a scintillator (either organic or inorganic). Hence, whenever a gamma ray is emitted, a light pulse is produced in the scintillator due to the stopping of the associated charged particle. A photomultiplier is used to generate the gating pulse from this light pulse.

The sources to be described are reasonably easy to construct, have the ability of producing gating efficiencies $\approx 98\%$, and are radioactively safe to prepare and use. The gating efficiency is defined as the probability of producing a gating pulse when ever a gamma ray is emitted.

2. Fabrication of sources

To be useful in this calibration scheme, the isotope must satisfy the following criteria: a) all gamma rays must be emitted in prompt coincidence with a charged particle which can be detected with high efficiency, b) there should be at least one and preferably two or more gamma ray lines in the energy range of interest, c) the isotope should have a relatively long half life.

In the MeV range an isotope that satisfies all these requirements is ^{60}Co . This isotope ($T_{1/2} = 5.26$ y) emits a β^- ($E_{\text{max}} = 0.313$ MeV) in prompt coincidence with two cascade gamma rays with energies of 1.33 and 1.17 MeV in 99% of the decays. In the keV energy range ^{241}Am has been used. ^{241}Am emits

gamma rays of energies 0.059 and 0.026 MeV in prompt coincidence with alpha particles of ≈ 5.5 MeV. In neither case are these photons emitted without an associated charged particle.

An earlier paper by one of the authors³) describes a calibration scheme similar to the one described here. ^{60}Co calibration source in this case was made by placing a small amount (≈ 0.003 μCi) of radioactive $^{60}\text{CoCl}_2$ on top of a thin plastic scintillator disk. A second disk was then placed on top of the first covering the $^{60}\text{CoCl}_2$. It was found that by applying heat and pressure, the two disks could be fused together thereby permanently encapsulating the radioactive source. The gating efficiency of different sources of this type although sometimes as high as 90% was highly variable and averaged about 70%. It was felt that the reason for the low and variable gating efficiency was due to self-absorption of the low energy beta's in the $^{60}\text{CoCl}_2$ residue between the two plastic scintillator disks. Hence to improve the gating efficiency, a way had to be found to uniformly mix the radioactive ^{60}Co within the plastic scintillator.

We have found two methods of doing this, both resulting in gating efficiencies of at least 98%. The first method consists of mixing a small amount of an organic ^{59}Co compound into an unpolymerized plastic scintillator compound. The scintillator can then be polymerized and after curing can be cut and polished to the desired shape. The complete unit is then placed in a thermal neutron beam from a nuclear reactor and a portion of the ^{59}Co is activated to radioactive ^{60}Co . The main advantage of this method is that all handling, cutting, and polishing of the plastic scintillator takes place before the plastic is radioactive. The main disadvantage is that not only is the light output of the plastic scintillator quenched by the addition of the foreign cobalt compound but that it is further reduced by the radiation damage the scintillator receives during the thermal neutron activation of the ^{59}Co .

The second method of fabrication avoids this last cause of light reduction in that the ^{59}Co compound is activated before it is mixed with the unpolymerized plastic scintillator. It does have the disadvantage, however, of the need to cut and polish a radioactive material with its accompanying problems and need for special facilities.

For preparing the ^{60}Co calibration source an organic compound [cobalt octoate, $\text{Co}(\text{2-ethylhexanoate})_2$] was mixed in benzene such that it contained 1 mole of ^{59}Co per liter of solution. The scintillator material was Pilot M Partially Polymerized Plastic Scintillator

ELECTRONICALLY GATED GAMMA AND X-RAY CALIBRATION SCHEME

(Pilot Chemicals, Inc., 36 Pleasant Street, Watertown, Massachusetts 02172, U.S.A.).

For the first method (polymerized scintillator with the cobalt activated together) the cobalt solution was mixed into the unpolymerized scintillator in various concentrations ranging from 0.03% to 0.5% by volume. After polymerization the composite scintillators were cut and polished into right cylinders with volumes of $\approx 0.5 \text{ cm}^3$. Control samples with no cobalt were also prepared. Samples with the different ^{59}Co concentrations were then activated in the MIT Research Reactor using the pneumatic tube facility.

The thermal neutron flux during irradiation was $2.2 \times 10^{13}/\text{cm}^2\text{s}$ and the gamma dose rate was $1.3 \times 10^8 \text{ R/h}$.

The irradiated pellets were all checked for surface contamination by a standard wipe test with no observable effect. They were then rated according to their relative light output when exposed to 5.5 MeV α -rays from ^{241}Am . The accuracy of the light output measurements was limited to approximately $\pm 20\%$ because of different polishes and scintillator sizes. This test with neutron irradiated samples that did not contain the cobalt showed that the dose received did indeed quench the scintillator light output. The effect observed seemed to be well predicted by the equation given by Birks⁴). He gives the light attenuation as

$$I/I_0 = \exp(-\alpha D),$$

where D is the radiation dose in erg/g . The quantity

α is a physical parameter characteristic of the scintillator used and has a value of $\approx 1.5 \times 10^{-10} \text{ g/erg}$.

The combined effects of quenching from both the addition of the cobalt compound and the radiation dose were more difficult to determine. For the range of concentration and doses we used, it seemed that the effects of each were about the same. Our requirement called for a specific activity of $\approx 2 \times 10^3$ disintegrations per cm^3 of scintillator. This could be achieved by irradiating a sample doped with 0.5% by volume of the cobalt compound for 4 min, 0.25% for 8 min or 0.1% for 20 min. In each case the relative scintillator efficiency was $\approx 50\%$ that of an undoped and unactivated sample. A summation of these results is shown in table 1.

The gating efficiency with any of these sources when the plastic ^{60}Co scintillator was placed directly on the face of the photomultiplier was $\approx 98\%$. The gating efficiency (ϵ) is defined as:

$$\epsilon = \frac{G}{G + NG} = \frac{G}{T - Bkg},$$

where G is the coincidence rate between NaI and plastic ^{60}Co unit, NG is the rate of ^{60}Co events in NaI detector not accompanied by a plastic ^{60}Co unit gate, Bkg is the background rate of the NaI detector when shielded from the plastic ^{60}Co unit, and

$$T = G + NG + Bkg.$$

Fig. 1 shows a simplified block diagram of the

TABLE I
Summary of results of tests with irradiated samples.

Source number	Cobalt concentration (%)	Irradiation time	Disintegration rate (s^{-1})	Relative scintillation efficiency (%)
1	0.00	unactivated	..	100
2	0.50	control samples	..	68
6	0.50		780	50
7	0.50	4 min	820	28
8	0.00		-	50
9	0.30		440	57
13	0.25		920	52
10	0.25		920	52
11	0.00	8 min	-	63
12	0.20		620	52
14	0.30		1360	44
15	0.09		800	53
16	0.09	20 min	900	48
17	0.06		400	52
21	0.20		1650	44
30	0.10	-	1000	79
31	0.10		1500	79

ORIGINAL PAGE IS
OF POOR QUALITY

D. J. FORRIST et al.

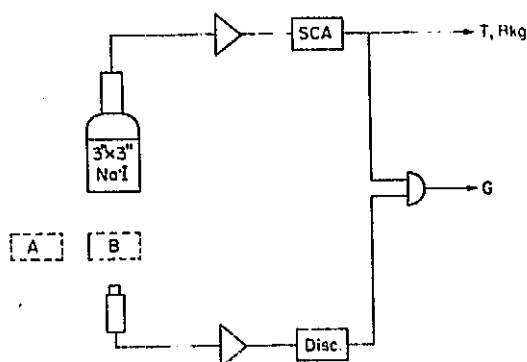


Fig. 1. Simplified diagram of method used to measure gating efficiency.

experimental setup used to measure the gating efficiency. The rates T and G were taken with the lead attenuation in position "A" while the rate Bkg was taken with the attenuator in position "B".

One of our applications, however, required that we place the calibration source on the end of a 2" long $\times \frac{1}{4}$ " diameter plastic light pipe. Because of the extra light loss the above source could only achieve a gating efficiency of $\approx 85\%$ when used with this light pipe. To regain the lost light the cobalt compound was activated before being mixed with the unpolymersed scintillator. This was accomplished by evaporating the benzene out of the same cobalt compound used before. The resulting residue was then irradiated and the benzene was added again so that pipettes could be used to transfer the activity to the scintillator. The mixture was then polymerized in the normal fashion. All cutting and polishing had to be done by hand so that our machine tools would not become contaminated. The light output from these sources was ≈ 1.5 times that from the sources made in the first way (see sources 30 and 31 in table 1). The gating efficiency of these sources when used on the light pipe was $95 \pm 1\%$.

The 98% gating efficiency we have obtained is most likely near the maximum that can be obtained with ^{60}Co and plastic scintillators. The phosphor efficiency of plastic scintillators is $\approx 5-10$ photons per keV of energy loss and the quantum efficiency of photocathodes is $\approx 10-20\%$. These numbers imply that there is less than a 50% probability of gating a 1 keV beta particle even if the threshold is set at the single photon level. Since $\approx 2\%$ of the beta particles from ^{60}Co have energies less than 1 keV, the maximum gating efficiencies we can expect are of the order of 97% to 99%. To achieve significantly higher gating efficiencies one would have to use an isotope with a

much higher beta energy and/or load the isotope into a scintillator with a much higher phosphor efficiency such as NaI.

As stated earlier ^{241}Am is an ideal source for calibration of X-ray detectors. The large alpha particle light pulses emitted in coincidence with the 26 and 54 keV gamma rays are easy to detect and result in high gating efficiencies. To date the ^{241}Am calibration sources that we have used are the ^{241}Am doped NaI "Light Pulser" crystal as commercially supplied by Harshaw Chemical Co. Although gating efficiencies are near 100%, the strong internal absorption of the low energy X-ray within the NaI crystal and its housing result in a very low X-ray flux for calibration purposes. However, there should be no difficulty doping a plastic scintillator with an organic ^{241}Am compound just as we have done with the cobalt. The internal X-ray absorption in plastic scintillators is much smaller than it is in NaI. Frost et al.⁵⁾ have recently described a satellite calibration scheme using exactly this approach.

3. Applications

We have used these calibration sources in two different ways on satellite and balloon gamma ray experiments. The development of these sources was first started to provide a gated calibration source on the UNH gamma ray experiment that is currently on board the OSO-7 (1971-083A) satellite which was launched on 29 September 1971. The gamma ray detector in this experiment is a high resolution $3" \times 3"$ NaI(Tl) scintillator which covers the energy range 0.3 to 9 MeV.

This detector is in anti-coincidence with a ≈ 5 cm thick shield of CsI(Na) which surrounds the central detector as shown in fig. 2. The ^{60}Co plastic scintillator is placed next to the central NaI detector and is viewed by its own photomultiplier through a 2" long light pipe. During normal operation the central detector is in anti-coincidence with the signals from both the ^{60}Co calibration source and CsI shield. Hence only gamma rays not interacting in any part of the shield are analyzed. During calibration, however, the central detector is still in anti-coincidence with the shield, but a coincidence with the ^{60}Co unit is required for analysis.

The calibration sequence is initiated twice each orbit as the satellite makes a day/night transition and it can be initiated at any other time by ground command. The information in the calibration spectrum is immediately inspected by means of a "Quick Look" telemetry link and several instrument parameters are checked. First the central detector's gain and linearity

ELECTRONICALLY GATED GAMMA AND X-RAY CALIBRATION SCHEME

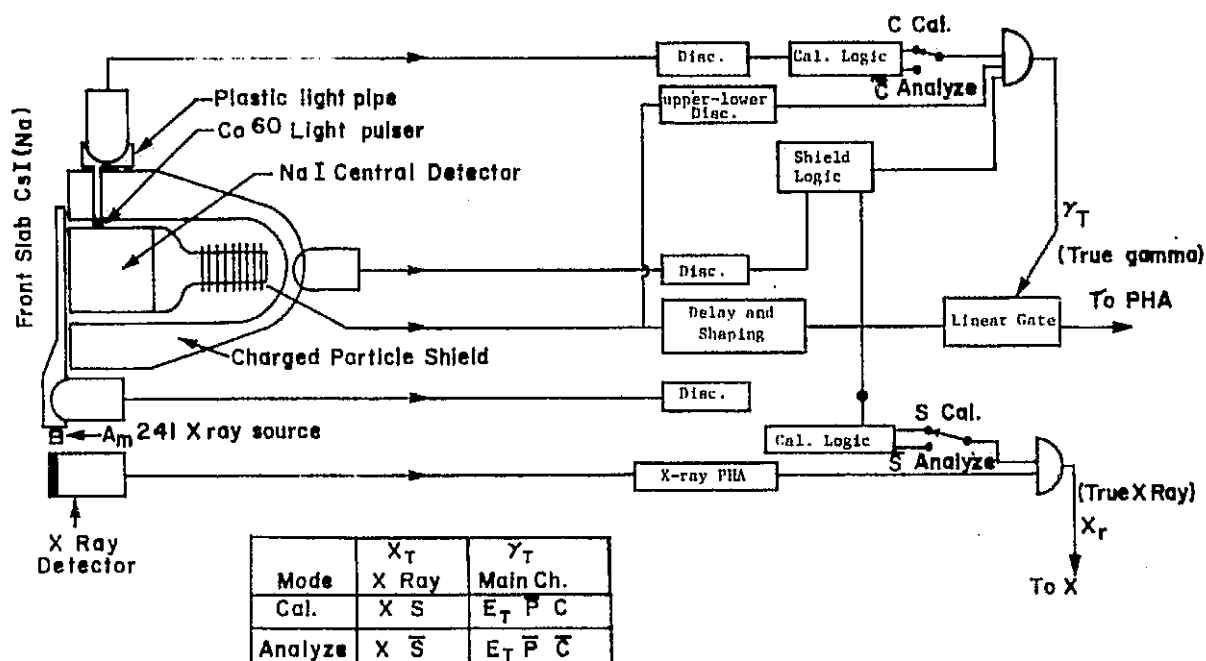
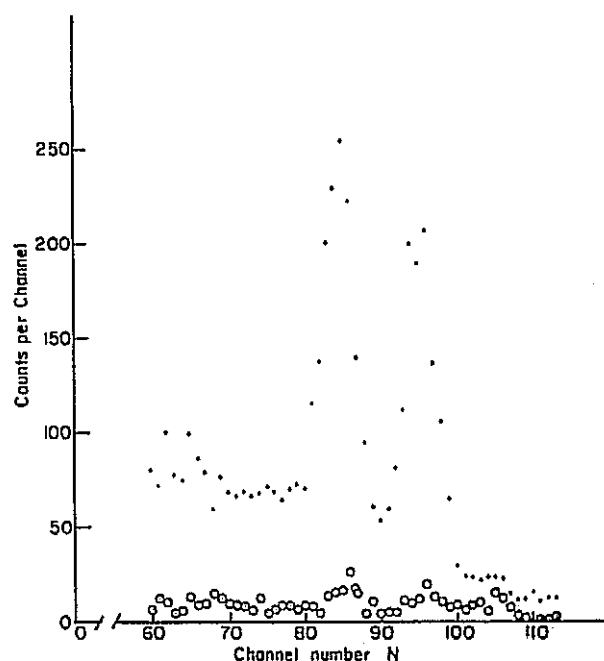


Fig. 2. Simplified block diagram of the UNH OSO-7 gamma ray experiment.

can be checked by noting the location of the two main peaks at 1.17 and 1.33 MeV and the sum peak at 2.50 MeV. If a gain change is noted it can be corrected by sending the appropriate commands to the central detector's programmable high voltage power supply. Second, because the CsI shield acts as an anti-Compton suppressor, the intensity of the ^{60}Co calibration spectrum also acts as a monitor of the shield threshold. Fig. 2 shows in a partial block diagram how the ^{60}Co calibration source and the central detector-CsI shield interact in the normal and in the calibration mode. Fig. 3 shows two pulse height spectrums, one with the ^{60}Co unit connected in the calibration mode and one with it disconnected.

The second application of the ^{60}Co calibration source involves its use in a digital stabilizer loop. The central detector in this experiment was an $11'' \times 5''$ NaI(Tl) crystal covering the energy range 0.3 to 7 MeV, and it was surrounded by a 1 cm thick plastic scintillator charged particle shield. The main purpose of the experiment was to search for gamma rays from the Sun and other extraterrestrial objects. It was carried to the top of the atmosphere by a large balloon. Fig. 4 shows a simplified block diagram for this experiment. Normally an event in the central detector, if not accompanied by an event in the charged particle shield, goes through a preamplifier, a shaping amplifier, a gain-controlled

amplifier and the linear gate to the pulse height analyzer (PHA). The digital output of the PHA is then telemetered to the ground station for storage.

Fig. 3. ^{60}Co pulse height spectrums; top - ^{60}Co calibration on; bottom - ^{60}Co calibration off.

D. J. FORREST et al.

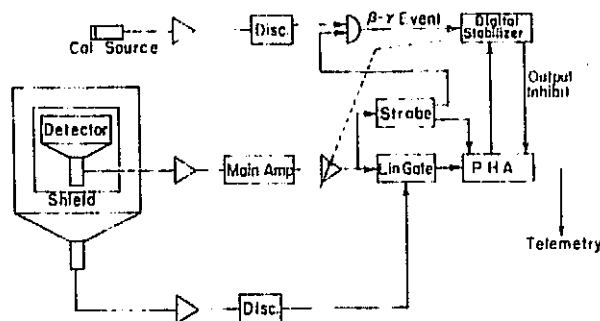


Fig. 4. Simplified block diagram of UNH's large NaI detector showing digital stabilizer loop.

However, when an event in the central detector is accompanied by an event in the ^{60}Co calibration unit, the digital stabilizer circuit is automatically commanded to inspect the output of the PHA, for a count in either of the two preset windows centered around one of the ^{60}Co peaks. If a count in one of the windows is found, then the stabilizer sends the appropriate command to the gain-controlled amplifier. For a calibration event the output of the PHA is inhibited so that the ^{60}Co spectrum is not accumulated.

The use of the gated ^{60}Co calibration unit in this

application allows for a high rate of calibration events necessary for good stabilizer control without accumulating a large number of calibration events in the unknown spectrum. Also, the calibration events are not affected by any change in the background counting rate of the central detector.

We gratefully acknowledge the gift of the organic cobalt compound from Dr. J. Webber, Mr. R. Kwor for assistance in preparation of the cobalt sources and Mr. I. Gleske for assistance in the calibration of the sources. Time-zero Corporation, Torrance, California designed and calibrated the electronics for the OSO-7.

References

- 1) A. Liuzzi and B. S. Pasternack, Nucl. Instr. and Meth. **57** (1967) 229.
- 2) J. M. Ferguson, Nucl. Instr. and Meth. **58** (1968) 318.
- 3) E. L. Chupp, P. J. Lavakare and A. A. Sarkady, IEEE Trans. Nucl. Sci. NS-16, no. 1 (1969) 309.
- 4) J. B. Birks, *The theory and practice of scintillation counting* (The MacMillan Co., New York, 1964).
- 5) K. J. Frost, B. R. Dennis and R. J. Lencho, Experiment to measure hard solar and celestial X-rays from the fifth orbiting solar observatory, GSFC Report X-680-70-440 (1970).

ORIGINAL PAGE IS
OF POOR QUALITY

A GAMMA RAY MONITOR FOR THE OSO-7 SPACECRAFT*

P. R. Higbie, E. L. Chupp, D. J. Forrest, I. U. Gleske

Department of Physics
University of New Hampshire
Durham, New Hampshire 03824

Summary

A 3" x 3" NaI(Tl) gamma ray (0.3 to 10 MeV) spectrometer with a CsI(Na) charged particle and anti-Compton shield has been developed for the ORBITING SOLAR OBSERVATORY (OSO-7) which was launched September 30, 1971. The instrument, designed for a rotating wheel compartment, utilizes a 377 channel quadratic PHA with accumulation times of 3, 1, or 0.5 minutes. Quick look and calibration data obtained via a direct data link to a minicomputer at the UNH campus allows near real time monitoring and control of the experiment. Various commands changing the operating mode can be executed. The functions which can be commanded include: rotation of the quadrants in which data is collected by 90°; gain adjustment of the central detector over a 6:1 range; manual or automatic sequencing of calibrations; variation of accumulation times by telemetering selected channels; and selection of reference directions. A small X-ray detector covering the range 7.5 to 120 keV is also included.

Introduction

The primary objective for the University of New Hampshire instrument is monitoring the Sun for emission of solar gamma rays. Possible gamma ray line emission from nuclear processes as well as the continuous gamma spectrum are to be investigated. The data can be correlated with sporadic solar events and can provide limits on steady or slowly varying gamma ray emissions. In addition, direct correlations can be made with data from the X-ray detector. These considerations led to an instrument which has high energy resolution, good time resolution, and crude angular resolution. The instrument will also study the Earth's albedo gamma rays and such celestial sources as supernovae, their remnants, and the galactic disk.

Gamma ray lines will be emphasized in the spectrum because of the high resolution (7.5-8.0% at 0.662 MeV). As an example, gamma rays at 0.51, 2.22, 4.43, and 6.15 MeV would indicate production of

positrons, neutrons, and excited nuclei from various nuclear processes. The energy dependent angular resolution of the instrument will help in determining the contribution from the solar, albedo, and celestial sources.

A data link has been set up to provide near real time control for the instrument. The data can be scanned for calibrations and can be examined for evidence of solar activity. Indications of solar activity or predictions of high flare probabilities might prompt the use of the faster time resolution modes.

Instrument Description

The instrument is shown schematically in Figure 1. The basic sensor is a 3" x 3" NaI(Tl) crystal mounted on a RCA C31012 stacked ceramic ruggedized photomultiplier. This assembly is mounted inside a CsI(Na) anticoincidence shield viewed by RCA C70132B phototubes. An ancillary X-ray detector and calibration sources complete the instrument. Figure 2 shows a photograph of the assembled flight instrument.

The NaI crystal was mounted by Harshaw Chemical Company directly on the sapphire face plate of the photomultiplier and hermetically sealed in a thin-walled stainless steel housing (low radioactivity 304ss). The crystal was restrained within the housing by a spring delivering a force of 60±5 lbs. Bleeder resistors were attached to the dynodes and coated with RTV 11. A rear housing was placed over the bleeder network and voids were foamed with Uralane 1723. The CsI(Na) cup was rigidly held against the outer aluminum housing by a pressure plate. A wave spring between the pressure plate and central detector restrained the latter from moving with respect to the cup.

The central detector is shielded by a thick CsI(Na) cup and a thin front slab of the same material. Charged particle interactions in either of these shields initiate anticoincidence logic signals. Gamma rays have a high probability of passing through the thin front shield without interaction; however, the cup, being 1.5 inches thick nearest the central detector, attenuates 1 MeV gamma rays by at least 60%. Gamma rays which pass

* This work was supported by NASA under Contract Nas 5-11054.

through the front slab and undergo Compton scattering in the central detector have a high probability of interacting in the cup. A 0.511 MeV escape gamma ray from an incident primary gamma ray producing a pair in the central detector may also interact in the cup. In either case an anticoincidence pulse is produced which improves the energy response function of the system by accentuating the photopeak. Figure 3 shows this effect for an external Co^{60} source.

The $\text{CsI}(\text{Na})$ cup is viewed by four hemispherical RCA C70132B photomultipliers. Three tubes are arranged at approximately 120° around the axis of symmetry, with the fourth tube at the apex of the cup. The cup is made from two cylindrically symmetric pieces with the parting plane near the fourth tube. The photomultipliers are coupled with RTV 165 to the shield crystals which are covered by household aluminum foil for enhancing light collection.

The front slab is viewed by a single RCA C70132B photomultiplier. One end of the slab is thickened and the hemispherical photocathode is recessed to be at the same level as the slab to take advantage of light piping effects. The Am^{241} doped $\text{NaI}(\text{Tl})$ crystal which forms part of the X-ray calibration system is also viewed by this tube through the CsI , an air interface, and the glass hermetic seal of the $\text{NaI}(\text{Tl}, \text{Am})$ can.

The small X-ray monitor is an uncollimated $\text{NaI}(\text{Tl})$ crystal, $1/4"$ thick x $1\ 1/4"$ diameter, with a 10 mil Be window. This is viewed by an RCA 4461 flat faced $1\ 1/2"$ diameter phototube. The output is divided into four energy channels: 7.5-15, 15-30, 30-60, 60-120 keV.

Calibration of the gamma ray spectrometer is accomplished by use of a Co^{60} source giving lines at 1.17 and 1.33 MeV. The source is dispersed (as cobalt octo-late) in a plastic scintillator (Pilot M Partially Polymerized Plastic Scintillator) as described elsewhere¹. A 0.02 μCi source in the shape of a small disk was bonded to the end of a light pipe which passed through a hole in the CsI cup so that the source was positioned adjacent to the central detector. Light from the plastic scintillator is collected by an auxiliary C70132B phototube. When Co^{60} decays to Ni^{60} , the beta particle is always accompanied by prompt gamma rays, more than 99% of which are the two cascade lines at 1.17 and 1.33 MeV. The gamma rays can pass unhindered into the central detector, but the beta particle deposits its energy in the plastic scintillator thus giving a logic signal from the auxiliary phototube

which is used to gate the signal from the central detector. This system has achieved a beta ray tagging efficiency of better than 95%. In normal operation the system is run in anticoincidence and the cobalt gamma rays are rejected, but in the calibration mode the system is run in coincidence and two prominent lines appear in the recorded spectrum with only accidental background contamination. A similar system to calibrate the X-ray detector uses Am^{241} which emits an alpha particle in coincidence with a gamma ray line at 60 keV.

The instrument is located in compartment 9 of the rotating wheel section of the OSO-7 spacecraft with the crystal and cup axes colinear with a wheel radius. Data is accumulated when the instrument axis lies within 45° of either the solar or antisolar direction.

Instrument Data Formating

A block diagram of our instrument is shown in Figure 4. The spacecraft telemetry system employs a 800 Hz clock and reads data out on a basic 32-word (byte) Main Frame cycle. The data from the instrument falls under three broad categories:

Spectral data from the central detector which is read out in two words which appear in every Main Frame cycle. Flag, status, clock, and dead time words also accompany every spectrum transmitted.

X-ray data is submultiplexed onto the Digital Subframe (DSF) which is a 48-word cycle on one word of the Main Frame. The instrument is assigned seven words which are spread though the cycle with two DSF cycles required to read out all X-ray channels and associated flags and times. Every 7.7 seconds a half second "snapshot" of the Sun is taken in successive energy ranges. The comparison quadrant is treated similarly.

Housekeeping and rate data are telemetered in 10 consecutive words of the 48-word Analog Subcommutator Cycle (ASC).

Gamma Spectral Data

The gamma ray pulses from the anode of the central detector flow through the front end electronics, where they are amplified by a charge sensitive pre-amplifier. The output is double differentiated and passes through a linear gate controlled by a variety of logic pulses. The gate is strobed to pass the flat portion of the signal and a peak detector is used to charge a capacitor used by a

Quadratic Analog to Digital Converter (QADC). The channel number, n , which is the digitized output of this device is related to the energy loss, E , in the central detector by

$$E = k(n + n_0)^2.$$

Over the nominal energy range covered by the instrument the half width in energy of a crystal photomultiplier combination for a given gamma ray line is approximately proportional to \sqrt{E} . In terms of channel numbers, however

$$\Delta E = 2k(n + n_0)\Delta n$$

to first order in Δn . Consequently, if we choose ΔE to be the half width, the corresponding Δn is approximately constant. Our system parameters were chosen such that we have approximately five channels under a gamma peak independent of energy. The QADC optimizes our telemetry usage by keeping the ratio of the detector to electronic resolution constant over the desired energy range (0.3-9.1 MeV) which then requires 377 channels. The QADC and memory is described in a companion paper in this volume².

For a given pulse height, E , a corresponding 12-bit word is fetched from core storage, incremented and replaced. This memory is operated according to an exchange buffer technique. While one half is being updated by the random gamma input, the second half is sequentially read out into the spacecraft telemetry system. These halves are again divided into sections for the solar and antisolar directions.

Gamma Logic. The admission of the desired gamma ray into the data stream is controlled by a linear gate in the following manner: First, a window discriminator, set to match the lowest and highest channels of the following QADC, provides a strobing input to the gate. For the nominal gain setting of the central detector this provides thresholds of 0.3 and 9.1 MeV. Other logic signals include PHA busy, anticoincidence pulses from the cup, slab and the Co^{60} source. The Co^{60} pulse as noted above, can be placed in coincidence for calibration operation. The anticoincidence pulse from the CsI cup has a variable width to cover the slow decay component of CsI(Na) after giant pulses. An analog dead time circuit sums all contributions to the dead time and increments its corresponding memory word after every 1.515 millisecond dead time accumulation. The dead time circuit also returns a pulse to cover its own operation. A final control pulse is provided by the

quadrant generator. This is an electronic subsystem which provides control pulses to the linear gate, the memory, the X-ray logic and the rate meters whenever the detector axis lies within the 90° sectors centered on either the solar or background directions. Data is accumulated for complete quadrants only and the total clock time for which accumulation was permitted is also sorted in core memory.

Fast Time Resolution and Other Modes.

Three formats for channel readouts are available: a full scan mode; a short scan mode covering channels selected for possible lines at 0.511, 2.2 MeV and calibration lines; and an intermediate scan covering these lines and the 4.43 and 6.13 MeV lines. The motive is to provide faster time resolutions of 30 and 61 seconds compared with the three minutes required for the full scan.

The instrument can be commanded to operate under several conditions besides the time read out and calibration modes described above. The night reference direction which is normally given by a Sun-pointing gyro can be switched to the magnetometer signal provided by the spacecraft. The quadrant normally aligned along a reference direction may be rotated by 90°. The central detector's gain can be controlled by adjusting its high voltage. Adjustments can be made in two ranges of approximately 150 volts which slightly overlap. Each range is divided into 64 steps. This supply and the high voltage supply for the shields, Co^{60} calibration, and X-ray tubes may be turned on and off independently. Calibration is automatically sequenced (but may be inhibited by command) at satellite dawn and dusk crossings and may also be initiated by a manual calibrate command. In the manual calibrate case, electronic pulses are also sequenced to calibrate the system amplifiers and thresholds.

These various modes are summarized in Table I.

X-ray Spectral Data

The pulses from the X-ray tube are amplified by a charge sensitive pre-amplifier and placed either in coincidence or anticoincidence with the front slab, depending on whether the instrument is in the calibrate mode or not. The X-ray data is also gated by the quadrant generator to accumulate only the latest complete quadrant. The analog pulses are attenuated by successive factors of two depending on which of the four energy intervals is being sampled and presented to a window discriminator. The number of counts is

accumulated by an adaptive scalar which can handle a maximum of 18,688 pulses.

Rates and Housekeeping

Various rates and housekeeping data are handled via the analog subcommutator channel. These include log rate meter outputs for the shield, cup and central detector, each of which is sampled synchronously with the spacecraft rotation and read out every 15.36 seconds. Temperatures, voltages, and status of the operating modes are also monitored and read out every 184 seconds. A typical calibration curve for the rate meters is shown in Figure 5.

Detector Properties

The system was calibrated using Na^{22} , Cs^{137} , Co^{60} , Th^{228} sources and a special Cm^{244} - C^{13} source. The last source gives a monoenergetic line at 6.130 MeV through the $\text{C}^{13}(\alpha, n)\text{O}^{16*}$ reaction. The peak channel for the gamma ray lines from these sources is shown as \sqrt{E} vs. n in Figure 6 for a typical gain setting.

The crystal and photomultiplier combination were carefully chosen to give a nominal energy resolution of 7.5% at 0.662 MeV. Because of the saturation effects in the central photomultiplier, the flight unit was provided with a nonlinear voltage divider network to assure signal linearity over our range of interest.

The number of channels corresponding to the half widths for the sources listed above is also shown in Figure 6. The salient characteristics of the instrument are summarized in Table II.

Acknowledgements

Antal A. Sarkady of the UNH Electrical Engineering Department contributed significantly to the design and testing during the breadboard and prototype development. The instrument was designed, fabricated, and tested in collaboration with Time-Zero Corporation under the successive supervision of the Project Managers, Robert Kobayashi and Donald Rose and the design team of J. Chapsky, R. Evelyn-Veere, and D. Aalami. Considerable support and assistance was given by the OSO Project Office under the Project Director, John Thole and the Experiment Manager, John Donley.

References

- 1 Forrest, D. J., P. R. Higbie, L. E. Orwig, and E. L. Chupp, "An Electronically Gated Gamma and X-ray Calibration Scheme," to be published.
- 2 Burtis, D. W., D. Aalami, R. H. Evelyn-Veere, and A. A. Sarkady, "A Quadratic Pulse Height Analyzer for Space Applications," IEEE Transactions on Nuclear Science, this volume.

Table I - Summary of Modes

<u>Mode</u>	<u>Function</u>
Quadrant	normal or rotated 90°.
Scan	selection of channels read out (full, intermediate, or short).
Manual Calibrate	electronic and radioactive calibrations.
Autocalibrate	radioactive calibration at dawn or dusk.
Shield High Voltages	(on/off).
Central High Voltage	(on/off).
Gain Change	(upper/lower Central Detector High Voltage Range).
Gain Step	(0 thru 63 steps on either Central Detector HV Range).
Aspect Reference	Magnetometer or Gyroscope.

Table II

Spectral Range	0.3-9.1 MeV (nominal).
Spectral Resolution	<8% @ 0.662 keV; 377 channel quadratic pulse height analyzer.
Angular Resolution	120° x 70° FWHM at 1 MeV in solar and antisolar directions.
Time Resolution	3 minutes, 61 or 30 seconds.
Effective Area	45 cm ² (point source on axis).
Bits per Second	50.
Power (nominal)	3.5 watts.
Weight	74 lbs.
Detector Type	3" x 3" NaI(Tl) crystal in CsI(Na) shield.

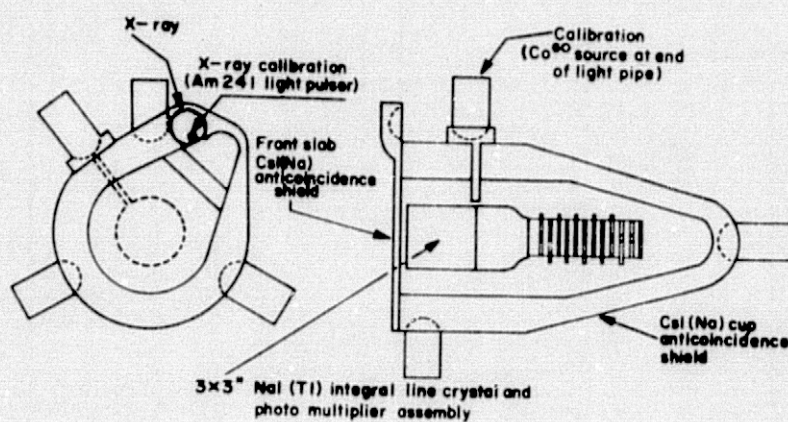


Figure 1. Instrument Schematic.

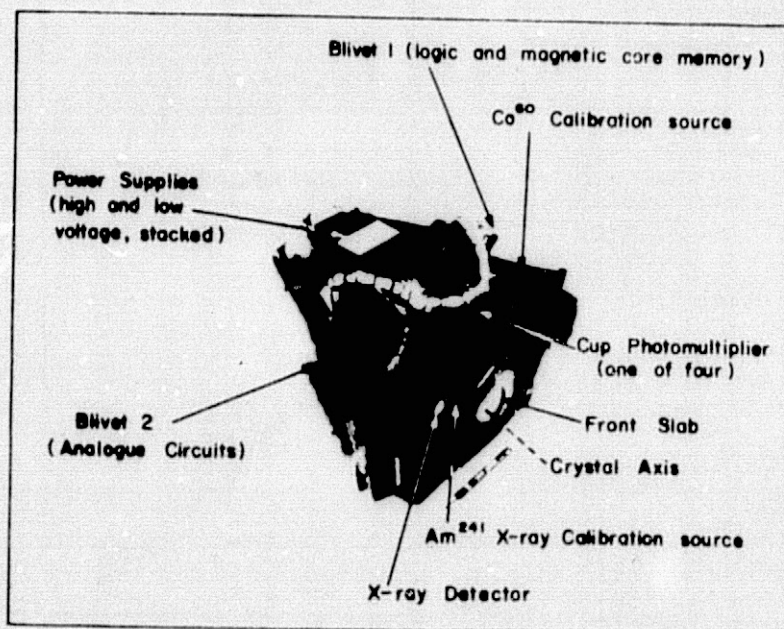


Figure 2. Photograph of the Solar Gamma Ray Monitor.

ORIGINAL PAGE IS
OF POOR QUALITY

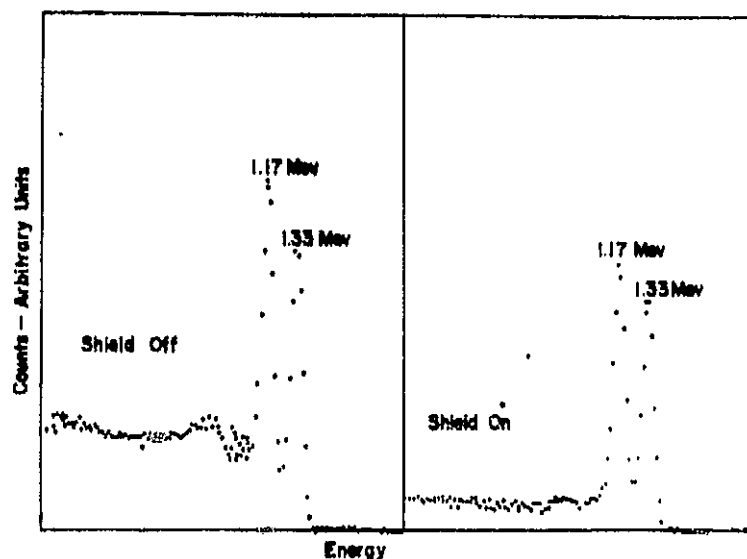


Figure 3. Compton suppression due to cup. The relative decrease of the line intensities with the cup on and off is real and is due to one of the cascade gamma pair interacting in the cup.

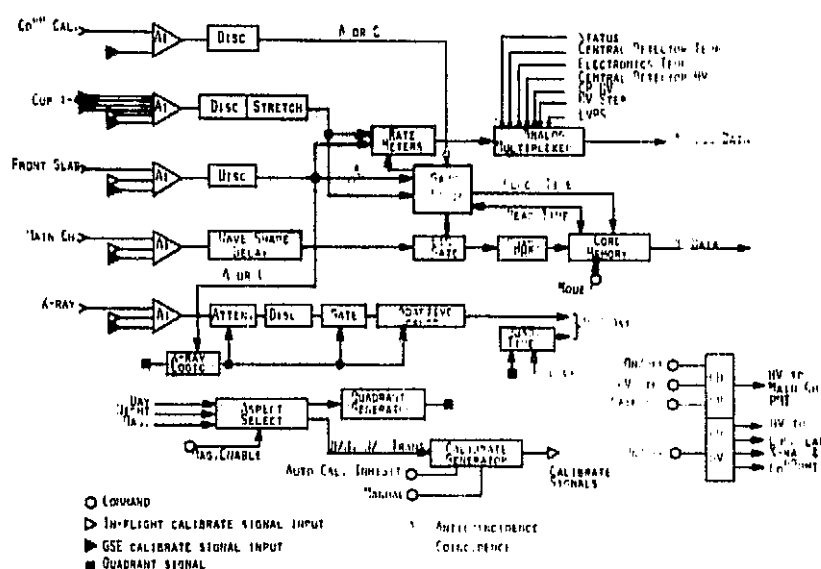


Figure 4. Simplified System Block Diagram.

ORIGINAL PAGE IS
OF POOR QUALITY

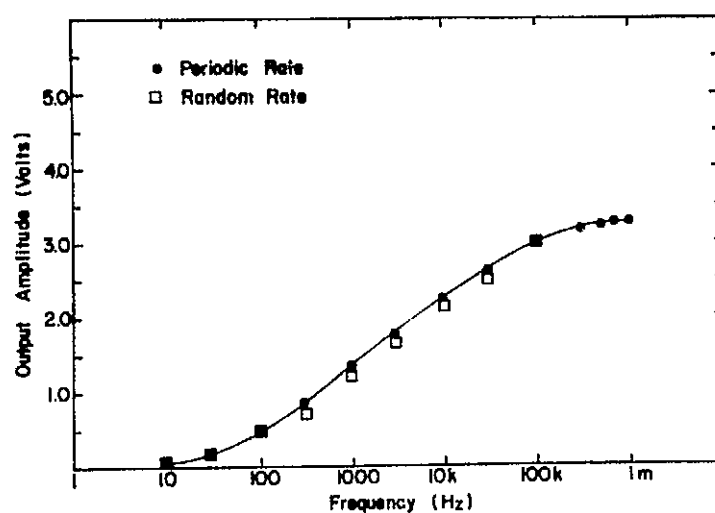


Figure 5. Typical calibration curve for the analog rate meters.

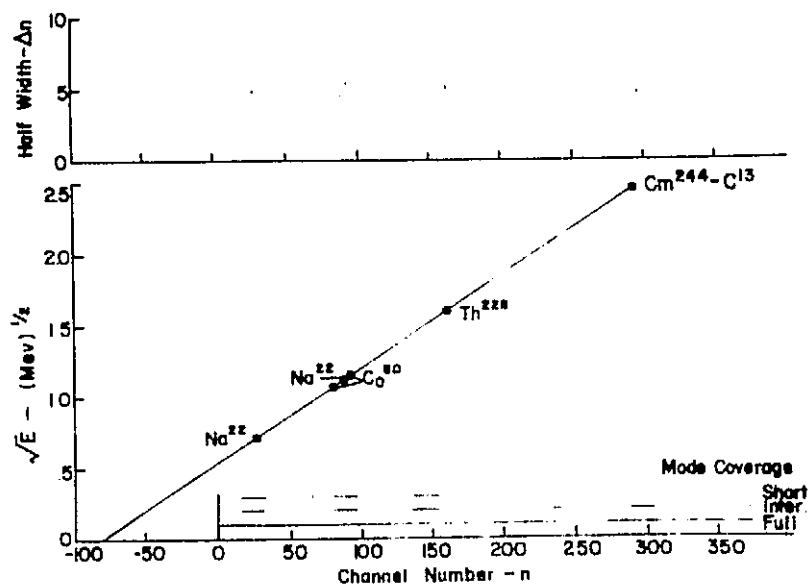


Figure 6. Calibration curve for the Quadratic Analog to Digital Converter. The constancy of line half widths is shown in the upper graph. Channels read out in the fast time resolution modes are illustrated below.

ORIGINAL PAGE IS
OF POOR QUALITY